Bio-Electromagnetic Model of Deep Brain Stimulation

THÈSE N^{O} 4369 (2009)

PRÉSENTÉE LE 2 AVRIL 2009

À LA FACULTÉ SCIENCES ET TECHNIQUES DE L'INGÉNIEUR

Laboratoire d'électromagnétisme et acoustique

SECTION DE GÉNIE ÉLECTRIQUE ET ÉLECTRONIQUE

ÉCOLE POLYTECHNIQUE FÉDÉRALE DE LAUSANNE

POUR L'OBTENTION DU GRADE DE DOCTEUR ÈS SCIENCES

PAR

Grégoire WALCKIERS

acceptée sur proposition du jury:

Prof. A. Ionescu, président du jury
Prof. J. R. Mosig, Dr J.-M. Vesin, directeurs de thèse
Prof. K. Aminian, rapporteur
Dr C. Pollo, rapporteur
Dr N. Yousif, rapporteur

ÉCOLE POLYTECHNIQUE
FÉDÉRALE DE LAUSANNE

Lausanne, EPFL
2009

À Barbara

Électricité (*n.f.*): Propriété qu'ont tous les corps d'attirer, dans certaines circonstances, les corps légers environnants, d'émettre des étincelles, de causer des commotions nerveuses chez les animaux.

(dictionnaire Larousse classique illustré - 1913)

Abstract

Functional stimulation is one of the most fascinating applications of bioelectromagnetism. It deals with the stimulation of excitable biological tissues by electromagnetic fields. One of its most impressive medical applications is the subthalamic nucleus deep brain stimulation (DBS). It consists in the insertion of an electrode into the deep brain, delivering electric pulses to treat Parkinson's disease and other movement disorders. But despite its wide use throughout the world for almost twenty years, the understanding of the mechanisms of action remains unclear.

To help clinicians to better understand the mechanisms of DBS, its limitations and implications from an electrical point of view, electrical models of the head can be used to predict the electric potential distribution generated by the electric pulse. With the development of medical imaging techniques, the information on biological tissues that can be used to build these electrical models has never been so detailed. The diffusion tensor magnetic imaging (DT-MRI) is able to provide the orientation of the fibers within the cerebral tissues. Thus, the high inhomogeneity and anisotropy of the head can be modeled through anisotropic electrical conductivity tensors to set up realistic models of the patient's head.

This thesis aims to provide to clinicians an accurate prediction of the potential distribution generated by the electric pulse. With this purpose, a finite element (FE) model is set up using electric conductivity values based on DT-MRI data. Special care has been taken to model more realistic boundary conditions than the ones commonly encountered in literature. A great effort has also been put to model the tissues surrounding the stimulation. The results show that these two aspects are impacting significantly the potential distribution.

To predict the neural extent of the stimulation, electrical equivalent models of axons are combined with the obtained potentials. Volume of tissues activated (VTA) are thus obtained. Results show that the VTA are also impacted by the decision on how to model the boundary conditions. They show that the usual choice assumed in literature up to now leads to an overestimation of 30% of the VTA.

Keywords

Bioelectromagnetism, deep brain stimulation, finite element method, diffusion tensor imaging, human head model

Résumé

La stimulation fonctionnelle est l'une des applications les plus fascinantes du bioélectromagnétisme. Elle consiste en la stimulation des tissus biologique excitables par un champ électromagnétique. L'une des applications médicales les plus impressionantes est la stimulation cérébrale profonde (DBS) du noyau sous-thalamique. Celle-ci consiste à introduire une électrode dans les profondeurs du cerveau et d'y appliquer des impulsions électriques afin de traiter la maladie de Parkinson ou d'autres troubles moteurs. Mais malgré son usage largement répandu à travers le monde depuis près de vingt ans, la compréhension de ses mécanismes d'actions demeure incomplète.

Afin d'aider les practiciens à une meilleur compréhension des mécanismes de la DBS, ses limitations et ses implications d'un point de vue électrique, des modèles numériques de la tête humaine peuvent être utilisés afin de prédire la distribution des potentiels générés. Grâce au développement des techniques d'imagerie médicale, les informations disponibles sur les tissus biologiques utilisables pour établir ces modèles n'ont jamais été aussi détaillées. L'imagerie par résonnance magnétique du tenseur de diffusion (DT-MRI) est capable de fournir l'orientation des fibres composant les tissus cérébraux. Dès lors, la forte inhomogénéité et l'anisotropie de la tête peuvent être modélisées au travers de conductivités électriques anisotropiques, afin de mettre au point un modèle réaliste du patient.

Cette thèse a pour but de fournir aux practiciens une prédiction détaillée de la distribution des potentiels générés par l'impulsion électrique. Dans cette optique, un modèle d'éléments finis (FE) est mis au point, utilisant des valeurs de conductivités électriques basées sur les données du DT-MRI. Un soin particulier a été pris afin de modéliser des conditions aux limites plus réalistes que celles fréquemment rencontrées dans la littérature. Un important effort a aussi été porté sur la modélisation des tissus entourant l'électrode de stimulation. Les résultats montrent que ces deux aspects ont un impact significatif sur la distribution des potentiels.

Afin de prédire l'étendue de la stimulation au niveau neural, des modèles équivalents électriques d'axones sont combinés avec les potentiels obtenus. Le volume de tissus activés (VTA) est alors obtenu. Les résultats montrent que les VTA sont aussi influencés par les choix de modèlisation des conditions aux limites. Ils montrent que le choix généralement assumé dans la littérature jusqu'à présent conduit à une surestimation du VTA de l'orde de 30 %.

Mots-clés

Bioélectromagnétisme, stimulation cérébrale profonde, méthode des éléments finis, imagerie par résonnance magnétique du tenseur de diffusion, modèle de tête humaine

Remerciements

La réalisation d'un travail de thèse est un long chemin. Sans le soutien de nombreuses personnes, la fin du chemin serait tout bonnement inaccessible. Je tiens ici à remercier toutes ces personnes qui m'ont guidé, accompagné ou encouragé le long de celui-ci.

Je tiens à adresser mes remerciements en tout premier lieu à mes deux directeurs de thèse. D'abord au Professeur Juan R. Mosig qui m'a proposé cette thèse, accueilli au sein de son laboratoire et soutenu lors des moments importants, malgré le décalage entre mon sujet et la thématique habituelle du laboratoire. Si l'ambiance dans ce laboratoire est si agréable, c'est en grande partie grce à lui. Ensuite à Jean-Marc Vesin qui a continué à jouer le jeu jusqu'au bout malgré l'orientation prise par ce travail.

Ce travail n'aurait jamais pu tre réalisé sans le soutien inconditionnel du Docteur Claudio Pollo, grce à qui le projet a vu le jour. Il faut savoir qu'il est un vrai docteur, un docteur qui sauve des vies. Et il a pris de son (précieux) temps pour me suivre tout au long du travail. Je dois avouer que ce fut un privilège de pouvoir travailler avec lui. Je le remercie pour toutes nos discussions et pour l'intért qu'il a eu pour mes recherches. Ce fut pour moi une véritable source de motivation.

Je remercie aussi les autres membres du jury, le Professeur K. Aminian et le Docteur N. Youssif, qui ont pris le temps de lire et d'améliorer mon travail grce à leurs remarques. Merci aussi au président du jury le Professeur A. Ionescu.

Je tiens également à remercier les permanents du laboratoire, à savoir Anja, Jean-Francois, Michael et Hervé, avec qui j'ai toujours eu plaisir à discuter, que ce soit autour d'un café ou au détour d'un couloir. Un merci particulier à Eulalia, la fée du labo, qui non seulement règle tous les problèmes d'organisation que l'on peut rencontrer, mais le fait en plus avec un sourire et une bonne humeur inébranlable.

Merci à tous les doctorants que j'ai eu le privilège de croiser durant ces cinq années et particulièrement ceux avec qui j'ai partagé mon bureau. Julien et Sergio d'abord, je suis sr que les murs de la diagonale résonnent encore de nos chants. Puis Pedro, avec qui j'ai partagé de nombreux bons moments et d'enrichissantes discussions sur le quai de la gare. Enfin merci à Benjamin, qui m'a motivé, supporté, encouragé, relu et coaché pendant le money-time . Ses précieux conseils ont vraiment été salutaires pour l'élaboration de ce travail.

Je remercie aussi les personnes qui ont relu les chapitres de ma thèse: Michael, Ivica, Pedro et Laurent. Merci d'avoir répondu présent et d'avoir consacré une partie de vos nuits, dans l'urgence, à relire et corriger ces pages. Un merci particulier à Ivica qui avait déjà commencé à travailler sur le projet avant moi et à qui je dois une section complète de ce manuscrit.

Je tiens à remercier tous mes camarades d'études avec qui j'ai partagé les repas et autres moments de détente, à savoir Yvan, Gilles, Thomas, Grégoire, Claude, Frédéric et Fabien. Le soutien mutuel que l'on s'est apporté lors des moments plus difficiles restera inoubliable.

Un merci particulier à mes parents, qui ont fait de moi ce que je suis. Merci pour votre

soutien inconditionnel tout au long de mes études. Merci à mes soeurs, beaux-frères et neveux. Merci aussi à ma belle famille et à mes amis.

Enfin merci à ma femme, je te serai à jamais reconnaissant pour tout l'amour et le soutien que tu m'as apporté et pour la patience dont tu as fait preuve. Tu as joué tous les rles nécessaires pour me maintenir et me faire avancer sur ce chemin qu'est la thèse, et sans toi je crois que je n'en aurais jamais vu la fin.

Table of Contents

Acronyms used in this thesis

BC	Boundary condition
BEM	Boundary element method
CSF	Cerebrospinal fluid
CT	Computed tomography
DBS	Deep brain stimulation
DT-MRI	Diffusion tensor magnetic resonance imaging
EEG	Electroencephalogram
FDM	Finite difference method
FE	Finite element
FH	Frankenhaeuser-Huxley
HPAV	Half pulse amplitude volume
MEG	Magnetoencephalogram
NEMS	Neuromuscular electrical stimulation
RCE	Return current electrode
STN	Subthalamic nucleus
VTA	Volume of tissue activated

1 Introduction

The actual trend of combining medical science and engineering has given birth to numerous applications for the improvement of the patients' life. While the application of edge techniques and the requirements of high reliability have been a source of motivation for the engineers, the new paradigms offered by the application of cutting edge technologies to their problems have always attracted the medical world. As Lausanne is the home of two major actors of these two worlds, namely the university hospital (Centre Hospitalier Universitaire Vaudois, CHUV) and the Swiss Federal Institute of Technology (Ecole Polytechnique Fédérale de Lausanne, EPFL), many diverse collaborations are blooming between these two entities, thus giving birth to a full panoply of innovative and advanced applications in domains as varied as

- specialized sensors – Laboratory of Movement Analysis and Measurement (LMAM)
- medical imaging techniques – Signal Processing Lab 5 (LTS5) and Biomedical Imaging Group (LIB)
- orthopedic prosthesis – Laboratory of Biomechanical Orthopedics (LBO)
- computer guided surgery – Laboratoire de Systèmes Robotiques (LSRO)

and many others.
Deep brain stimulation is one of these areas for which the collaboration between engineers and medical doctors can provide rich and invaluable improvements.

The deep brain stimulation (DBS) of subthalamic nucleus (STN) is a medical technique used since the early 1990's to treat Parkinson's Disease and other movement disorders. It is now used worldwide and, in particular, it has become a standard at Lausanne's CHUV. Indeed, more than 150 patient have been treated since 1996 in the CHUV and the results have been considered as excellent for the vast majority of these persons. Nevertheless, the understanding of the mechanisms of action underlying DBS remains unclear, despite the perspective offerred now by almost 20 years of experience.
STN-DBS relies on generating electric impulses inside the brain thanks to a deeply implanted electrode. Since the effects of the STN DBS are almost instantaneous on the patient, the procedure to implant the electrode is based on a trial and error procedure. This empirical procedure aims to obtain both an exact anatomical location of the stimulation and to select its electric parameters (frequency, amplitudes, pulse shape...). Recently, long term sides effects have been observed, which could lead to the use of this therapy as treatment for other symptoms and diseases, such as chronical depressions or obsessive-compulsive troubles.
This thesis aims to provide the clinicians with a tool having the ability to predict which neural pathways are activated or inhibited by the stimulation. Such a tool can be useful for

two reasons. First, from a preoperative point of view, to improve the localization of the best stimulation target and to help in the choice of the stimulation parameters. And secondly, as a post operative tool to correlate the neural structures stimulated with the long term effects observed.

1.1 Objectives

The research presented in this thesis has been done in the frame of the Swiss National Science Foundation (SNSF) project number 31523A-108318 : "Exploration of the mechanisms underlying subthalamic deep brain stimulation for Parkinson's disease by a computer model and an analysis of the electrophysiological response of the brain to stimulation". This research project has involved the neurosurgery department on the Centre Hospitalier Universitaire Vaudois (CHUV) and two laboratories of the Ecole Polytechnique Fédérale de Lausanne (EPFL), namely the Laboratory of Signal Processing 5 (LTS5) and the Laboratory of Electromagnetics and Acoustics (LEMA).
The main objective of the project was to provide to the clinicians the best prediction possible of the tissues activated by the DBS. In this frame, an electrical conductive model of the involved body regions has been built. The so-called bioelectric problem is well-known and numerous electrical head models have been developed in the frame of electroencephalograms (EEG) prediction and analysis. These models are based on the latest high definition medical imaging techniques, to increase the realism of the modelled tissues.
The model developed in this thesis is based on diffusion tensor imaging. This allows to assign to the modelled tissues an anisotropic conductivity. Also, opposite to the previous DBS electrical models which were mainly based on reduced head models, the model developed in this thesis extends to the upper chest in order to encompass the implanted pulse generator.
The thesis remains on a pure electrical standpoint. Therefore, any result concerning the activation of the tissues surrounding the DBS electrode is done on the basis of the values obtained for the electrical potential distribution and for derived mathematical quantities such as its second directional derivative.
The knowledge of these electrical quantities can be used, for instance, to provide extracellular potentials needed as input data in electrical equivalent models of neurons, which allow to evaluate the response of these neurons to DBS.
Indeed, a remaining challenge would be to compare the numerical-based prediction of this thesis with actual data results obtained by direct physiological or clinical methods.
This would allow us to ascertain the relevance of quantities like the potential second derivative in the firing of neurones and to better estimate the threshold values actually needed to provoke this activation.

1.2 Outline

This section summarize the contents of the chapters of the thesis. Every chapter end with a selective bibliography complementing its material.

Chapter 2 aims to introduce the reader to the wide domain of bioelectromagnetism. After a definition of that term, a classification of the different applications of bioelectromagnetism is provided. Some explanations and the historical background are presented. Special care is taken in describing electrical stimulation, and more specifically deep brain stimulation (DBS). For this topic, a survey of the current state of the art is provided.

Chapter 3 introduces the needed electromagnetic theory and provides the mathematical equations for the static approximation of the general bioelectromagnetic problem. The numerical techniques available to solve this general bioelectromagnetic problem are then reviewed. Afterwards, this chapter explain the strategy used to estimate the electrical conductivity of the tissues, based on the diffusion tensor magnetic resonance imaging (DT-MRI). Finally the description of the selected numerical technique to solve the problem, the finite element (FE) method, is provided.

Chapter 4 depicts the realistic FE model developed in this thesis to provide the macroscopic effect of the DBS: the potential distribution generated in the brain tissues. The sensitivity of this potential distribution to the parameters defining the general bioelectromagnetic problem, namely the tissues conductivity and the boundary conditions, is thoroughly evaluated.

Chapter 5 uses the results obtained in Chapter 4 to evaluate the microscopic effects of DBS: the activation of neurons by the electric stimulation. This chapter first introduces to the reader the basic mechanisms of action of neural signal propagation. Electrical equivalent models of axons are then developed. Theses models are then combined with the potentials generated by the stimulation to provide the main results of this thesis: the volume of tissues activated (VTA) by the stimulation. Here also, the influence of the tissues' conductivity and of the applied boundary conditions is evaluated.

Chapter 6 summarize the thesis, provides its concluding remarks and outline the possible future research directions inspired by the outcome of this work.

1.3 Original contributions

The primary original contributions of this thesis are summarized in what follows.

Chapter 3, Section 3.3 presents an original approach to obtain anisotropic electrical conductivity values based on diffusion tensor magnetic resonance imaging, which does not need a segmentation process but takes directly advantage of the linearity observed between the water diffusion and the electrical conductivity.

Chapter 4, Section 4.2 proposes a model for DBS which extends to the chest, in order to model the whole DBS system in combination with a more sophisticated boundary condition. This original approach allows to evaluate the impact of the simplified boundary condition and the reduced geometry models usually applied in previous studies.

Chapter 5, Section 5.2 introduces two original methods to evaluate the VTA. The one using the fiber direction provided by the DT-MRI should be able to provide information relevant for the clinicians on the activation of anatomical structures.

2 State of the Art and historical background

This chapter provides a non-exhaustive review of bioelectromagnetism and its applications. Starting from the definition of bioelectromagnetism, it will sum up the history of this field of science and of its different kinds of applications. The emphasis will be put on the functional electrical stimulation, and more precisely on deep brain stimulation.

2.1 Bioelectromagnetism

The interactions between living organisms and electric phenomena have been known to humanity since at least the ancient Egypt civilization. Some hieroglyphs describing the electric catfish dated from 4000 B.C. have indeed been found [1].
Bioelectromagnetism is the area of science that studies these interactions. Until the middle of the nineteenth century, electromagnetism and bioelectromagnetism where sharing the same history as the first electromagnetic experiments were conducted on biological bodies, which were used as sensors. In the last 100 years, the fast improvement of the knowledge in electromagnetism has led to a better understanding of the basic bioelectromagnetism phenomena. This has enabled a full panoply of bioelectromagnetic applications.

Several aspects can be taken into account to classify the applications of bioelectromagnetism. In this thesis, a classification is proposed based on the nature and location of the source of the electromagnetic fields. It is categorized here below and summarized in Fig. 2.1.

- The interactions with **internal sources** refer to the electromagnetic fields and electric currents produced by any biological system. Firstly, we have the bioelectrical activity itself, source of life and of all the neurological process. But bodies or any other biological system can also use internal generated electricity to enhance their physiological senses or to create true weapons like the catfish electric bolt. The bioelectrical activity can be measured through the electric and magnetic fields it produces or through some macroscopic quantities like voltages. The study of the bioelectrical activity "per se" is not targeted in this thesis, although an obvious goal in the thesis would be to ascertain how some natural bioelectrical activity is affected by external man-made sources.

- The interactions with **external sources** include any modification of the biological behavior provoked by an external electromagnetic field or electric current. The word "external" includes sources like pacemakers that, although thanks to modern technology are nowadays implanted in the body and acts from within, remain essentially alien to the natural body. External sources can be classified as natural or artificial (man-made). Obvious examples of a natural external source is the Earth geomagnetic field and the solar electromagnetic radiation, but these phenomena are of no concern in this thesis.

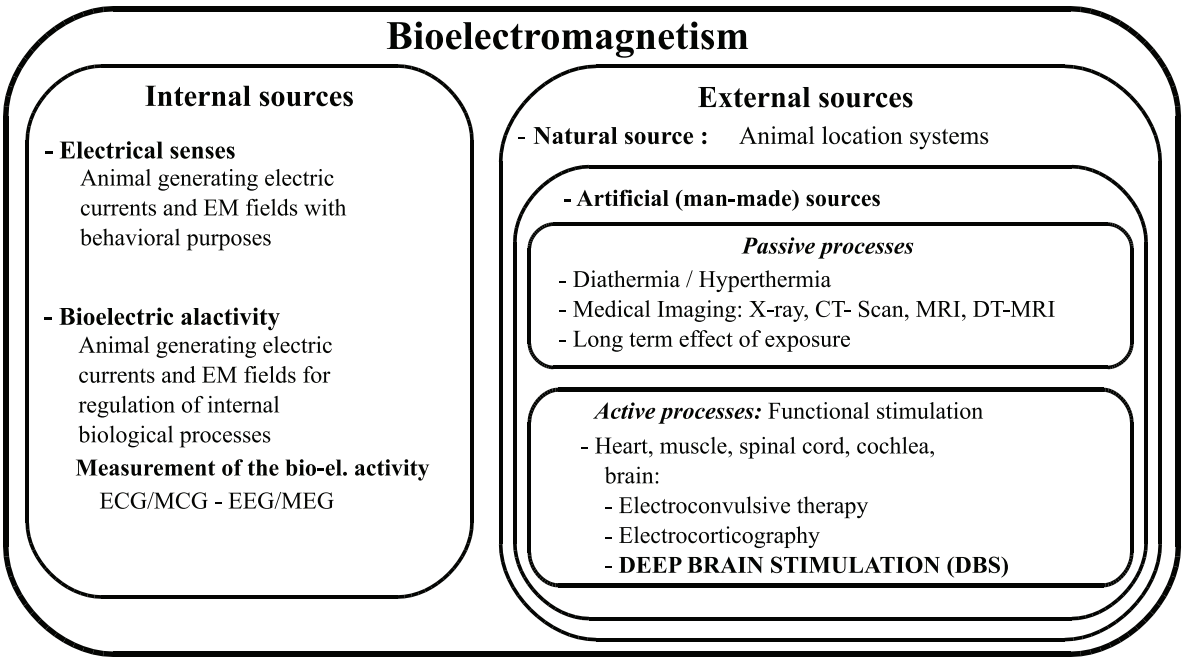

Figure 2.1: Diagram summarizing the applications of bioelectromagnetism. Bioelectromagnetism can be divided depending of the source of the fields, either external to the body or created by its own activity.

As for the external artificial sources, we will classify them, for the sake of clarity into two groups, depending on whether they are associated to "passive" or to "active" processes.

Passive processes are those that do not interact directly with the bioelectric process in the body (like neuronal signal transmission or heart beat). They will rather act at a molecular or even atomic scale, producing for instance heat (diathermia, or hyperthermia) or a orientation of hydrogen atoms along a magnetic field (some medical imaging techniques). Obviously, an indirect or retarded effect on the bioelectrical processes of the body cannot be excluded. This could be the aim of the interaction (like in many hyperthermia processes) or an undesirable effect that must be controlled and kept at bay (X-rays imaging).

Active processes are those intended to act directly on bioelectrical phenomena in order to stimulate or to inhibit them. Therefore these active processes can be also considered as **functional stimulation** processes. Functional stimulation is nowadays applied to many body parts, most frequently with medical applications in mind. A relevant example is the "**Deep Brain Stimulation**" (DBS), which is the subject of this thesis.

A final word must be said about these processes from the electrical engineer point of view. Active process must interact with the natural bioelectrical activities. Therefore they must use the same range of frequencies arising naturally in body-generated processes. These are relatively low frequencies, when considering the whole electromagnetic spectrum (Fig. 2.2).

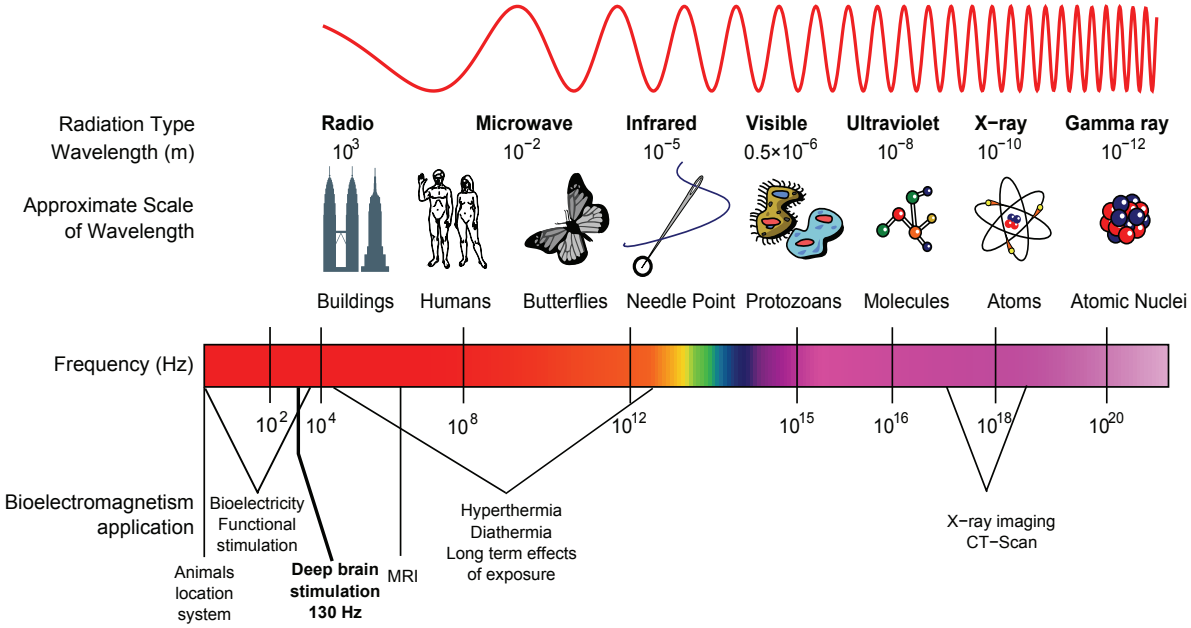

Figure 2.2: The bioelectromagnetic applications spread on the whole electromagnetic spectrum. The low frequencies below one kilohertz are where the bioelectricity generated by the living bodies takes place. The active interactions with external fields, which modify the behavior of the biological body, are also arising at these frequencies. At higher frequencies, from radiofrequency to the x-rays, the interactions are qualified as passive as they do not modify the behavior of the living bodies. (Adapted from Wikimedia Commons)

The range is roughly between DC and a few hundreds of Hz (Hertz), with DBS occupying the higher part of this range at, typically 100-150 Hz. This, by the way, justifies why DBS is termed in medical circles a "high frequency technique".
On the other hand, passive processes are intended not to elicit or to interfere directly with natural bioelectrical processes. This is obtained by using frequencies very far away from the natural range. The frequencies are typically in the high-end of the electromagnetic spectrum (see Fig. 2.2). They are selected either to provoke a specific molecular reaction (hyperthermia at 2.45 GHz, the resonant frequency of water molecules), to provide enough penetration power (X-rays tomography) or to induce any specific reaction at molecular or atomic level that can be used for imaging or for therapy purposes.

A succint description of the bioelectromagnetic interactions more deeply connected with the purpose of this thesis is given in the following sections.

2.1.1 Bioelectric activity

The transport of information through neurons is made by variation of ion concentration, creating electrical currents. Biological activity is the source of an important electrical activity through neural processes. This electrical activity generated by any living body is called bioelectricity. The chronology of bioelectricity measurements is now briefly reviewed.

Measurement of bioelectricity were first reported by Matteucci, who characterized a muscle impulse in frog muscle in 1838. In 1887, the first trace of electric activity of human heart, the *electrocardiogram* or ECG was measured by Waller.
Few years later, in 1924, the German psychiatrist Hans Berger made the first recording of the electrical activity of the brain, the *electroencephalogram* or EEG and identified the two major rhythms, α and β.
The development of modern electronics, and especially the transistor (Bardeen and Brattain, 1948), opened a new area in the use of these measurements. This indeed has allowed the instrumentation of bioelectromagnetism to be more reliable, miniaturized and made it portable and implantable.
According to Ampère, any electric current produces a magnetic field. In the biological electrical processes, the currents involved are so small that the measurement of the magnetic field they create was only possible in the second half of the twentieth century.
In 1963, Baule and McFee measured the first biomagnetic signal, the *magnetocardiogram* or MCG, arising from the heart activity.
The magnetic signals generated by the electric activity of the brain, the *magnetoencephalogram* or MEG, are so low that in practice their detection is only possible with the use of *Superconducting QUantum Interference Devices* (SQUID), working at the temperature of liquid helium (-269 $^\circ$ C). It is in 1970 that Cohen reported the first detection of MEG with the help of these devices. More information on the history of bioelectricity measurements can be found in [1].

Nowadays, applications of the measurements of the bioelectromagnetic activity of patients covers a wide and important area.
The monitoring of the heart beats through ECG is routinely used in medical practice and

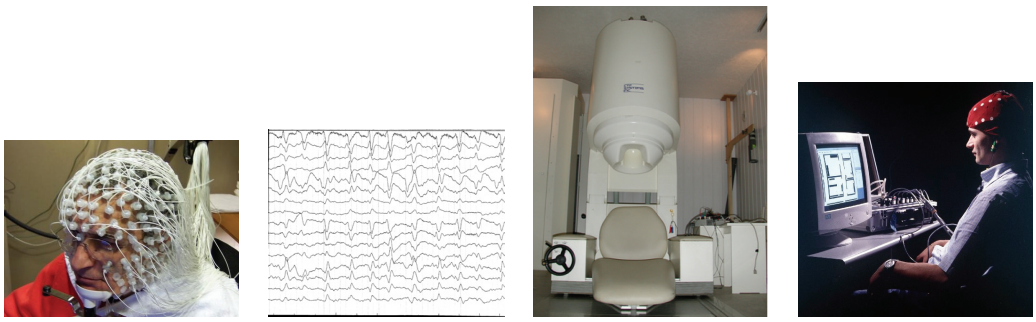

(a) EEG acquisition system (b) EEG recordings (c) MEG acquisition system (d) BCI system

Figure 2.3: Examples of measuring the bioelectric activity of the head.

hospitalization procedures. Moreover the study of patient ECG rhythm is also used to diagnose several troubles [2].
The development of the EEG and MEG and the use of high resolution medical imaging allowed neural science to elucidate some behavior of the brain. The study of EEG has several applications in cognitive science (motor process, sensory pathways, spatial tasks . . .) but also clinical applications such as epilepsy, head trauma, sleep disorders, sclerosis.
Another promising application of EEG is the brain computer interface (BCI), which uses the identification of EEG pattern to control computer interfaces [3]. The patient wears a cap containing about thirty electrodes that record the EEG. Particular mental states such as movement imagination, mental arithmetic or imagining someone, are differentiated among each other. A task can be executed according to the mental state activated. The applications are varied and are giving new hopes for autonomy for disabled people.

2.1.2 Interactions due to natural sources

An external electromagnetic field or an electric current containing the frequencies naturally present in the bioelectrical phenomena (lower end of the EM spectrum) has all the chances to interact with the biological process.
The source of the external field can be the Earth (magnetic field), but also another living creature, in which case Evolution usually guarantees the compatibility of frequencies.

Within the animal kingdom, several animal species have developed biological processes taking advantages of these interactions. Birds, fishes or turtles use the earth magnetic field to locate themselves during their annual migrations (Fig. 2.4(a)) [4]. Hammerhead sharks and similar species have developed electroreceptory sensory pores called ampullae of Lorenzini. These sensors are used to locate their preys as an electromagnetic field is generated by any movement of these preys (Fig. 2.4(b)).
When ancient Egyptians caught an electric catfish in their nets, the shock generated by the fish (450volts) forced the fishermen to release all the fish [1]. This is a typical example of excitation which should be classified as internal from the point of view of the catfish but

external otherwise! Other similar dual cases can be easily found.

(a) During their migrations, avian birds use the geomagnetic field as a compass to locate themselves.

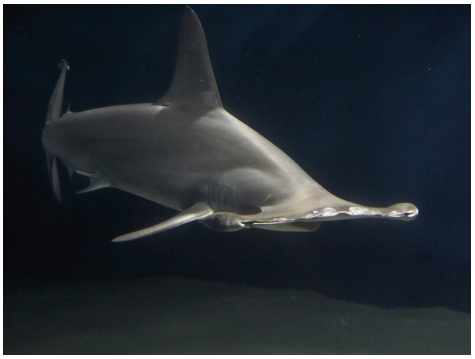

(b) Hammerhead shark uses electrosensitive organs to locate their preys.

Figure 2.4: Examples of animals using bioelectromagnetic interactions. (Taken from Wikimedia Commons)

2.1.3 Passive interactions due to artificial sources

When increasing the frequency of the electromagnetic field, the effects of the interaction between a field and a biological body does not act on biological processes anymore but rather on a structural or molecular processes. With the emergence of radiotelecommunications, the study of the effects of man-made sources of electromagnetic field has become an intensive research area. Most of the biological tissues are only interacting weakly with electromagnetic fields, absorbing the energy of the fields and converting it into heat. But long term effects of the exposure of biological tissues to electromagnetic fields remains unknown. Intensive studies are ongoing but as these researches have started lately, there is no clear answer yet on these effects [5].
Besides, therapeutic techniques using these kinds of interaction have been set up. The development of diathermy as a heating source is well established [6]. The use of hyperthermia is analog except that here the heating is used up to damage and even destroy tissues. As it has been observed, the malignant cells are generally more sensitive to thermal damage than are normal cells. The use of this technique to destroy cancers tumors that cannot be removed by classical surgery has thus rapidly increased.
But the main application of bioelectromagnetic interactions at high frequency is the medical imaging.

2.1.4 Medical Imaging

Medical imaging uses interactions between electromagnetic fields and biological tissues at high frequencies. The frequency used is highly dependant on the type of imaging. The typical range of frequency used for the magnetic resonance imaging (MRI) is around tens of megahertz while radiography uses X-rays.

The biological tissues modify in a specific way the field while interacting with it. The reflected or transmitted electromagnetic fields are then detected and analyzed to characterize the properties of the tissues. Therefore, it allows a non destructive anatomical reconstruction of the body.
Medical imaging has started at the end of the nineteenth century with the X-ray imagery, which used the fact that bones absorb more these ionizing rays than the other tissues (Fig. 2.5(a)). It provided the first non invasive imaging of the human internal anatomy.
In the 1970s, this technique was improved and upgraded to computed tomography scan (CT scan), which uses the same properties to provide a 3-dimensional view of a living body (Fig. 2.5(b)).
In the late 1970s, the availability of techniques to produce very strong magnetic fields led to the development of MRI (Fig. 2.5(c)), a technique that provides higher contrast between soft tissues than what previously obtained by CT scan. A strong magnetic field is used to align hydrogen nuclei, found in abundance in water molecules and therefore in biological tissues. A second electromagnetic field, which oscillates at radiofrequencies and is perpendicular to the main field, is then pulsed to push a portion of the protons out of alignment with the main field. These protons then drift back into alignment with the main field, emitting a detectable radiofrequency signal as they do so. Since protons in different tissues of the body realign at different speeds, the different structures of the body can be revealed. The MRI is the base of several new imaging technique such as diffusion tensor MRI (DT-MRI) (see Fig. 2.5(d)) [7], functional MRI [8] and so on.
The diffusion tensor imaging is obtained from a set of MRI taken for different direction of field. It have been shown that the diffusivity of water depends on the angle between the field and the fiber tract axis. The differences obtained for each direction allow to evaluate the preferred direction for diffusion of water. This measure of the anisotropic water diffusion in voxels provides an indication on the orientation of the fiber tracts in tissues [9]. This medical imaging technique will be used in this thesis to build a realistic anisotropic model of the brain tissues.

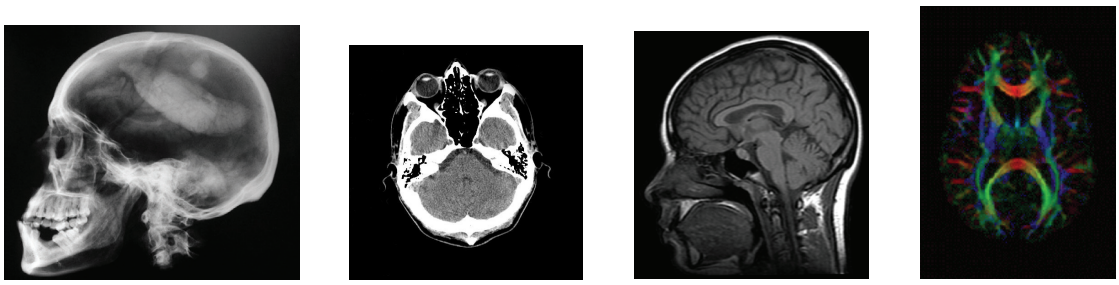

(a) sagittal X ray (b) axial CT (c) sagittal cut MRI (d) DTI color map

Figure 2.5: Examples of imaging the head.

The improvements of the medical imaging have allowed a better knowledge of the biological tissues leading to the development of numerous medical techniques to detects and treat disease. But biological bodies are also producing their own electromagnetic fields and using them as

a mean of transporting information.

2.2 Functional stimulation of excitable biological tissues

Functional electric or magnetic stimulation consists in stimulating either muscle [10] or nervous system [11] through the creation of an external electic or magnetic field in excitable tissues.

A short history

A succinct review of the historical experiments of functional stimulation is given here. During the eighteenth century, Galvani produced the most famous experiments in neuromuscular stimulation [1]: a dissected and prepared frog was lying on the same table as an electric machine. When his assistant touched with a scalpel the femoral nerve of the frog, sparks were simultaneously discharged in the nearby electric machine, and violent muscular contractions occurred. This is cited as the first documented experiment in neuromuscular electric stimulation. He then elaborated an experiment which is often cited as the classic study to demonstrate the existence of bioelectricity (see Fig. 2.6).

Afterwards, Green(1872) described a method used to awake surgical patients who where

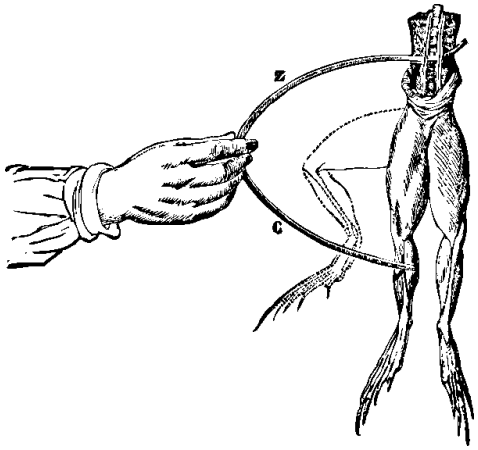

Figure 2.6: Stimulation of a frog leg muscle by Galvani. The *bimetallic arch of copper* (C) *and zinc* (Z), when in contact with the tissues, was producing a contraction of the muscle. Taken from [1]

deeply anesthetized. Using a battery generating about 300 volts, he applied this voltage to the patient between the neck and the lower ribs on the left side. It is documented that Green used this method successfully on five to seven patients who suffered sudden respiratory arrest and were without a pulse. Later, the development of induction coils by Faraday led to the first magnetic stimulation of nervous system(d'Arsonval,1896). A more detailed history of electric stimulation can be found in [1].

Magnetic and electric stimulation

The typical frequency range for this kind of stimulation is between static and hundreds of hertz. At these frequencies, it is correct to distinguish between electric and magnetic field effects. Therefore, the functional stimulation is either said magnetic or electric, depending on the field mainly used to interact with the excited tissues. The stimulation through electric fields, the most widespread one, and specific examples will be described in detail in the following subsections. Here some general remarks about magnetic and dielectric interactions are made.

In magnetic functional stimulation, time-varying magnetic fields are used to induce the stimulating current within the volume conductor. The fact that the magnetic field penetrates unattenuatedly through various classes of biological tissues implies several advantages. It avoids a high density of stimulating current at the contact and thus avoids pain sensation. It also avoids physical contact between the stimulating coil and the target tissue, which can be of primal importance in medical applications. The main application of magnetic stimulation of excitable tissues is transcranial stimulation of the motor cortex [12]. A coil is placed over the head of the patient, to produce a magnetic field. This field induces a current loop in the head (see Fig. 2.7) and produces the stimulation. Magnetic stimulation of the heart is also performed.

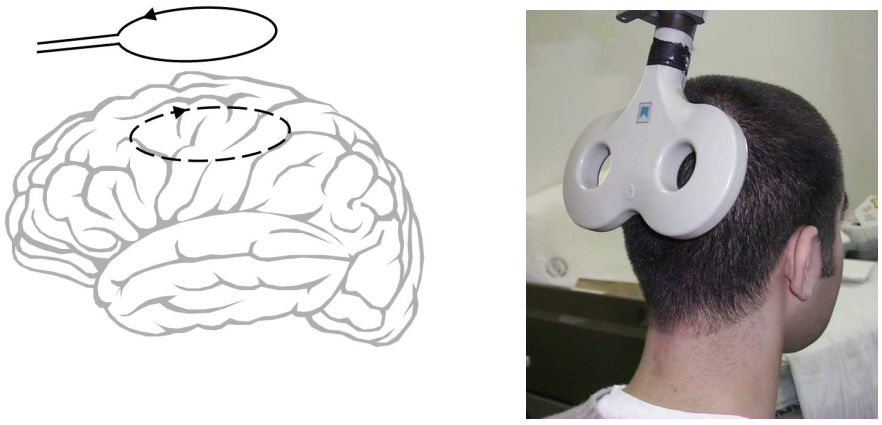

(a) (b)

Figure 2.7: In transcranial magnetic simulation, an external coil creates an magnetic field. This field (solid line) induces a loop current (dashed line) in the brain (a) which stimulates the targeted area. b) shows a transcranial magnetic stimulation device. Taken from scholarpedia and www.princeton.edu

Functional electric stimulation consists of direct injection of current in excitable tissues through electrodes. Opposite to magnetic stimulation, the stimulating electrodes must have a galvanic contact with the tissues. The electrode can either be placed on the outer boundary

of the body (transcutaneous stimulation) or implanted in direct contact with the targeted tissue.
In the case of transcutaneous stimulation, the currents go through the skin to reach the targeted area. This kind of stimulation is noninvasive but implies several drawbacks: activation of cutaneous pain receptors, poor selectivity and use of strong currents. These drawbacks are avoided when the electrode is directly implanted in the patient's body.
However, it is obvious that then a surgical intervention is required. Various applications for electrical stimulation exist and are discussed hereafter.

2.2.1 Heart stimulation

Electrical stimulation of the heart has played a major role in the development of electrical stimulations due to the importance of this organ. The heart can be electrically stimulated either to maintain the heartbeat regular (pacing) or to create an shock when the heart is having a seizure (defibrillation).
The modern era of cardiac stimulation started in 1952, when Zoll performed cardiac pacing for a duration of 20 minutes [13]. The first implantation of a cardiac pacemaker was accomplished in 1958 by Senning [1].
The actual pacemakers monitor the electrical rhythm of the heart. When the pacemaker detects a failed heartbeat within a normal beat-to-beat time period, it provides a short low voltage pulse through an electrode contact in the ventricle to stimulate it. This sensing and stimulating activity continues on a beat-by-beat basis.
The electrical stimulation of the heart can be achieved through several techniques explained hereafter.
Transcutaneous or external pacing is used in case of medical emergency. It consists in delivering pulses of electric current through electrodes located on each side of the patient's chest, which stimulate the heart to contract.
Transvenous pacing is the introduction of a pacemaker wire through a vein to the right part of the heart. The wire is then connected to an external pacemaker and electric pulses are then sent. When the stimulation is not necessary anymore, the system is removed.
Permanent pacing consists of the implantation of a whole system in the patient's body. The electrodes are placed in one or more chambers of the patient's heart and then connected to the pulse generator (see Fig. 2.8).

Another type of cardiac electrical stimulation is defibrillation. Prevost and Battelli found, in animal experiments, that low-voltage electric shocks induced ventricular fibrillation whereas high-voltage shocks did not. Instead, the latter defibrillated a fibrillating heart. In the 1930s Kouwenhoven used a 60 Hz current to defibrillate a dog heart [14]. Modern implantable defibrillators are designed to detect ventricular and atrial fibrillation and, if necessary, to deliver an electric jolt in order to drive back the heart to its sinusoidal rhythm.

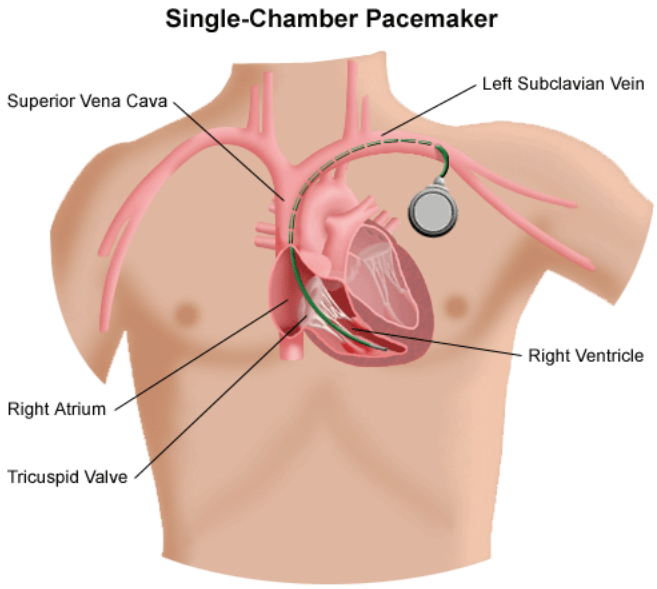

Figure 2.8: Schematic view of a single-chamber pacemaker. Taken from www.rush.edu

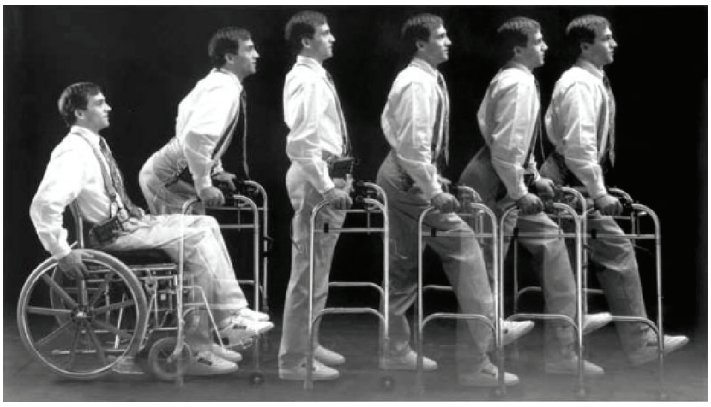

Figure 2.9: A transcutaneous multichannel neuroprosthesis system allows persons with paraplegia unbraced ambulation for home and short community distances. (Paradtep System User, couretsy of Sigmedic Inc., Fairborn, OH.), taken from [15].

2.2.2 Muscle stimulation

The neuromuscular electrical stimulation (NMES) is widely used in neurorehabilitation [10,15] and is directly inspired from Galvani's experiment.
Its application may include standing or ambulatory activities (see Fig. 2.9), upper-limb performance of activities of daily living and control of respiration or bladder function.
One of the therapeutic effects is motor relearning, which is defined as the "recovery of previously learned motor skills that have been lost following localized damage to central nervous

system". The stimulating system (neuroprosthesis) can be either implanted or transcutaneous.
NMES is initiated by the excitation of peripheral nervous tissues rather than the muscle cells. Indeed, the threshold for eliciting a nerve fiber action potential is 100 to 1000 times less than the threshold for muscle fiber stimulation. The strength of the resultant muscle contraction is modulated by adjusting the amplitude and the duration of the electric pulse stimulation. The frequencies used for NMES systems range from 10 to 50 Hz.

2.2.3 Spinal cord stimulation

Spinal cord stimulation is mainly used to treat chronic pain of neurologic origin [16]. Neurostimulation delivers low voltage electrical stimulation to the spinal cord or targeted peripheral nerve (see Fig. 2.10) to block the sensation of pain.
The mechanism(s) of action of this technique remains unclear. One theory, the Gate Control Theory, claims that neurostimulation activates the body's pain inhibitory system [17]. According to this theory, there is a gate in the spinal cord that controls the flow of noxious pain signals to the brain. An electrical activation of certain type of nerve fibers in the dorsal horn of the spinal cord inhibit these pain signals or "close the gate". The neurostimulation system, implanted in the epidural space, stimulates these pain-inhibiting nerve fibers, masking the sensation of pain.

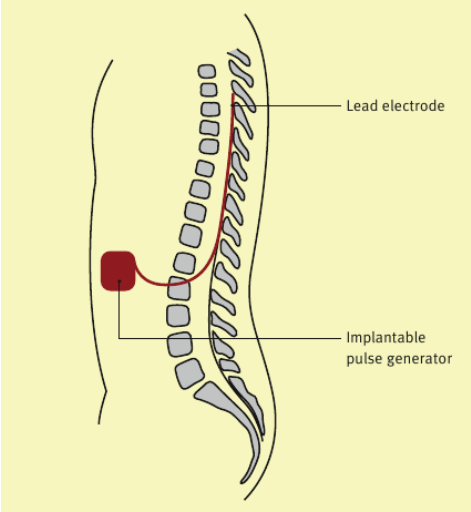

Figure 2.10: Artistic view of spinal cord stimulation.

2.2.4 Cochlea stimulation

A cochlear implant (CI) is a surgically implanted electronic device that provides a sense of sound to a person who is profoundly deaf or severely hard of hearing. The cochlear implant does not amplify sound like other hearing aids, but directly stimulates with an electric field

any functioning auditory nerves inside the cochlea. The system is made of an external microphone, a speech processor and an electrical stimulator. A transcutaneous link is used to transmit the signal processor output to the impanted electrodes (see Fig. 2.11).

In 1800, Volta reported placing an electrode in each of his ears and connecting the two electrodes to a series stack of electrochemical cells, whose potential was later estimated at 50 V. He reported hearing a "sound like a boiling viscid fluid" [18]. Wisely, he never repeated the study.
It is in the 1960s that the first studies on electrical stimulation of the cochlea have been reported [19]. The earliest cochlear implants used a single electrode placed inside the cochlea.

Introduction of cochlear implants that use multiple implanted electrodes and better processing of the signals from the microphone provided major improvements in speech discrimination. Using more than one electrode allowed to stimulate different parts of the cochlea and thereby different population of auditory nerve fibers with electrical signals derived from different frequency band of sound. Actual cochlear implants separate the sound spectrum using bandpass filters. Then a specific band of the sound spectrum activates the proper nerves thanks to the electrode.

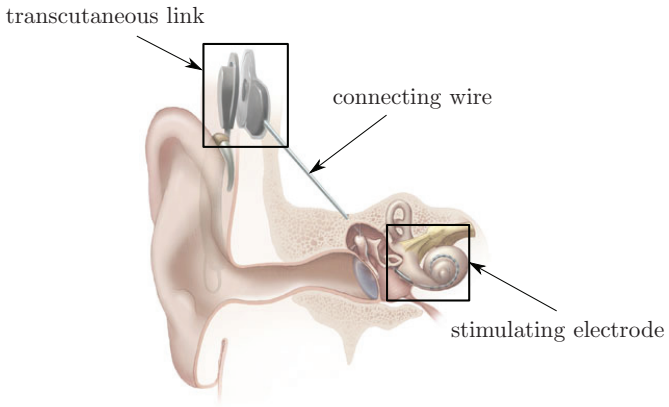

Figure 2.11: Cochlear stimulation implant. An external microphone and speech processor are analyzing the sound. Then the information is transmitted transcutaneously to the pulse generator, which delivers the pulse to the electrode through a wire to stimulate the cochlea. Adapted from www.thehearinginstitute.org

2.2.5 Brain stimulation

When speaking of electric neural stimulation, the brain is obviously the organ of main interest as it is the source of most of the neural processes.
One of the technique of stimulation of the brain is electroconvulsive therapy (or electroshock). This controversial psychiatric treatment is mainly used today to treat major depression which have not responded to other treatments, and in some cases to treat psychotic disorders.

Electrodes are usually placed on each part of the patient's head and a strong electrical stimulus is delivered to provoke a seizure to the patient. Whereas showing efficient results in some therapies, this technique is used as a last possibility as it has serious sides effects.
To stimulate a specific area of the brain while minimizing the side effects, intracranial electrical stimulation is performed either on the cortex (electrocorticography) or inside the brain. The intracranial electrical stimulation is called deep brain stimulation (DBS).

2.3 Deep brain stimulation

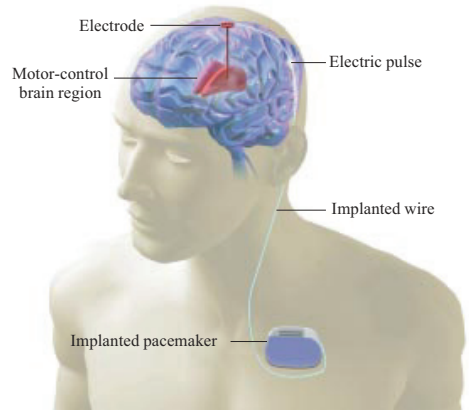

Figure 2.12: Artistic view of DBS. The implanted device is composed of a electrode which delivers an electric pulse to the target. The pulse is generated by an implanted pulse generator located in the chest and linked to the electrode via an implanted electric cable.

2.3.1 History

As knowledge on the brain structure increased, the understanding that the brain is an electrical organ and that it is not homogeneous were major steps in the progress of DBS.
At the end of the nineteenth century, the first experiments of brain stimulation were performed to treat epilepsy through electrocorticography (electric stimulation of the cortex). This technique was not yet ready to consider the implantation of a stimulating device [20]. Therefore, practitioners rather used ablation or lesioning of the targeted area than electrical stimulation. In a next step, surgical operations on the brain became much more efficient thanks to human stereotaxy. This technique consists in the localization of the structure to be treated through an atlas of the human brain. Once this structure is determined, an apparatus guided the surgical tools to reach the targeted area (see Fig. 2.13(a)). As there are issues of inaccurate targeting with stereotactic surgery, electrical stimulation was used since 1950 to determine the proximity of vital structures and thereby avoid them before creating stereotactic lesions. The development of the first totally implanted pacemaker by Chardack in 1960 and of the radiofrequency-driven spinal cord stimulator by Shealy in 1967 opened the era of implantable systems for DBS (see Fig. 2.12). In 1987, Benabid *et al.* [21], realized that chronic "high

frequency" stimulation (in fact just above 100 Hz) achieved similar effects than lesions at the same site of application, in a reversible, and therefore safer, manner than the former surgical lesioning (destructive or ablative) stereotactic methods (thalamotomies and pallidotomies). DBS of the subthalamic nucleus (STN) or globus pallidus (GPi) has largely replaced palidotomy in the treatment of the cardinal motor features of Parkinson's disease (resting tremor, rigidity, bradykinesia). The clinical benefits of the DBS are so encouraging that several pioneer studies have begun to examine its utility for dystonia [22], epilepsy [23] and obsessive-compulsive disorder.
The interested reader will find a more detailed history of DBS in the review of Schwalb and Hamani [20].

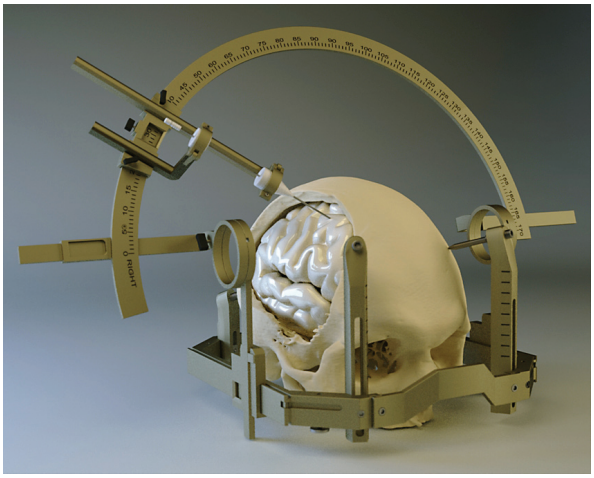

(a) To apply precise surgery to an area previously selected with imaging of a patient and anatomic atlas, a stereotactic frame is used. Courtesy of Benjamin Brosdau

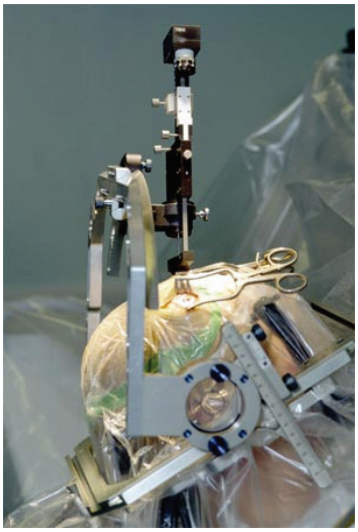

(b) During DBS surgery, the patient is still conscious. Taken from Wikimedia Commons

Figure 2.13: Illustration of the DBS surgery tool and procedure

2.3.2 Set up procedure

The medical procedure used to install DBS devices is the following: The goal of stereotactic surgery is to reach a selected area (or target) of stimulation with optimal accuracy. The first step is to locate this area in the patient brain.
To do so, the practician uses an MRI of the patient's head and a stereotactic atlas to identify the target's position (subthalamic nucleus in the case of Parkison's disease).
Once the target located in the patient's anatomy, a trajectory avoiding vital organs such as veins or specific functional areas is selected for the insertion of the electrode. The stereotactic frame is then set up to guide the surgical tools along this trajectory during the surgery.
The surgery then starts and during this phase, the patient remains conscious as the evaluation

of the effects of the stimulation requires his participation. Openings are made under local anesthesia in the patients scalp in order to reach the skull. The skull is then drilled to give access to the brain.
First, a microelectrode is inserted in the brain and records the electric noise of the structures crossed during the course to reach the target. The characteristic electrical noise signature of the subthalamic nucleus allows to re-enforce the localization of this structure. But this procedure increases the risks of bleeding and extends the duration of the procedure.
The introduction of the stimulating electrode takes place and stimulation starts few millimeters over the target to test the patient's response to stimulation. Afterwards, the parameters of stimulation are changed (frequency, amplitude) and several neurologic tests are proceeded to evaluate how the patient's symptoms evolve. The stimulating electrode is then introduced deeper and the procedure is started again.
The final position of the electrode and the stimulation parameters are chosen according to maximizing the patient's response to stimulation while minimizing the side effects.
Once the electrode is placed adequately, the system is internalized and linked to the pulse generator located under the collarbone. A picture illustrating the DBS surgery is shown in Fig. 2.13(b).

2.3.3 Present understanding

The therapeutic effectiveness of DBS had for consequences that the clinical applications have preceded the scientific understanding of the underlying mechanism(s) of action. We are only in the preliminary stages of understanding the effects of DBS because of the limited number of years that have been available for scientific investigation and the sheer complexity of the problems being addressed. However, a critical mass of talented clinicians and scientists dedicated to addressing the mechanisms of DBS now exists. In turn, collaborative efforts are forming to address the effects and mechanisms of DBS from the molecular, cellular, network, system, and behavioral levels.

There exist long-standing controversies over different hypotheses to explain the therapeutic benefit of DBS. Addressing the effects of high-frequency DBS confronts investigators with a paradox of how stimulation (traditionally thought to activate neurons) can result in similar therapeutic outcomes as lesioning target structures. In turn, there exist two general philosophies on the effects of DBS: (1) DBS generates a functional ablation by suppressing or inhibiting the structure being stimulated, or (2) DBS results in activation of the stimulated structures that are transmitted throughout the network. It is possible that the therapeutic mechanisms that underlie DBS most likely represent a combination of several phenomena: such as depolarization blockade, synaptic inhibition, synaptic depression and stimulation-induced modulation of pathologic network activity [24, 25].

To address these questions, models have been set up analyzing several aspects of the different levels of mechanism. These models will be reviewed in the following.

Electric field released form the electrode

The electrical field generated by DBS is a three-dimensional complex phenomenon that is distributed throughout the brain. The field distribution is affected by the electrical properties of the surrounding tissues [26, 27]. These electrical properties depend on the electrode position in the brain anatomy, but also of the presence of a capacitive tissue at the interface between electrode contact and brain tissue. Indeed the implantion of the stimulation electrode induces the creation of cicatricial tissues. These tissues are directly influencing the potential distribution created by the stimulation [28–30]. The design of the electrode also affects the shape of the electric field [31–34]. The presence of cystic cavities in the tissues surrounding the electrode have also been investigated in [35], and showed a deformation of the electric potentials released during stimulation.
The electric field distribution plays an important role in DBS. Indeed, the response of an individual neuron to the applied field is related to the second derivative of the extracellular potential distribution along each process [36]. In turn, each neuron (or neural process) surrounding the electrode will be subject to both depolarizing and hyperpolarizing effects from the stimulation [37]. As a result, a neuron can either be activated or suppressed in response to extracellular stimulation in different ways and in different portions of the neuron, depending on its positioning with respect to the electrode and the stimulation parameters used [38].
Activation or inhibition of the different classes of neurons surrounding the electrode can result in dramatically different physiologic and/or behavioral outputs. Given the stimulation parameters and electrode geometries presently used, it is likely that DBS directly affects local cells, afferent inputs, and fibers of passage. This complicates our ability to specifically address the role of activation/inhibition of each of these tissues in the mechanism of DBS.

Effect of DBS at the single cell level

When stimulating within the central nervous system, the electrode is placed within a complex volume conductor where there exist three general classes of neurons that can be affected: local cells, afferent inputs, and fibers of passage. Local cells represent neurons that have their cell body in close proximity to the electrode. Afferent inputs represent neurons that project to the region near the electrode and whose axon terminals make synaptic connections with local cells. Fibers of passage represent neurons where both the cell body and axon terminals are far from the electrode, but the axonal process of the neuron traces a path that comes in close proximity to the electrode. Each of these classes of neurons can be affected by extracellular stimulation.
The use of multicompartment cable models of neurons coupled to extracellular electrical fields provides the opportunity to study the effects of stimulation on neural activity. The first studies of modelling extracellular stimulation date back to McNeal (1976) [39] and have been used extensively in the study of electrical stimulation nerve stimulation [32, 40–42]. More recently, investigations have addressed the biophysical mechanisms of action potential initiation during extracellular brain stimulation on neuron models, [38, 43–45] and on axons models [26–28, 31, 32, 46, 47].
In general, modelling the excitation of neurons relies on representing the neural membrane

with multiple compartments of electrical circuits (conductance and capacitance in parallel or series) [48]. Models of extracellular stimulation allow analysis of the effects of stimulation of all the neural elements surrounding the electrode simultaneously, something impossible to achieve experimentally. However, the strengths of modelling are tempered by the necessary simplifications made in any reasonable model.

Modelling the volume of tissue influenced dy deep brain stimulation

Our understanding of the size and shape of the three-dimensional volume of tissue directly influenced by DBS is limited. The subthalamic nucleus represents the most common target of DBS technology. However, the subthalamus nucleus is a relatively small structure surrounded by several other nuclei and multiple fiber tracts. One limitation of subthalamic nucleus DBS is the low threshold for side effects such as tetanic muscle contraction, speech disturbances, and ocular deviation [49]. Activation of highly anisotropic fiber tracks that surround the subthalamic nucleus have been implicated in many of the side effects associated with DBS. However, our limited understanding of the neural response to stimulation and the three-dimensional anisotropic and inhomogeneous tissue medium surrounding the electrodes makes predicting the volume of tissue influenced challenging.
The recent work of McIntyre's group evaluated a volume of tissue activated. A finite element model is used to solve for the electrical field generated in the tissue medium by DBS. The diffusion tensor imaging was used to estimate the electrical conductivity of the surrounding tissues [50]. The field was applied to detailed multicompartment cable models of myelinated axons to determine stimulation parameters suprathreshold for axonal activation. Based on the results from stimulation of the axon models, estimates of the spatial extent of activation in the anisotropic and inhomogeneous tissue medium were made using the second difference of the potential distribution [26, 27]. Nevertheless, the use of this second difference of the potential is directional and needs an assumption on the fibers direction.

Clinical parameters used for DBS

The general therapeutic stimulation parameters for DBS (monopolar cathodic; 1 to 5 V stimulus amplitude; 60 to 200 μs stimulus pulse duration; 120 to 180 Hz stimulus frequency) have been derived empirically by trial and error [51]. This trial-and-error selection of the stimulation parameters has been effective because of the nearly immediate effects of DBS on the control of tremor and Parkinsonian motor symptoms. However, new therapies utilizing DBS technology will not allow such ease of titration. The beneficial effects of stimulation can take weeks to months to manifest in dystonia and obsessive-compulsive disorder, and it is unclear which electrode geometries, stimulation amplitudes, pulse durations, and frequencies are most effective for these new therapeutic directions. Therefore, the elaboration of a reliable model of the physical phenomens involved during DBS is of paramount relevance to elucidate the underlying mechanism(s) of action of DBS.

2.4 Conclusion

This chapter introduced some aspects of bioelectromagnetism, which consists of the interaction of electromagnetic fields with biological bodies. These interactions can be divided into two groups, depending on the source of the electromagnetic fields. The bioelectricity concerns the sources produced by biological processes inside the body.
The interactions between the electromagnetic fields produced by external sources and biological bodies are used in several applications such as medical imaging. One of these applications is the deep brain stimulation.
Deep brain stimulation is the electrical stimulation of a brain structure through an implanted electrode. Whereas this technique is widely used, its mechanisms of action are still not well understood and subject to research.
The aim of this thesis is to build an electrical model to predict the potential distribution generated by the electric stimulation and to evaluate the impact of the stimulation on the surrounding tissues.

Bibliography

[1] J. Malmivuo and R. Plonsey, *Bioelectromagnetism*. Oxford University Press, 1995.

[2] P. L. Nunez and R. Srinivasan, *Electric Fields of the Brain - The Neurophysics of EEG*, 2nd ed. Oxford University Press, 2006.

[3] J. R. Wolpaw, N. Birbaumer, W. J. Heetderks, D. J. McFarland, P. H. Peckham, G. Schalk, E. Donchin, L. A. Quatrano, C. J. Robinson, and T. M. Vaughan, "Brain-computer interface technology: a review of the first international meeting." *IEEE Trans Rehabil Eng*, vol. 8, no. 2, pp. 164–173, Jun 2000.

[4] J. L. Kirschvink, "Magnetoreception: Homing in on vertebrates," *Nature*, vol. 390, no. 6658, pp. 339–340, Nov. 1997. [Online]. Available: http://dx.doi.org/10.1038/36986

[5] "What are electromagnetic fields?" World Health Organization, Tech. Rep., 2004. [Online]. Available: http://www.who.int/peh-emf/about/WhatisEMF/en/

[6] J. M. Osepchuk, *Biological effects of Electromagnetic Radiation*. IEEE Press, 1983.

[7] D. Le Bihan, J. F. Mangin, C. Poupon, C. A. Clark, S. Pappata, N. Molko, and H. Chabriat, "Diffusion tensor imaging: concepts and applications," *J. Magn. Reson. Imaging.*, vol. 13, no. 4, pp. 534–546, Apr. 2001.

[8] K. K. Kwong, J. W. Belliveau, D. A. Chesler, I. E. Goldberg, R. M. Weisskoff, B. P. Poncelet, D. N. Kennedy, B. E. Hoppel, M. S. Cohen, and R. Turner, "Dynamic magnetic resonance imaging of human brain activity during primary sensory stimulation." *Proc Natl Acad Sci U S A*, vol. 89, no. 12, pp. 5675–5679, Jun 1992.

[9] P. J. Basser, J. Mattiello, and D. LeBihan, "Mr diffusion tensor spectroscopy and imaging." *Biophys J*, vol. 66, no. 1, pp. 259–267, Jan 1994.

[10] O. K. Sujith, "Functional electrical stimulation in neurological disorders." *Eur J Neurol*, vol. 15, no. 5, pp. 437–444, May 2008. [Online]. Available: http://dx.doi.org/10.1111/j.1468-1331.2008.02127.x

[11] P. L. Gildenberg, "Evolution of neuromodulation." *Stereotact Funct Neurosurg*, vol. 83, no. 2-3, pp. 71–79, 2005. [Online]. Available: http://dx.doi.org/10.1159/000086865

[12] M. Kobayashi and A. Pascual-Leone, "Transcranial magnetic stimulation in neurology." *Lancet Neurol*, vol. 2, no. 3, pp. 145–156, Mar 2003.

[13] P. M. Zoll, "Resuscitation of the heart in ventricular standstill by external electric stimulation." *N Engl J Med*, vol. 247, no. 20, pp. 768–771, Nov 1952.

[14] W. B. Kouwenhoven, "Effects of electricity on the human body." *Ind Med Surg*, vol. 18, no. 7, p. 269, Jul 1949.

[15] L. R. Sheffler and J. Chae, "Neuromuscular electrical stimulation in neurorehabilitation." *Muscle Nerve*, vol. 35, no. 5, pp. 562–590, May 2007. [Online]. Available: http://dx.doi.org/10.1002/mus.20758

[16] M. Chaudhari and P. Mackenzie, "Implantable technology for pain management," *Anaesthesia and Intensive Care Medicine*, vol. 9, no. 2, pp. 69–74, 2008.

[17] R. Melzack and P. D. Wall, "Pain mechanisms: a new theory." *Science*, vol. 150, no. 699, pp. 971–979, Nov 1965.

[18] F. A. Spelman, "The past, present, and future of cochlear prostheses." *IEEE Eng Med Biol Mag*, vol. 18, no. 3, pp. 27–33, 1999.

[19] A. R. Moller, "History of cochlear implants and auditory brainstem implants." *Adv Otorhinolaryngol*, vol. 64, pp. 1–10, 2006. [Online]. Available: http://dx.doi.org/10.1159/000094455

[20] J. M. Schwalb and C. Hamani, "The history and future of deep brain stimulation." *Neurotherapeutics*, vol. 5, no. 1, pp. 3–13, Jan 2008. [Online]. Available: http://dx.doi.org/10.1016/j.nurt.2007.11.003

[21] A. Benabid, P. Pollak, A. Louveau, S. Henry, and J. De Rougemont, "Combined (thalamotomy and stimulation) stereotactic surgery of the vim thalamic nucleus for bilateral parkinson disease," *Applied Neurophysiology*, vol. 50, no. 1-6, pp. 344–346, 1987.

[22] A. L. Benabid, "Deep brain stimulation for parkinson's disease." *Curr Opin Neurobiol*, vol. 13, no. 6, pp. 696–706, Dec 2003.

[23] W. H. Theodore and R. S. Fisher, "Brain stimulation for epilepsy." *Lancet Neurol*, vol. 3, no. 2, pp. 111–118, Feb 2004.

[24] A. L. Benabid, A. Benazzous, and P. Pollak, "Mechanisms of deep brain stimulation." *Mov Disord*, vol. 17 Suppl 3, pp. S73–S74, 2002.

[25] J. L. Vitek, "Mechanisms of deep brain stimulation: excitation or inhibition." *Mov Disord*, vol. 17 Suppl 3, pp. S69–S72, 2002.

[26] C. C. McIntyre, S. Mori, D. L. Sherman, N. V. Thakor, and J. L. Vitek, "Electric field and stimulating influence generated by deep brain stimulation of the subthalamic nucleus." *Clin Neurophysiol*, vol. 115, no. 3, pp. 589–595, Mar 2004. [Online]. Available: http://dx.doi.org/10.1016/j.clinph.2003.10.033

[27] C. R. Butson, S. E. Cooper, J. M. Henderson, and C. C. McIntyre, "Patient-specific analysis of the volume of tissue activated during deep brain stimulation." *Neuroimage*, vol. 34, no. 2, pp. 661–670, Jan 2007. [Online]. Available: http://dx.doi.org/10.1016/j.neuroimage.2006.09.034

[28] C. R. Butson and C. C. McIntyre, "Tissue and electrode capacitance reduce neural activation volumes during deep brain stimulation." *Clin Neurophysiol*, vol. 116, no. 10, pp. 2490–2500, Oct 2005. [Online]. Available: http://dx.doi.org/10.1016/j.clinph.2005.06.023

[29] N. Yousif, R. Bayford, P. G. Bain, and X. Liu, "The peri-electrode space is a significant element of the electrode-brain interface in deep brain stimulation: A computational study." *Brain Res Bull*, vol. 74, no. 5, pp. 361–368, Oct 2007. [Online]. Available: http://dx.doi.org/10.1016/j.brainresbull.2007.07.007

[30] N. Yousif, R. Bayford, S. Wang, and X. Liu, "Quantifying the effects of the electrodebrain interface on the crossing electric currents in deep brain recording and stimulation," *Neuroscience*, vol. 152, no. 3, pp. 683–691, March 2008. [Online]. Available: http://dx.doi.org/10.1016/j.neuroscience.2008.01.023

[31] C. R. Butson, C. B. Maks, and C. C. McIntyre, "Sources and effects of electrode impedance during deep brain stimulation." *Clin Neurophysiol*, vol. 117, no. 2, pp. 447–454, Feb 2006. [Online]. Available: http://dx.doi.org/10.1016/j.clinph.2005.10.007

[32] C. R. Butson and C. C. McIntyre, "Role of electrode design on the volume of tissue activated during deep brain stimulation." *J Neural Eng*, vol. 3, no. 1, pp. 1–8, Mar 2006, electrode design. [Online]. Available: http://dx.doi.org/10.1088/1741-2560/3/1/001

[33] C. C. McIntyre and W. M. Grill, "Finite element analysis of the current-density and electric field generated by metal microelectrodes," *Ann. Biomed. Eng.*, vol. 29, no. 3, pp. 227–235, Mar. 2001.

[34] X. F. Wei and W. M. Grill, "Current density distributions, field distributions and impedance analysis of segmented deep brain stimulation electrodes." *J Neural Eng*, vol. 2, no. 4, pp. 139–147, Dec 2005. [Online]. Available: http://dx.doi.org/10.1088/1741-2560/2/4/010

[35] M. Astrm, J. D. Johansson, M. I. Hariz, O. Eriksson, and K. Wrdell, "The effect of cystic cavities on deep brain stimulation in the basal ganglia: a simulation-based study." *J Neural Eng*, vol. 3, no. 2, pp. 132–138, Jun 2006. [Online]. Available: http://dx.doi.org/10.1088/1741-2560/3/2/007

[36] F. Rattay, "Analysis of models for external stimulation of axons," *IEEE Trans Biomed Eng*, 1986.

[37] C. C. McIntyre and W. M. Grill, "Excitation of central nervous system neurons by nonuniform electric fields." *Biophys J*, vol. 76, no. 2, pp. 878–888, Feb 1999.

[38] ——, "Extracellular stimulation of central neurons: influence of stimulus waveform and frequency on neuronal output." *J Neurophysiol*, vol. 88, no. 4, pp. 1592–1604, Oct 2002.

[39] D. R. McNeal, "Analysis of a model for excitation of myelinated nerve." *IEEE Trans Biomed Eng*, vol. 23, no. 4, pp. 329–337, Jul 1976.

[40] P. J. Basser and B. J. Roth, "New currents in electrical stimulation of excitable tissues." *Annu Rev Biomed Eng*, vol. 2, pp. 377–397, 2000. [Online]. Available: http://dx.doi.org/10.1146/annurev.bioeng.2.1.377

[41] J. H. Frijns, S. L. de Snoo, and J. H. ten Kate, "Spatial selectivity in a rotationally symmetric model of the electrically stimulated cochlea." *Hear Res*, vol. 95, no. 1-2, pp. 33–48, May 1996.

[42] J. Holsheimer, "Computer modelling of spinal cord stimulation and its contribution to therapeutic efficacy." *Spinal Cord*, vol. 36, no. 8, pp. 531–540, Aug 1998.

[43] C. C. McIntyre, W. M. Grill, D. L. Sherman, and N. V. Thakor, "Cellular effects of deep brain stimulation: model-based analysis of activation and inhibition." *J Neurophysiol*, vol. 91, no. 4, pp. 1457–1469, Apr 2004. [Online]. Available: http://dx.doi.org/10.1152/jn.00989.2003

[44] C. C. McIntyre, S. Miocinovic, and C. R. Butson, "Computational analysis of deep brain stimulation." *Expert Rev Med Devices*, vol. 4, no. 5, pp. 615–622, Sep 2007. [Online]. Available: http://dx.doi.org/10.1586/17434440.4.5.615

[45] S. Miocinovic, M. Parent, C. R. Butson, P. J. Hahn, G. S. Russo, J. L. Vitek, and C. C. McIntyre, "Computational analysis of subthalamic nucleus and lenticular fasciculus activation during therapeutic deep brain stimulation." *J Neurophysiol*, vol. 96, no. 3, pp. 1569–1580, Sep 2006. [Online]. Available: http://dx.doi.org/10.1152/jn.00305.2006

[46] C. R. Butson and C. C. McIntyre, "Differences among implanted pulse generator waveforms cause variations in the neural response to deep brain stimulation." *Clin Neurophysiol*, vol. 118, no. 8, pp. 1889–1894, Aug 2007, electrode Parameters. [Online]. Available: http://dx.doi.org/10.1016/j.clinph.2007.05.061

[47] S. Sotiropoulos and P. Steinmetz, "Assessing the direct effects of deep brain stimulation using embedded axon models," *Journal of Neural Engineering*, vol. 4, no. 2, pp. 107–119, 2007. [Online]. Available: http://stacks.iop.org/1741-2552/4/107

[48] A. L. Hodgkin and A. F. Huxley, "A quantitative description of membrane current and its application to conduction and excitation in nerve." *J Physiol*, vol. 117, no. 4, pp. 500–544, Aug 1952.

[49] P. Krack, V. Fraix, A. Mendes, A.-L. Benabid, and P. Pollak, "Postoperative management of subthalamic nucleus stimulation for parkinson's disease." *Mov Disord*, vol. 17 Suppl 3, pp. S188–S197, 2002.

[50] D. S. Tuch, V. J. Wedeen, A. M. Dale, J. S. George, and J. W. Belliveau, "Conductivity tensor mapping of the human brain using diffusion tensor MRI," *Proc. Natl. Acad. Sci. USA*, vol. 98, no. 20, pp. 11 697–11 701, Sep. 2001.

[51] E. Moro, R. J. A. Esselink, J. Xie, M. Hommel, A. L. Benabid, and P. Pollak, "The impact on parkinson's disease of electrical parameter settings in stn stimulation." *Neurology*, vol. 59, no. 5, pp. 706–713, Sep 2002.

3 Bioelectric head model

To help the clinicians understanding the mechanism(s) activated by deep brain stimulation (DBS), a better knowledge of the physical phenomena involved during the electrical stimulation needs to be provided.
Bioelectromagnetic phenomena, as any other electromagnetic phenomena, are governed by Maxwell equations. In the bioelectromagnetism applications of interest here (deep brain stimulation and related techniques) the tissues can be considered as conductive media. This leads to a general formulation of Maxwell equations for bioelectromagnetic problems that will be reviewed in Section 3.1.
These equations must be applied to a model of the involved biological region. In the case studied here, this region extends to the head, neck and upper chest. Section 3.2 briefly describes the possible geometrical and constitutive models and explains advantages and drawbacks of each one. The conductivity of each tissue can be estimated or determined by many different techniques. The diffusion tensor magnetic resonance imaging (DT-MRI) is favored here as documented in Section 3.3.
Finally, among the well established techniques to discretize Maxwell equations and transform them in a set of algebraic equations that can be solved in a computer, the finite element (FE) method has been selected, as this approach is very well adapted to high anisotropic and inhomogeneous problems. The particular version of the FE method used here is described in Section 3.4.

3.1 Mathematical formulation of the general bioelectric problem

3.1.1 Maxwell's equations

The equations governing the electric and magnetic phenomena are the Maxwell equations [1]:

$$\nabla \cdot \mathbf{D} = \rho \tag{3.1a}$$

$$\nabla \times \mathbf{E} = -\frac{\partial \mathbf{B}}{\partial t} \tag{3.1b}$$

$$\nabla \cdot \mathbf{B} = 0 \tag{3.1c}$$

$$\nabla \times \mathbf{H} = \mathbf{J} + \frac{\partial \mathbf{D}}{\partial t} \tag{3.1d}$$

where $\mathbf{D}$ is the electric displacement, ρ the electric free charge density, $\mathbf{H}$ and $\mathbf{B}$ the magnetic field and induction, $\mathbf{E}$ the electric field, $\mathbf{J}$ the electric current density and ∇, a symbol spelt as "del" or "nabla", is the classic first-order differential operator with respect to the spatial coordinates.
Equation (3.1a) arises from *Gauss' law* and relates the electric displacement $\mathbf{D}$ to the source that generates it, namely the source density ρ.
Equation (3.1b) arises from *Faraday's law* and states that a time varying magnetic field $\mathbf{H}$ induces an electric field $\mathbf{E}$.
Equation (3.1c) is known as *Gauss' law for magnetism* and recognize that no magnetic charges exist and hence that $\mathbf{B}$ must be solenoidal.
Equation (3.1d) is a statement of *Ampere's law* that the line integral of a magnetic field $\mathbf{H}$ around a closed loop equals the total current through the loop.

By taking the divergence of (3.1d) and introducing on it the equation (3.1a) we get :

$$\nabla \cdot \mathbf{J} + \frac{\partial \rho}{\partial t} = 0. \tag{3.2}$$

This is the continuity equation of paramount relevance for our calculations.
In the frequency range of the DBS (below 1000 Hz), the fields and its sources vary slowly and hence their time derivatives can be neglected. This means that on one side the continuity equation (3.2) reduces to :

$$\nabla \cdot \mathbf{J} = 0 \tag{3.3}$$

showing that the total current density must be solenoidal (or divergenceless). On the other hand electric and magnetic phenomena are decoupled since Maxwell equations (3.1) reduce to

$$\nabla \cdot \mathbf{D} = \rho \tag{3.4a}$$

$$\nabla \times \mathbf{E} = 0 \tag{3.4b}$$

$$\nabla \cdot \mathbf{B} = 0 \tag{3.4c}$$

$$\nabla \times \mathbf{H} = \mathbf{J}. \tag{3.4d}$$

Under these conditions, biological media behave as electrolytes and the capacitive and inductive properties of tissues can be neglected in a first approximation [2]. In response to any excitation current density $\mathbf{J}_S$ (the so called source or impressed current), a conduction or ohmic current density $\mathbf{J}_\Omega$ will be induced everywhere in the medium. Therefore, the total current density to which equations (3.3) and (3.4d) apply is

$$\mathbf{J} = \mathbf{J}_S + \mathbf{J}_\Omega. \tag{3.5}$$

The impressed current $\mathbf{J}_S$ is supposed to be the primary source of the problem and unaffected by the existing fields. It could be the current generated by an external source or the current entering a cell through its membrane.
The induced current will obey to the Ohm's law and will be proportional to the total electric field according to the equation

$$\mathbf{J}_\Omega = \bar{\bar{\sigma}} \cdot \mathbf{E} \tag{3.6}$$

where $\bar{\bar{\sigma}}$ is the electrical conductivity. This tensorial quantity, mathematically represented by a 3x3 matrix, is the most important physical parameter to be assigned to the biological tissues in this study. Knowing the electrical conductivity at every point of a tissue accounts to know the electrical field associated to a given current in this point or, viceversa, to reconstruct the induced ohmic current from the knowledge of the electric field.
Finally, it is worth recalling an obvious mathematical property. The conductivity $\bar{\bar{\sigma}}$ being a tensor (resulting from the tissues anisotropy), the vectors $\mathbf{J}$ and $\mathbf{E}$ (current and field) will not be in general parallel inside a biological tissue.

The basic differential equation

Introducing equations (3.5) and (3.6) in (3.3) yields

$$\nabla \cdot (\bar{\bar{\sigma}}\mathbf{E}) = -\nabla \cdot \mathbf{J}_S \tag{3.7}$$

This differential equation can be used to obtain $\mathbf{E}$ when $\bar{\bar{\sigma}}$ and $\mathbf{J}_S$ are known.

The static electric potential

Frequently, one speaks about electric potentials rather than about electric fields. Moreover, standard technologies and devices are usually calibrated in terms of "voltages" or potential differences between two electrodes measured in volts.
The mathematical relationship between field $\mathbf{E}$ and potential V is easily set up in the static approximation since the equation (3.4b) implies that

$$\mathbf{E} = -\nabla V = -\text{grad}\, V. \tag{3.8}$$

It is also well known that from a computational point of view it is much easier to deal with the scalar quantity V than with vector quantities like $\mathbf{E}$ and $\mathbf{J}$. Therefore, introducing (3.8) in (3.7) yields the final differential equation to be solved inside biological media:

$$\nabla \cdot (\bar{\bar{\sigma}} \nabla V) = \nabla \cdot \mathbf{J}_S. \tag{3.9}$$

No role for permittivity and permeability

In the classical electromagnetic theory, the two electric vectors $\mathbf{E}$, $\mathbf{D}$ and the two magnetic vectors $\mathbf{B}$, $\mathbf{H}$ are connected through the constitutive relationships

$$\mathbf{D} = \bar{\bar{\varepsilon}} \cdot \mathbf{E} \tag{3.10a}$$

$$\mathbf{B} = \bar{\bar{\mu}} \cdot \mathbf{H} \tag{3.10b}$$

where $\bar{\bar{\varepsilon}}$ and $\bar{\bar{\mu}}$ are respectively the electric permittivity and the magnetic permeability of the medium. These relations remain valid for biological tissues but are irrelevant in the frame of the static approximation and of the conductive electrolyte model.
Under these assumptions, it is the conductivity $\bar{\bar{\sigma}}$ which solely determines the values of $\mathbf{J}$ and $\mathbf{E}$ in a biological medium. This is equivalent to say that the capacitive $\bar{\bar{\varepsilon}}$ and inductive $\bar{\bar{\mu}}$ effects can be neglected regarding the conductive effects $\bar{\bar{\sigma}}$.

The quasistatic approximation: magnetic phenomena

Any current density flowing inside a material medium will create a magnetic field. Using the approximate static Maxwell equations (3.4), this magnetic field can be computed from

$$\nabla \times \mathbf{H} = \mathbf{J}. \tag{3.11}$$

In many current technological applications, $\mathbf{J}$ will be an alternating low frequency current $\mathbf{J} = \mathbf{J}_0 \cos(\omega t)$. The so-called "quasi static" approximation assumes that (3.11) remains valid for these low frequency currents and hence

$$\nabla \times \mathbf{H}(t) \simeq \mathbf{J}(t). \tag{3.12}$$

Now, this slow-varying magnetic field could be used to compute a first correction to the static electric field by invoking the basic Maxwell equation (3.1b) and the constitutive relations (3.10).

3.1.2 Boundary conditions

At the interface

The general bioelectric problem is formed of tissues of different electrical conductivities, which are usually discrete, therefore the domain is piecewise homogeneous as shown in Fig. 3.1. The problem

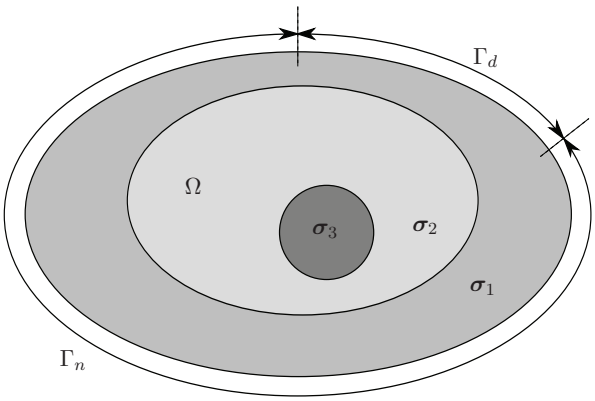

Figure 3.1: General bioelectric problem. The medium Ω is divided in three subregions σ_i having their own electrical properties. The external boundary Γ is divided in two. On one part, Γ_d, a Dirichlet boundary condition is applied (fixed potential). On the other, Γ_n, a Neumann boundary condition is applied (fixed normal current).

can be solved for each region having a constant $\bar{\bar{\sigma}}$ with the help of (3.9) and then enforcing continuity at the interface between regions.
Electromagnetic theory requires that on one side the potential is continuous (to avoid non physical infinite fields which would be associated to discontinuous potentials) and that the normal component of the current density is also continuous (to avoid charge accumulation at the interface which will violate the physical principle of charge conservation). This yields the following mathematical relationships, known as boundary conditions :

$$V_i = V_j \tag{3.13a}$$

$$\hat{n} \cdot \bar{\bar{\sigma}}_i \nabla V_i = \hat{n} \cdot \bar{\bar{\sigma}}_j \nabla V_j. \tag{3.13b}$$

Heres i and j are two adjacent regions. $\bar{\bar{\sigma}}$ is a conductivity tensor. $\hat{n}$ denotes the unit outward vector orthogonal to the interface. V_i and V_j are the potentials on the two sides of the interface.

On the electrode surface

Special boundary conditions must be applied on the interface between the biological tissue and an electrode, either on the voltage or on the current flowing through this interface. A fixed potential is denoted as a **Dirichlet** boundary condition

$$V(x, y, z) = V_0 \tag{3.14}$$

where V_0 is the fixed electrode voltage. A fixed current is denoted as a **Neumann** boundary condition

$$\hat{n} \cdot \bar{\bar{\sigma}} \nabla V = J_n \tag{3.15}$$

where J_n is the surface current density of the electrode.

On the outer boundary

The problem studied in this thesis is a bounded conducting volume (human body), and the conductivity outside the volume is zero. Therefore, at the interface between air and human tissues the outward

normal current J_n is zero and the Neumann boundary condition reduces to

$$\hat{n} \cdot \bar{\bar{\sigma}} \nabla V = J_n = 0. \tag{3.16}$$

This Neumann boundary condition models our problem much more accurately than the Dirichlet condition used in previous studies, roughly equivalent to assure a null potential (ground) in the outer boundary.

The final algorithmic strategy used in this thesis is summarized in Fig. 3.2. The next section will show how the general bioelectric problem described here can be built and solved when applied to the head.

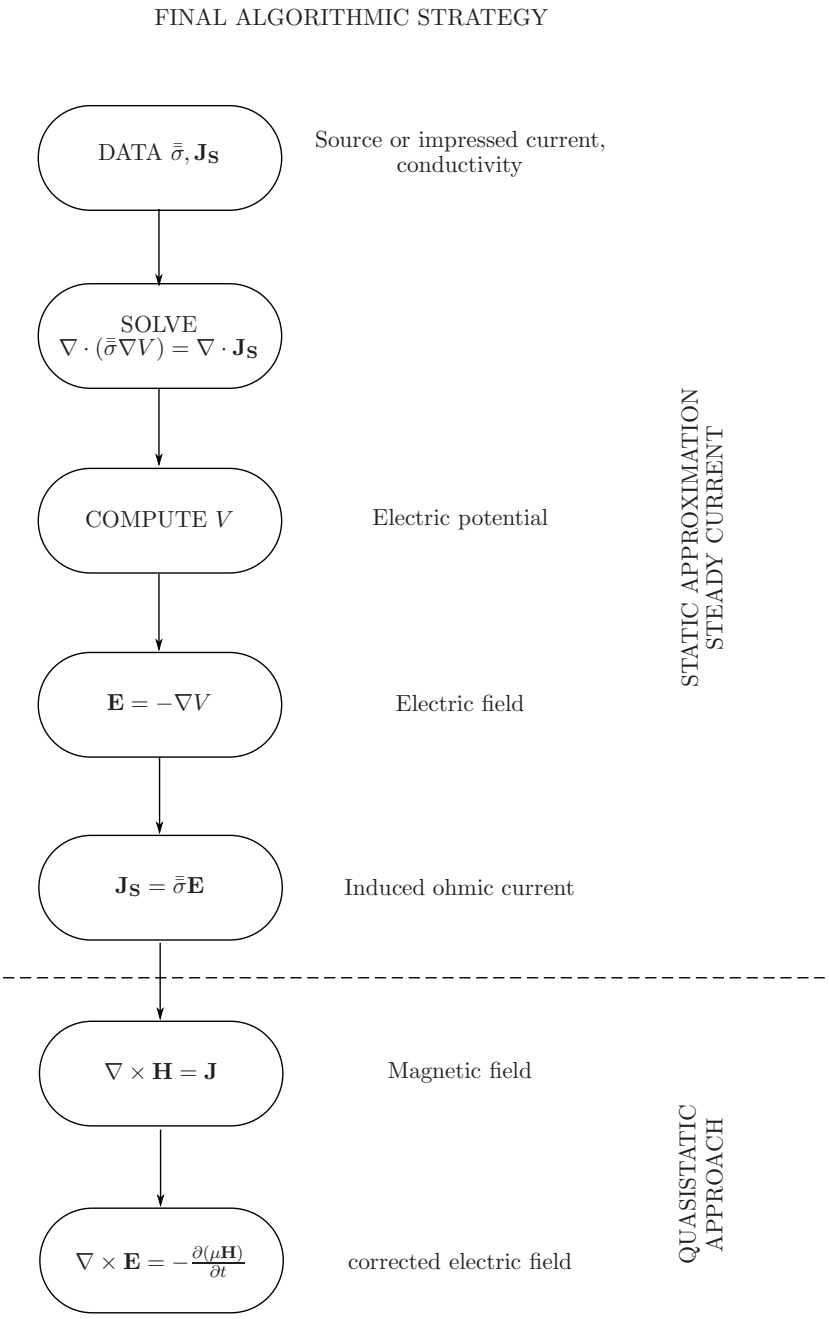

Figure 3.2: Final algorithmic strategy.

3.2 Bioelectromagnetic head models and associated electromagnetic analysis methods

The main challenge in head modelling is to model the head tissues adequately (both shape and characteristics). Human head is made of several type of tissues (such as skin, bone, white and gray matter, cerebrospinal fluid (CSF)...). All these tissues have different structures and composition and therefore different electrical characteristics. For example, bone can be seen as an insulator, CSF as a good conductor.
Bioelectromagnetic models of the head can be used either to evaluate the electroencephalograms (EEG) generated from a known source (forward or direct problem), or to estimate the source position of a known EEG (backward or inverse problem).
In this section, a review of the bioelectric models and their associated electromagnetic analysis methods is proposed. A summary is given in Table 3.1.

Table 3.1: Model used for bioelectric problem.

Bioelectric model		EM model	+	-
Ideal	spherical and ellipsoidal	analytical	fast	not realistic geometry
Anatomical	realistic shaped layered model	boundary element method	fast	important mathematical preprocessing
	atlas based anatomical model	FE method	limited number of unknowns	statistical models
	patient based model	FE method + finite difference method	realistic	high number of unknowns, image preprocessing needed

3.2.1 Ideal models: spherical and ellipsoidal shapes

The head models are becoming more and more realistic thanks to:

- the increase of the computational power which reduces the time of calculation and allows an increase of the problem size
- the improvement of the medical imaging, which provided better and more detailed knowledge of tissues properties.

The first models describing the bioelectric phenomena in the head were used to predict EEG. The head was approximated by concentric spheres or ellipsoids of different tissues [3, 4]. Typically, three classes of tissues were used in these models: brain, skull and scalp from the innermost to the external layer (see Fig. 3.3).
These models can be solved analytically and provide a first reasonable approximation.
More realistic models have been developed later, increasing the number of layers and using anisotropic conductivity [5]. These models have been employed to localize the electrophysiological generators associated with neural activity in various states of health and disease.

3.2.2 Anatomical models

To overcome the geometrical simplification of using spheres to model the head, models having more realistic shapes have been built. But these models imply the use of numerical techniques to solve the problem as no analytical solution exists for these complex geometries. Each domain has therefore to

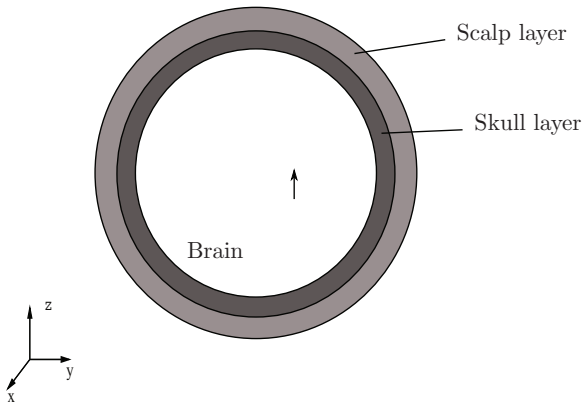

Figure 3.3: Three layers head model, the arrow represents a dipole source.

be sampled into elements. Each element has to be defined to be as close as possible to reality (shape and physical properties).

3.2.3 Atlas based models

The first realistic model geometries are based on anatomical knowledge [4, 6]. These models are segmented according to anatomical atlases. The geometry used is thus based on statistical observations made during post mortem dissection. These observations allow to divide the structure of the human brain in several tissue classes. Fig. 3.4 illustrates an example of an atlas-based FE model.

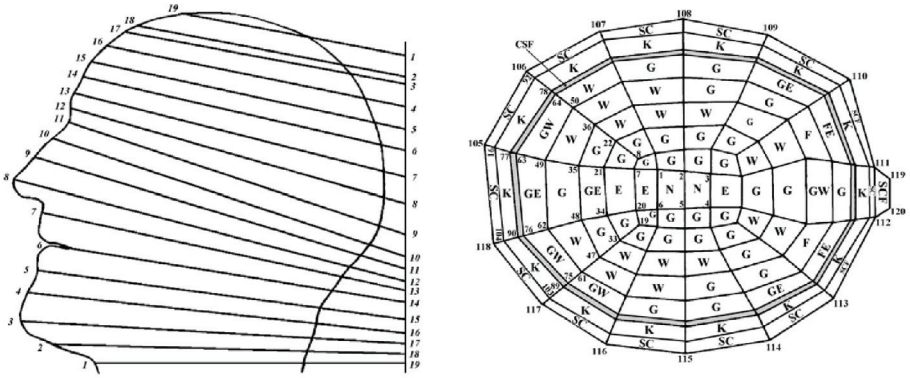

Figure 3.4: Finite element model of a human head based on the atlas of Eycleshymre and Shoemaker (1911) [7]. Classes of tissue are muscle (M), fat (F), pharynx (P), bone (B), skull (K), gray matter (G), white matter (W), cerebellum (C), medulla spinalis (N), CSF (E), blood (BL), air cavity (KL), and scalp (SC), taken from [8].

Once the model built, the electrical properties of each tissue class used in the model must be characterized. Several studies have been made to characterize the electrical properties of biological tis-

sues [9–11]. In general, quite large discrepancies have been obtained when quantifying these properties. A review of these studies can be found in the article of Geddes and Baker [12].

3.2.4 Medical imaging based models

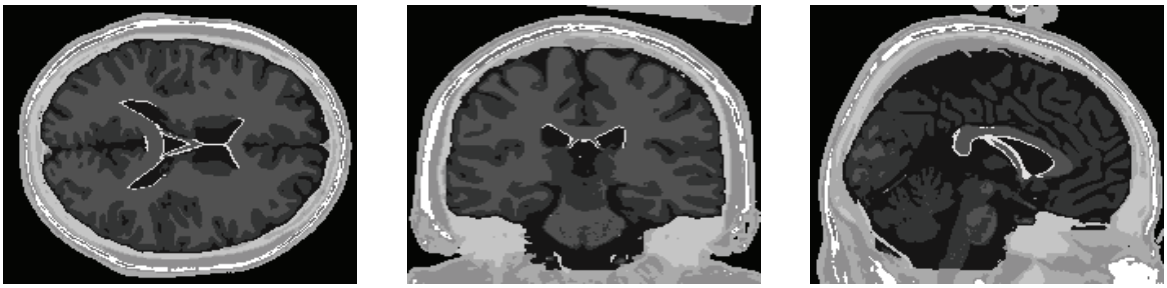

(a) Axial cut (b) Coronal cut (c) Sagittal cut

Figure 3.5: Cutting views of a segmented head. Each pixel has a color which refers to the class of tissue it belongs to (for example here from black to white one has CSF, gray matter, white matter, fat, muscle, skin, skull, glial matter). Based on the BrainWeb model [13].

With the improvement of the medical imaging techniques (for instance magnetic resonance imaging (MRI) or computed tomography (CT)), the knowledge on the head tissues distribution dramatically increased.
Consequently, head models using this information also increased strongly in complexity. Nowadays, these models can be based on an individual patient's head, according to some image preprocessing to transform the obtained biological data in electrical quantities.

As each imaging technique has its own advantages, image processing is needed to combine these advantages, thus increasing the reality of the final model as explained hereafter.
T1-weighted MRI is well suited for segmentation of tissue boundaries like white and gray matter, outer skull and skin. But the identification of the inner skull surface is problematic.
CT is well suited for imaging bone tissues as the human skull. But most of the models built for neurology or neuropsychology research are based on healthy patient, therefore exposition to ionized radiation is inappropriate.
The use of proton density MRI (PD-MRI) coupled to T1-MRI to build a head model is well explained in Wolter's PhD dissertation [14]. The PD-MRI is registered onto the corresponding image in order to correct for movement of the subject and geometrical distortions.

Afterwards, segmentation algorithms are applied to obtain for each voxel a probability of belonging to a class of tissue. Then each element is labelled according to the tissue having obtained the highest probability (see Fig. 3.5). Finally, bulk isotropic conductivities values are taken from literature and assigned to each element according to its label.

Lately an improvement of magnetic resonance imaging technique has provided information on the water diffusion in tissues. This information provided by the diffusion tensor MRI (DT-MRI) [15] can be used to enforce the reality of the head model, as explained in the next section.

3.3 Diffusion and conductivity tensors

Previous modelling studies using anatomical models have shown that the results of the forward problem are sensitive to the accuracy of the conductivity values assumed for the tissue [16–19]. So in this thesis a special care will be taken to model these tissues and especially the ones surrounding the electrode.
Anatomical models have the ability to be based on real patient heads, but the segmentation process assume that each tissue of a class share the same electrical properties. However this assumption may be questioned, as a voxel is likely to be composed of more than one type of tissue.

Efforts to develop an imaging strategy to characterize noninvasively the electrical conductivity of tissue have been encumbered by anatomical and biophysical barriers. The organ of interest can be shielded by highly resistive barriers such as the bony tissue of the skull. The tissue can exhibit significant reactance, anisotropy and microstructural heterogeneity.
The difficulties associated with imaging biological conductivity *in vivo* can be appreciated by considering the limitations of electrical impedance tomography. This technique suffers from poor spatial resolution and requires delivering current to the tissues under characterization.

Lately, the improvement of medical imaging technique has provided the diffusion tensor MRI (DT-MRI) [15]. As explained in Section 2.1.4, this imaging technique provides information on the water self-diffusion in tissue for each voxel. The use of the information given by the DT-MRI has been made in several studies to show the importance of the anisotropy on the solution obtained for EEG prediction in forward or backward models [14, 20, 21].

This section explains how the electrical conductivity of the tissues used in our model is obtained from the results of the DT-MRI.

3.3.1 Water diffusion tensors

The DT-MRI provides images of diffusion gradient applied in noncolinear directions. An example of a 32 direction DT-MRI result is shown in Fig. 3.6.

An image processing task is needed to obtain a more useful information: the diffusion tensor. This image processing uses multiple linear regressions as explained in [22]. A diffusion tensor $\bar{\bar{d}}$ is then obtained for each voxel. It provides a three dimensional indicator on the ability of water molecules to move. As these movements are constrained by the structure of the cells, it provides information on the fibers directions. $\bar{\bar{d}}$ is a 3×3 matrix which is symmetric, full rank.
If we define a local Cartesian basis with the axis along the eigenvectors, the tensor can be represented by a diagonal matrix. Therefore it can be represented as an ellipsoid and can be written as

$$\bar{\bar{d}} = \mathbf{S} \begin{bmatrix} d_1 & 0 & 0 \\ 0 & d_2 & 0 \\ 0 & 0 & d_3 \end{bmatrix} \cdot \mathbf{S}^t \tag{3.17}$$

where d_1, d_2 and d_3 are the diffusion eigenvalues and $\mathbf{S}$ is the rotation matrix composed by putting the eigenvectors in the columns.

The obtained tensor is hardl to represent visually. That is why several scalar indicators are used to characterize the diffusion tensor.

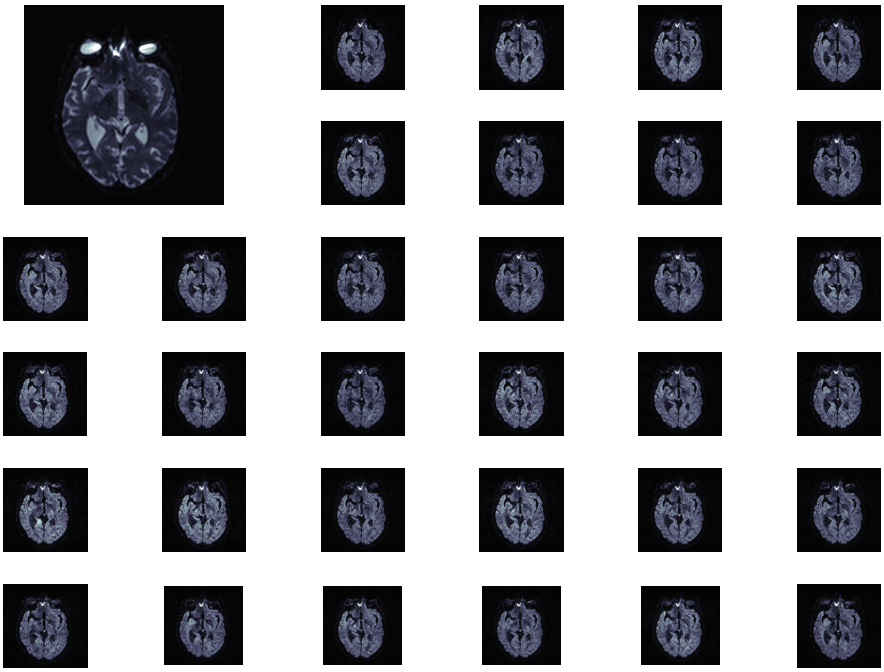

Figure 3.6: Images obtained from a 32 axes DT-MRI. The first image is a T1 MRI. Each small image shows the diffusion gradient obtained in one of the 32 noncolinear directions.

Trace of the diffusion tensors

The mean diffusivity is obtained by taking the trace of the diffusion tensor:

$$Tr(\bar{\bar{d}}) = d_1 + d_2 + d_3. \tag{3.18}$$

This quantity gives an information on the overall diffusion for each voxel. Note that no information on the anisotropy can be extracted at this point. Nevertheless, it can be observed that the tissue consistently showing the highest diffusion is the cerebrospinal fluid (CSF). For this reason, CSF plays an essential role as reference or normalizing value in the conductivity calculation formula of the conductivity tensor.

Anisotropy of the diffusion tensors

To have information on the tensor's anisotropy, the fractional anisotropy (FA) and the volume ratio (VR) have been defined as [22] :

$$FA(\bar{\bar{d}}) = \sqrt{\frac{3}{2}}\sqrt{\frac{(d_1 - \langle d\rangle)^2 + (d_2 - \langle d\rangle)^2 + (d_3 - \langle d\rangle)^2}{d_1^2 + d_2^2 + d_3^2}} \tag{3.19}$$

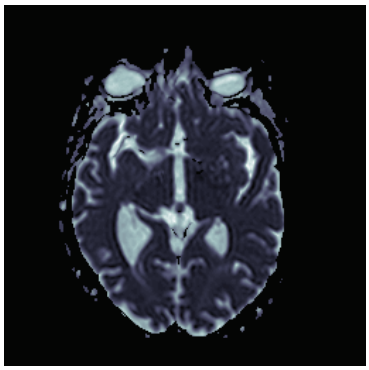

Figure 3.7: Trace of the diffusion tensor. Due to its similarity with water solution, tensors issued from CSF shows the biggest trace. As the ventricles are filled with that liquid, they are easily seen on the picture. The limit between gray and white matter is hardly visible.

where $\langle d \rangle$ is the mean eigenvalue.
FA quantifies the fraction of the "magnitude" of $\bar{\bar{d}}$ that can be ascribed to anisotropic diffusion and varies between 0 (isotropic diffusion) and 1 (infinite anisotropy).

$$VR(\bar{\bar{d}}) = \frac{d_1 d_2 d_3}{\langle d \rangle^3}. \tag{3.20}$$

VR represents the ratio of the ellipsoid volume to the volume of a sphere of radius $\langle d \rangle$, its range is from 1 (isotropic diffusion) to 0, hence, it is is preferred to use the quantity $1 - VR$ in order to continue to assign the value 0 to isotropy.
An illustration of these three indicators can be seen in Fig. 3.8.

Three dimensional representation of the diffusion tensors

Another way to represent the diffusion tensor is to use ellipsoids, as proposed in [15]. An ellipsoid is a three-dimensional representation of the diffusion distance covered in space by molecules in a given diffusion time (see Fig. 3.9). Each ellipsoid has as main axes the eigenvectors of the diffusion tensor.

3.3.2 Conductivity tensors

The information provided by the DT-MRI, namely the water diffusion tensors, characterizes the diffusive motion of protons and other metabolites within a single voxel of anisotropic medium. Basser *et al.* [15] were the first to propose that the diffusion tensor and conductivity tensor might share eigenvectors. This observation was prompted by the observation that, although in free solutions there is no fundamental relationship between the two transport modes, in a structured medium such as biological tissues, the two processes are related through the boundary conditions imposed by the tissue geometry.

In their study Tuch *et al.* [23] showed that a strong linear relationship between the conductivity and

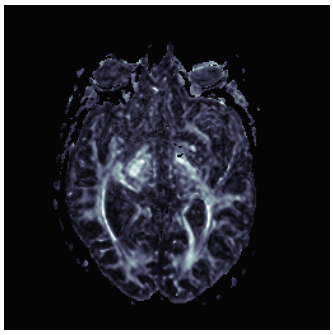

(a) Fractional anisotropy of the diffusion tensor

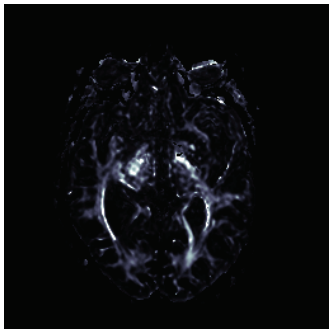

(b) Volume ratio of the diffusion tensor

Figure 3.8: Indicators measuring the anisotropy obtained from the DT-MRI. As the white matter is made of bundle of nerves sharing the same direction, it has a high anisotropy and therefore can be easily seen on these picture. Gray matter is made of fibers crossing in random directions, so the anisotropy is low. Opposite to white matter, the CSF shows a very low anisotropy as it is close to a water solution. The ventricles observed easily in Fig. 3.7 are now close to 0.

diffusion tensor exists. This relationship can be written as

$$\bar{\bar{\sigma}}_i = \frac{\sigma_e}{d_e}\bar{\bar{d}}_i, \tag{3.21}$$

where $\bar{\bar{\sigma}}_i$ and $\bar{\bar{d}}_i$ are the conductivity and diffusion tensor (respectively), and σ_e and d_e denote the extracellular conductivity and diffusivity. This linear approximation of the relationship between the eigenvalues of the conductivity tensor and the diffusion tensor assumes the intracellular conductivity to be negligible.

Several techniques can be used to include the anisotropic conductivity into electrical models of the head.
A fixed ratio between the conductivity along the longitudinal eigenvector and the transverse eigenvectors (σ_L and σ_T, respectively) can be set. This ratio has been evaluated to be 9:1 by Nicholson [24]. This means that the conductivity along a nerve bundle is nine times bigger than the transverse or perpendicular one. A constraint is then used to fix the volume of the ellipsoid having these eigenvectors. The volume is compared to the volume obtained for an ellipsoid having its eigenvectors σ_{iso} equal (isotropic sphere) of the same class of tissue. The two main constraints used are:

- Wang's constraint [25], which states that the product of radial and tangential conductivity has to stay constant and has to be equal to the square of the isotropic conductivity:

$$\sigma_L \sigma_T = {\sigma_{\text{iso}}}^2, \tag{3.22}$$

- a volume constraint [14, 21] which retains the geometric mean of the eigenvalues and thus the

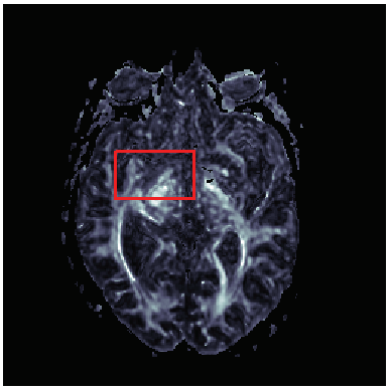

(a) Cutting view of the volume ratio of full head.

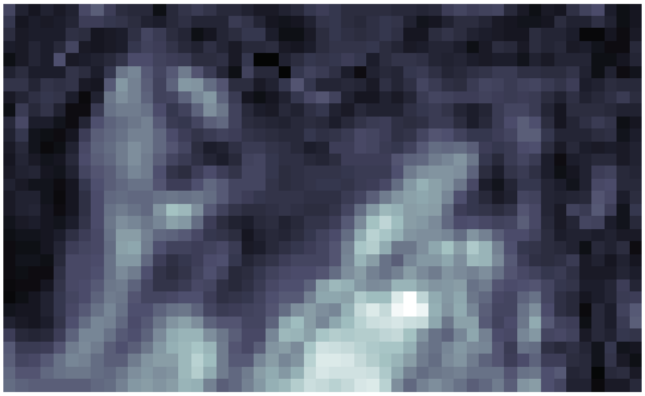

(b) Cutting view of the volume ratio of partial head cut.

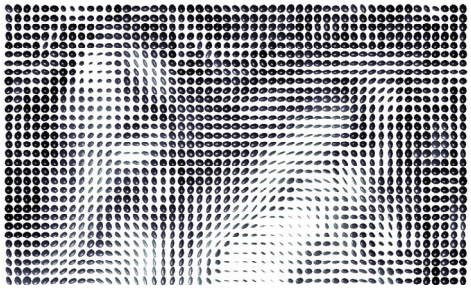

(c) Cutting view of the diffusion tensor ellipsoids.

Figure 3.9: The ellipsoids represented in (c) show the diffusion tensor obtained from a DT-MRI file. Their color is linked to their volume ratio (see equation (3.20)). In order to have a better visualization, each ellipsoid has its main eigenvalue equalized. The white matter, showing high anisotropy, can easily be seen in white on the image (b) and its derived tensors ellipsoids show a prolate aspect on image (c).

volume of the conductivity tensor:

$$\frac{4}{3}\pi\sigma_L(\sigma_T)^2 = \frac{4}{3}\pi{\sigma_{\text{iso}}}^3. \tag{3.23}$$

Another technique is to use the volume constraint directly on the obtained diffusion tensor and the linearity factor between the diffusion and the conductivity tensor (see equation 3.21) [26]

$$\frac{d_1}{\sigma_1} = \frac{d_2}{\sigma_2} = \frac{d_3}{\sigma_3} \tag{3.24}$$

where d_1, d_2 and d_3 are the eigenvalues of the matrix representation of the diffusion tensor at a voxel

as explained in equation 3.17. σ_1, σ_2 and σ_3 are the unknown eigenvalues of the matrix representation of the conductivity tensor at the same voxel. This system of two equations and three unknowns can be solved by applying the volume constraint on the anisotropic conductivity ellipsoid using the isotropic conductivity sphere of the tissue considered:

$$\frac{4}{3}\pi\sigma_1\sigma_2\sigma_3 = \frac{4}{3}\pi{\sigma_{iso}}^3. \tag{3.25}$$

These techniques are well tailored to model either the white matter or the skull anisotropy. Nevertheless, they have to follow a segmentation procedure, since the application of either the volume constraint or Wang's constraint is using a reference volume of a certain class of tissue. But, as shown in Fig. 3.8, the anisotropy is not constant in a class of tissue. The assumption of a fixed ratio of anisotropy can be challenged, since when bundles of fibers are crossing in a voxel, the diffusion tensor can show two main directions or be quasi anisotropic. Setting a constant volume among a class of tissue can also be questioned, since a voxel can contain several type of tissues and therefore can show an overall conductivity higher than other voxel of the same class of tissue.

3.3.3 Original approach to obtain the conductivity tensors

The usual approach to include the anisotropic conductivity in patient tailored FE models of the head is the following. A pre processing treatment of the medical imaging obtained for the patient is made to segment the different classes of tissues. To the isotropic classes of tissues such as CSF or gray matter, an isotropic conductivity tensor is applied, constant for each tissue class and based on the isotropic conductivity values found in litterature. For the classes of tissue showing anisotropy, such as white matter or skull, the use of Wang's constraint or of volume constraint is made, based on the anisotropy direction provided by the DT-MRI [20, 21, 26].
In this thesis the segmentation of the tissues is avoided. A linear transformation of the water diffusion tensor into electrical conductivity tensors is applied on all the tensors obtained by the DTMRI, regardless of the tissue class they belong to. The linear relation of the diffusion tensor and the electric conductivity tensor introduced in [23] is used **not only on the white matter but on all the tissues of the head**. The diffusion tensors are transformed into conductivity tensor using the following formula:

$$\bar{\bar{\sigma}}_{\text{voxel}} = \bar{\bar{d}}_{\text{voxel}} \cdot \left(\frac{\text{Vol}(\bar{\bar{\sigma}}_{CSF_{\text{iso}}})}{\text{Vol}(\bar{\bar{d}})_{max}} \right)^{1/3} \tag{3.26}$$

where Vol() refers the volume of an ellipsoid. The volumes of the diffusion tensor are normalized to fix the volume of the biggest diffusion tensor ellipsoid to be equal to an isotropic sphere of the tissue having the highest conductivity, namely the CSF. A head cut of the ellipsoids obtained with this method can be seen in Fig. 3.10. Formula (3.26) summarizes the new technique used in this work to predict conductivity values out of the diffusion measured by DT-MRI techniques.
Our proposed approach is supposed first to account better for the actual strong anisotropy of brain tissues. On the other hand, it is free from segmentation procedures and it it hence it should provide conductivity values more stable respect to the choice of FE geometries and meshes.

3.4 Finite element formulation

In order to solve the generalized bioelectric problem formulated in Section 3.1, a numerical technique is used, since obviously no analytical solutions is possible. Several numeric techniques exist having their own advantages and drawbacks.

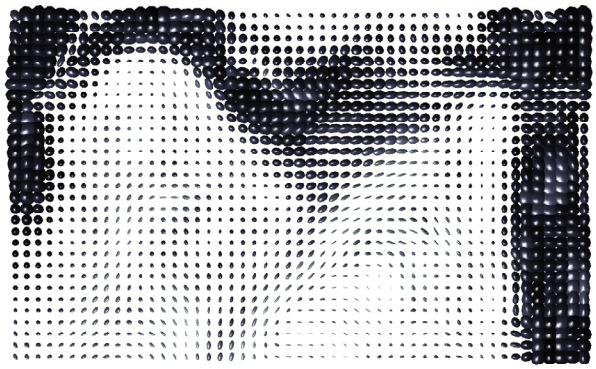

Figure 3.10: Conductivity tensor ellipsoids used in this thesis. The biggest tensor volume is normalized to the volume of an isotropic sphere of CSF. Ellipsoids representing the CSF can be identified as they are quasi spherical and have big volumes. As white matter is highly anisotropic and has a lower conductivity than CSF, the ellipsoids are hardly seen.

The boundary element method (BEM) has been widely used for head modelling and for EEG source localization [27–30]. The use of BEM is adapted for piecewise homogeneous isotropic compartments. The main layers (scalp, skull and brain) can be represented with realistic geometry and the currents are computed only on the boundaries, therefore the computational cost remains low. But BEM involves an important analytic effort before computation.
Another technique used to solve the bioelectric problem is the finite difference method (FDM) [5, 26, 31–33]. This numerical technique as an algorithm easily implementable and is able to treat any geometry and anisotropic and inhomogeneous media. Nevertheless, it has to use a regular mesh and any interface must be interpolated as a staircase slope. Therefore it needs an important computational effort to deal with a high definition model of the head.
The finite element (FE) method is a numerical technique that uses the same kind of discretization as FDM, howevre the use of regular meshes is not mandatory. The number of unknowns and the computational power to solve big problems can be therefore greatly reduced, while keeping, thanks to an adaptive meshing, a high definition mesh on specific areas.

For the problem treated in this thesis, the model should provide the evaluation of the potentials delivered by the DBS electrode, and especially on the tissues surrounding the electrode contact as they are most likely to be influenced by the simulation. These tissues are highly inhomogeneous and anisotropic. Considering the size of the problem, which extends to the upper chest in order to include all the element involved in deep brain stimulation, the use of mesh refinement on specific area is clearly an advantage. Therefore the modelling technique that will be used is the finite element method [34,35]. In the following a description of this method is given, using linear shape functions. The construction of the stiffness matrix is explained, leading to a matrix linear system that can be solved with a matrix inversion.
Another important distinction is that FDM works on a three dimensional grid of equidistant points.

Potentials and fields outside the grid must be obtained by external specific interpolation. On the other hand, FE method works with tetrahedrons where the unknown quantities are assumed to follow simple mathematical variations. Therefore FE method works on a continuous space and no external interpolation is needed.

3.4.1 Finite element formulation of the bioelectric problem

Finite element formulations involve the approximation of an unknown function, the state variable, over some region of space Ω (see Fig. 3.1). This state variable $V(x, y, z)$ is a function of spatial coordinates. The finite element method provides an approximate solution satisfying the governing equations and boundary conditions.

The first step of finite element formulation is the construction of an approximate solution satisfying the governing equation of our problem.

The electrical potential V, the state variable of our problem is governed by equation (3.9), repeated here:

$$\nabla \cdot (\boldsymbol{\sigma} \nabla V) = \nabla \cdot \mathbf{J}_s.$$

Let $\tilde{V}$ designate this approximation and let

$$V \approx \tilde{V} = \sum_{i=1}^{n} V_i N_i, \tag{3.27}$$

where V_i is the solution of the electric potential at the node i and N_i is any piecewise-smooth function (called basis or shape function) spanning an n-dimensional linear space.

As (3.27) is unlikely to exactly satisfy the governing equation, substituting it in the governing differential equation (3.9) leads to an error or residual

$$R = \nabla \cdot (\sigma \nabla \widetilde{\mathbf{V}}) - \nabla \cdot \mathbf{J_s} \neq \mathbf{0}. \tag{3.28}$$

Obviously, the residual will not equal zero unless our approximate solution $\tilde{V}$ is the one. A criterion has to be chosen to optimize $\tilde{V}$. The Galerkin method of weighted residuals is forcing the residual to equal zero in an average sense, using for weighting functions the set of shape functions

$$\int_{\Omega} N_j R \, \mathrm{d}\Omega = 0, \quad j = 1, \ldots, n. \tag{3.29}$$

Substituting (3.28) in (3.29) and applying Gauss' theorem

$$\int_{\Omega} \nabla f g \, \mathrm{d}\Omega = \int_{\Gamma = \partial\Omega} f g \hat{n} \, \mathrm{d}\Gamma - \int_{\Omega} f \nabla g \, \mathrm{d}\Omega, \tag{3.30}$$

with $g = N_j$ and $f = \boldsymbol{\sigma} \nabla \widetilde{V}$ gives

$$-\int_{\Omega} \nabla N_j \boldsymbol{\sigma} \nabla \widetilde{V} \, \mathrm{d}\Omega + \underbrace{\int_{\Gamma} N_j (\boldsymbol{\sigma} \nabla \widetilde{V}) \cdot \hat{n} \, \mathrm{d}\Gamma}_{B.C.} = \int_{\Omega} \nabla \cdot \mathbf{J}_s N_j \, \mathrm{d}\Omega, \quad j = 1, \ldots, n, \tag{3.31}$$

where

$$B.C. = \int_{\Gamma} N_j(\boldsymbol{\sigma}\nabla\widetilde{V}) \cdot \hat{n}\,\mathrm{d}\Gamma = \int_{\Gamma} N_j \mathbf{J} \cdot \hat{n}\,\mathrm{d}\Gamma = \int_{\Gamma} J_n N_j\,\mathrm{d}\Gamma, \tag{3.32}$$

J_n being the normal component of the current at the boundary where Neumann boundary conditions are imposed.

Using the definition of $\widetilde{V}$ from (3.27) and letting all known values to be on the right-hand side of equation (3.31) yields

$$\sum_{i=1}^{n} V_i \int_{\Omega} \nabla N_j \boldsymbol{\sigma} \nabla N_i\,\mathrm{d}\Omega = \int_{\Gamma} J_n N_j\,\mathrm{d}\Gamma - \int_{\Omega} \nabla \cdot \mathbf{J}_s N_j\,\mathrm{d}\Omega, \quad j = 1, \ldots, n, \tag{3.33}$$

which can be written in a matrix form

$$\mathbf{K}\mathbf{x} = \mathbf{f}. \tag{3.34}$$

In classical FEM approaches, $\mathbf{K}$ is called the stiffness matrix and $\mathbf{f}$ is the excitation vector. The elements of the stiffness matrix $\mathbf{K}$ depend only on the shape functions and conductivity and are given by

$$k_{ji} = \int_{\Omega} \boldsymbol{\nabla} N_j \boldsymbol{\sigma} \boldsymbol{\nabla} N_i\,\mathrm{d}\Omega. \tag{3.35}$$

The force or excitation vector $\mathbf{f}$ contains the source function and boundary conditions and is given by

$$f_j = \int_{\Gamma} J_n N_j\,\mathrm{d}\Gamma - \int_{\Omega} \boldsymbol{\nabla} \cdot \mathbf{J}_s N_j\,\mathrm{d}\Omega, \tag{3.36}$$

and the vector $\mathbf{x}$ contains the solutions of the unknown potentials at n nodes $x_i = V_i$.

As the shape functions have only local support, the matrix $\mathbf{K}$ is sparse.

3.4.2 Shape function definition

The shape functions are chosen such that $N_i(x_j, y_j, z_j) = \delta_{ij}$, where (x_i, y_j, z_j) are the coordinates of node j. In other words, the function has a value of one at its associated node and zero at all other nodes. The domain under study is partitioned into elements with adjacent sides and no overlap or gap between elements. The elements are connected at nodes, which must be in the corner of each element but may also be on the edges or in the center. The numbers of nodes per element determines the order of the shape function polynomials. Whereas the domain considered is inhomogeneous, each element needs to be homogeneous. In this section, the definition of linear basis function is given for tetrahedron element type (basis functions can be quadratic or even with higher order of continuity).

Fig. 3.11 shows the mapping between a four-node tetrahedral daughter element in the (x, y, z) space and the unit parent element in the (ξ, η, ζ) space. We will first define the shape functions in the parent (ξ, η, ζ) space and then map them to the (x, y, z) space.

Any point in the daughter tetrahedron (x, y, z) has a mapping point (ξ, η, ζ) in parent unit tetrahe-

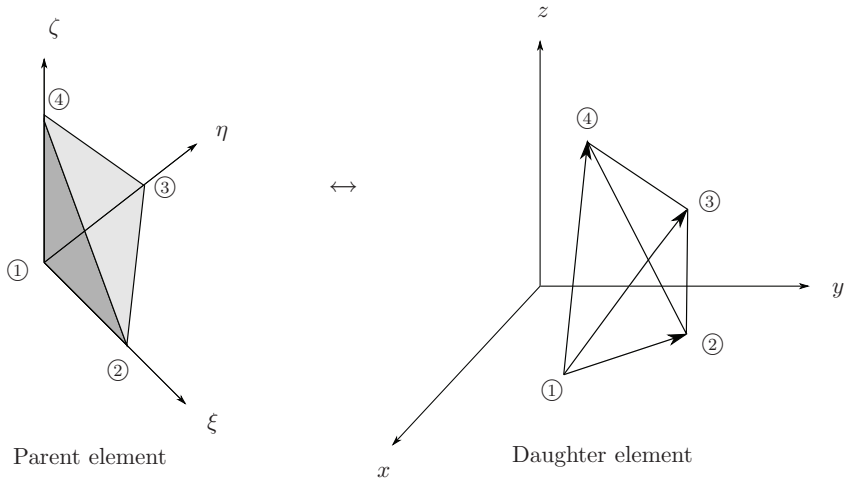

Figure 3.11: Mapping between a four-node tetrahedral daughter element in the (x, y, z) space and the unit parent element in (ξ, η, ζ) space.

dron and the following relation holds

$$\begin{aligned}\begin{pmatrix} x \\ y \\ z \end{pmatrix} &= \begin{pmatrix} x_1 \\ y_1 \\ z_1 \end{pmatrix} + \xi \begin{pmatrix} x_2 - x_1 \\ y_2 - y_1 \\ z_2 - z_1 \end{pmatrix} + \eta \begin{pmatrix} x_3 - x_1 \\ y_3 - y_1 \\ z_3 - z_1 \end{pmatrix} + \zeta \begin{pmatrix} x_4 - x_1 \\ y_4 - y_1 \\ z_4 - z_1 \end{pmatrix} \\ &= (1 - \xi - \eta - \zeta) \begin{pmatrix} x_1 \\ y_1 \\ z_1 \end{pmatrix} + \xi \begin{pmatrix} x_2 \\ y_2 \\ z_2 \end{pmatrix} + \eta \begin{pmatrix} x_3 \\ y_3 \\ z_3 \end{pmatrix} + \zeta \begin{pmatrix} x_4 \\ y_4 \\ z_4 \end{pmatrix}. \end{aligned} \tag{3.37}$$

The natural coordinates for tetrahedrons are based on volume ratios. The volume of a tetrahedron, when coordinates of all four nodes are known, is given by

$$\Omega = \frac{1}{6} \begin{vmatrix} 1 & x_1 & y_1 & z_1 \\ 1 & x_2 & y_2 & z_2 \\ 1 & x_3 & y_3 & z_3 \\ 1 & x_4 & y_4 & z_4 \end{vmatrix}. \tag{3.38}$$

Consider first the ratio of the volume formed by points ②, ③, ④ and any point (ξ, η, ζ) inside of the parent tetrahedron and the volume of the unit tetrahedron. The volume of the unit tetrahedron is $1/6$, so this ratio is given by

$$N_1(\xi, \eta, \zeta) = \begin{vmatrix} 1 & \xi & \eta & \zeta \\ 1 & 1 & 0 & 0 \\ 1 & 0 & 1 & 0 \\ 1 & 0 & 0 & 1 \end{vmatrix} = 1 - \xi - \eta - \zeta. \tag{3.39}$$

This is at the same time the expression for the shape (basis) function for the node ①. Its value varies linearly from $N_1 = 1$ at node ① to $N_1 = 0$ at all other nodes.

In the same way we define the linear shape function for node ②. It is defined as ratio of the volume formed by points ①, ③, ④ and any point (ξ, η, ζ) and the volume of the unit tetrahedron, and it is

given by

$$N_2(\xi,\eta,\zeta) = \begin{vmatrix} 1 & \xi & \eta & \zeta \\ 1 & 0 & 0 & 0 \\ 1 & 0 & 1 & 0 \\ 1 & 0 & 0 & 1 \end{vmatrix} = \xi. \tag{3.40}$$

Similarly for the rest of the nodes

$$N_3(\xi,\eta,\zeta) = \eta, \tag{3.41}$$

$$N_4(\xi,\eta,\zeta) = \zeta. \tag{3.42}$$

If we take into account the definition of the basis functions and the mapping equation (3.37), the mapping between the parent and daughter tetrahedrons can be defined as a function of shape functions and node coordinates

$$x(\xi,\eta,\zeta) = \sum_{i=1}^{4} N_i(\xi,\eta,\zeta)x_i, \tag{3.43a}$$

$$y(\xi,\eta,\zeta) = \sum_{i=1}^{4} N_i(\xi,\eta,\zeta)y_i, \tag{3.43b}$$

$$z(\xi,\eta,\zeta) = \sum_{i=1}^{4} N_i(\xi,\eta,\zeta)z_i. \tag{3.43c}$$

Derivatives of shape functions

The stiffness matrix involves derivatives of the basis functions, which can be calculated using a chain rule for partial derivatives. The mapping from parent to daughter element is characterized by the Jacobian matrix, which in 3-D, for a parent (ξ,η,ζ) space is given by

$$[\mathcal{J}] = \begin{bmatrix} \frac{\partial x}{\partial \xi} & \frac{\partial y}{\partial \xi} & \frac{\partial z}{\partial \xi} \\ \frac{\partial x}{\partial \eta} & \frac{\partial y}{\partial \eta} & \frac{\partial z}{\partial \eta} \\ \frac{\partial x}{\partial \zeta} & \frac{\partial y}{\partial \zeta} & \frac{\partial z}{\partial \zeta} \end{bmatrix}. \tag{3.44}$$

The relationship between derivatives is given by

$$\begin{pmatrix} \frac{\partial N_i}{\partial \xi} \\ \frac{\partial N_i}{\partial \eta} \\ \frac{\partial N_i}{\partial \zeta} \end{pmatrix} = [\mathcal{J}] \begin{pmatrix} \frac{\partial N_i}{\partial x} \\ \frac{\partial N_i}{\partial y} \\ \frac{\partial N_i}{\partial z} \end{pmatrix}, \tag{3.45}$$

that is

$$\begin{pmatrix} \frac{\partial N_i}{\partial x} \\ \frac{\partial N_i}{\partial y} \\ \frac{\partial N_i}{\partial z} \end{pmatrix} = [\mathcal{J}]^{-1} \begin{pmatrix} \frac{\partial N_i}{\partial \xi} \\ \frac{\partial N_i}{\partial \eta} \\ \frac{\partial N_i}{\partial \zeta} \end{pmatrix}. \tag{3.46}$$

For the case of tetrahedral elements and linear basis functions, the derivatives are summarized in Table 1.

Now that all basis functions are defined and the derivatives in the parent cell known, and taking into account the definition of mapping as a function of basis functions and node coordinates, the expression

$i=$	1	2	3	4
$\frac{\partial N_i}{\partial \xi}$	-1	1	0	0
$\frac{\partial N_i}{\partial \eta}$	-1	0	1	0
$\frac{\partial N_i}{\partial \zeta}$	-1	0	0	1

Table 3.2: Derivatives of linear basis functions defined in parent tetrahedral element.

for the Jacobian matrix is given by

$$[\mathcal{J}] = \begin{bmatrix} x_2 - x_1 & y_2 - y_1 & z_2 - z_1 \\ x_3 - x_1 & y_3 - y_1 & z_3 - z_1 \\ x_4 - x_1 & y_4 - y_1 & z_4 - z_1 \end{bmatrix}. \tag{3.47}$$

The determinant of the Jacobian matrix will give us the value of the ratio between the volume of the daughter and parent elements.

3.4.3 Stiffness matrix calculation

Stiffness matrix elements are calculated for every node, which can have several basis functions assigned to. The number of basis functions assigned to the node depends on how many elements the node belongs to. The computation of stiffness matrix elements is on element-by-element basis. Non-zero interactions exist only between basis functions on a given element which is a support for them.

The interactions over a given element Ω_e are given by

$$k_{ij}^e = \int_{\Omega_e} \boldsymbol{\nabla} N_i \bar{\bar{\sigma}}_e \boldsymbol{\nabla} N_j \, \mathrm{d}\Omega. \tag{3.48}$$

Taking into account the conductivity tensor $\boldsymbol{\sigma}_e = [\sigma_{pq}]_{3\times 3}$, $p, q \in \{x, y, z\}$, (3.48) can be written in indicial notation as

$$k_{ij}^e = \sum_{p,q \in \{x,y,z\}} \int_{\Omega_e} \frac{\partial N_i}{\partial p} \sigma_{pq} \frac{\partial N_j}{\partial q} \, \mathrm{d}\Omega. \tag{3.49}$$

In the parent tetrahedron coordinate system (ξ, η, ζ), the interaction term (3.48) can be expressed as

$$k_{ij}^e = \int_{\Omega_e} (\boldsymbol{\nabla} N_i \bar{\bar{\sigma}}_e \boldsymbol{\nabla} N_j) \, |\mathcal{J}| \, \mathrm{d}\xi \, \mathrm{d}\eta \, \mathrm{d}\zeta, \tag{3.50}$$

where $|\mathcal{J}|$ is the determinant of the Jacobian of the transformation.

For a general type of basis functions we have to apply the numerical integration. If n_{int} - point integration rule is applied

$$\int_{\Omega} f(\xi, \eta, \zeta) \, \mathrm{d}\xi \, \mathrm{d}\eta \, \mathrm{d}\zeta = \sum_{k=1}^{n_{int}} w_k f(\xi_k, \eta_k, \zeta_k), \tag{3.51}$$

(3.50) becomes

$$k_{ij}^e = \sum_{k=1}^{n_{int}} w_k |\mathcal{J}| \left(\boldsymbol{\nabla} N_i \bar{\bar{\sigma}}_e \boldsymbol{\nabla} N_j\right)\big|_{(\xi_k,\eta_k,\zeta_k)}. \tag{3.52}$$

For the chosen tetrahedral elements and linear basis functions, the derivatives are constant for a given element and a given basis function. Supposing, in addition, that every element has an isotropic constant conductivity σ_e, (3.52) can be rewritten in the following simplified form

$$k_{ij}^e = \frac{\sigma^e}{6} |\mathcal{J}| \left(\frac{\partial N_i}{\partial x}\frac{\partial N_j}{\partial x} + \frac{\partial N_i}{\partial y}\frac{\partial N_j}{\partial y} + \frac{\partial N_i}{\partial z}\frac{\partial N_j}{\partial z} \right). \tag{3.53}$$

3.4.4 Force vector calculation

The force vector $\mathbf{f}$ is given by

$$f_i = \int_\Gamma J_n N_i \,\mathrm{d}\Gamma - \int_\Omega \boldsymbol{\nabla} \cdot \mathbf{J}_s N_i \,\mathrm{d}\Omega, \quad i = 1, \ldots, n, \tag{3.54}$$

and must be calculated on an element-by-element basis, that is, over its domain Ω_e and boundary Γ_e. Either V or J_n will be known at every node on the boundary Γ through boundary conditions. The value of V at node i is equivalent to x_i and if it is known then the equation for x_i can be eliminated from the vector of nodal potentials $\mathbf{x}$. If a fixed-voltage electrode is present, for example all nodes in contact with the electrode can be assigned that voltage and the associated equations eliminated from the solution.

The boundary integral

$$\int_\Gamma J_n N_i \,\mathrm{d}\Gamma \tag{3.55}$$

reduces to

$$J_n \int_{\Gamma_n} N_i \,\mathrm{d}\Gamma. \tag{3.56}$$

In the absence of external sources, this boundary integral will cancel between elements, since the current leaving one element boundary will exactly equal the current entering its neighbor as stated in equation (3.13b). It must be evaluated for the external boundary or any interval element boundaries if J_n exists due to an external source. If the source is a fixed-current electrode, for every node on the side to which the current electrode is connected we have

$$\int_\Gamma J_n N_i \,\mathrm{d}\Gamma = J_n \int_{\Gamma_n} N_i \,\mathrm{d}\Gamma. \tag{3.57}$$

If we introduce the mapping from daughter to parent variables (Fig. 3.12), the surface integral over a side of one element can be written as

$$\int_{\Gamma_e} N_i(x,y,z) \,\mathrm{d}\Gamma = \int_{\Gamma_{en}} N_i(x,y,z) |\mathcal{J}| \,\mathrm{d}\xi \,\mathrm{d}\eta, \tag{3.58}$$

where the Jacobian of transformation is equal to the ratio of the surface of the daughter side and the

surface of the unit triangle

$$[\mathcal{J}] = \begin{bmatrix} 1 & x_1 & y_1 \\ 1 & x_2 & y_2 \\ 1 & x_3 & y_3 \end{bmatrix}. \tag{3.59}$$

In the previous, we supposed that the daughter side is placed in the $x\,y$ plane. Taking into account the definitions of linear basis functions defined at nodes ①, ② and ③, one obtains

$$\int_{\Gamma_{en}} N_i(\xi, \eta, \zeta = 0)\,\mathrm{d}\xi\,\mathrm{d}\eta = \frac{1}{6}, \quad i = 1, 2, 3. \tag{3.60}$$

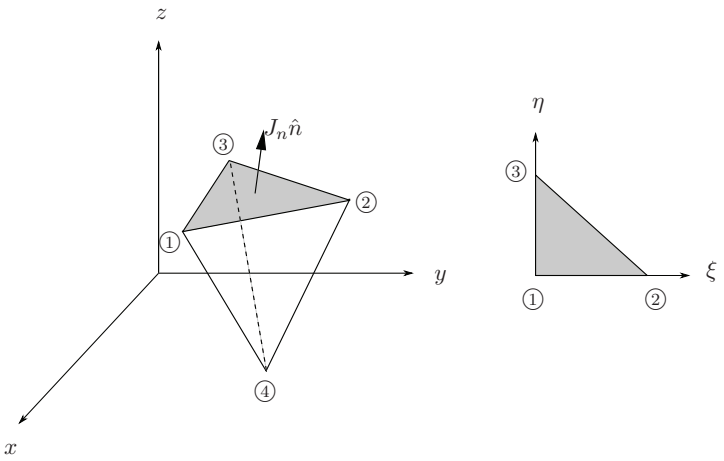

Figure 3.12: Mapping between the side of a daughter tetrahedron to which the fixed current electrode is connected and the side of a parent unit tetrahedron.

This means that the current has to be multiplied by the side area and the third part of that amount is assigned to each node at the endpoints of the side

$$\int_{\Gamma_e} J_n N_i\,\mathrm{d}\Gamma = J_n \int_{\Gamma_e} N_i\,\mathrm{d}\Gamma = J_n \frac{1}{6}|\mathcal{J}| = J_n \Gamma_e/3, \tag{3.61}$$

where $\Gamma_e = 2|\mathcal{J}|$ is the area of connecting side.

3.4.5 Stiffness matrix regularization

At least one node needs to have a known potential which will serve as a reference point. Otherwise the stiffness matrix will be overdefined and therefore singular. The value of V at node i is equivalent to x_i and if it is known, then the equation for x_i can be eliminated from the vector of nodal potentials $\mathbf{x}$. If a fixed-voltage electrode is present, for example, all nodes in contact with the electrode can be assigned that voltage and the associated equations eliminated from the solution.

If the Dirichlet boundary conditions are applied at nodes i and j, then x_i and x_j will be known and we can remove the ith and the jth rows from the matrix equation. The corresponding columns are removed from the stiffness matrix by subtracting them from the computed force vector. In this way,

the starting matrix equation

$$\begin{bmatrix} k_{11} & \dots & \boldsymbol{k_{1i}} & \dots & \boldsymbol{k_{1j}} & \dots & k_{1n} \\ \vdots & \ddots & \vdots & \ddots & \vdots & \ddots & \vdots \\ \boldsymbol{k_{i1}} & \dots & \boldsymbol{k_{ii}} & \dots & \boldsymbol{k_{ij}} & \dots & \boldsymbol{k_{in}} \\ \vdots & \ddots & \vdots & \ddots & \vdots & \ddots & \vdots \\ \boldsymbol{k_{j1}} & \dots & \boldsymbol{k_{ji}} & \dots & \boldsymbol{k_{jj}} & \dots & \boldsymbol{k_{jn}} \\ \vdots & \ddots & \vdots & \ddots & \vdots & \ddots & \vdots \\ k_{n1} & \dots & \boldsymbol{k_{ni}} & \dots & \boldsymbol{k_{nj}} & \dots & k_{nn} \end{bmatrix} \begin{bmatrix} x_1 \\ \vdots \\ \boldsymbol{x_i} \\ \vdots \\ \boldsymbol{x_j} \\ \vdots \\ x_n \end{bmatrix} = \begin{bmatrix} f_1 \\ \vdots \\ \boldsymbol{f_i} \\ \vdots \\ \boldsymbol{f_j} \\ \vdots \\ f_n \end{bmatrix} \tag{3.62}$$

becomes

$$\begin{bmatrix} k_{11} & \dots & k_{1,i-1} & k_{1,i+1} & \dots & k_{1,j-1} & k_{1,j+1} & \dots & k_{1n} \\ \vdots & \ddots & \vdots & \vdots & \ddots & \vdots & \vdots & \ddots & \vdots \\ k_{i-1,1} & \dots & k_{i-1,i-1} & k_{i-1,i+1} & \dots & k_{i-1,j-1} & k_{i-1,j+1} & \dots & k_{i-1,n} \\ k_{i+1,1} & \dots & k_{i+1,i-1} & k_{i+1,i+1} & \dots & k_{i+1,j-1} & k_{i+1,j+1} & \dots & k_{i+1,n} \\ \vdots & \ddots & \vdots & \vdots & \ddots & \vdots & \vdots & \ddots & \vdots \\ k_{j-1,1} & \dots & k_{j-1,i-1} & k_{j-1,i+1} & \dots & k_{j-1,j-1} & k_{j-1,j+1} & \dots & k_{j-1,n} \\ k_{j+1,1} & \dots & k_{j+1,i-1} & k_{j+1,i+1} & \dots & k_{j+1,j-1} & k_{j+1,j+1} & \dots & k_{j+1,n} \\ \vdots & \ddots & \vdots & \vdots & \ddots & \vdots & \vdots & \ddots & \vdots \\ k_{n,1} & \dots & k_{n,i-1} & k_{n,i+1} & \dots & k_{n,j-1} & k_{n,j+1} & \dots & k_{n,n} \end{bmatrix} \begin{bmatrix} x_1 \\ \vdots \\ x_{i-1} \\ x_{i+1} \\ \vdots \\ x_{j-1} \\ x_{j+1} \\ \vdots \\ x_n \end{bmatrix} =$$

$$= \begin{bmatrix} f_1 \\ \vdots \\ f_{i-1} \\ f_{i+1} \\ \vdots \\ f_{j-1} \\ f_{j+1} \\ \vdots \\ f_n \end{bmatrix} - \begin{bmatrix} k_{1,i} & k_{1,j} \\ \vdots & \vdots \\ k_{i-1,i} & k_{i-1,j} \\ k_{i+1,i} & k_{i+1,j} \\ \vdots & \vdots \\ k_{j-1,i} & k_{j-1,j} \\ k_{j+1,i} & k_{j+1,j} \\ \vdots & \vdots \\ k_{n,i} & k_{n,j} \end{bmatrix} \begin{bmatrix} x_i \\ x_j \end{bmatrix}. \tag{3.63}$$

Once the potential distribution is computed, the electric field is obtained using

$$\mathbf{E} = -\boldsymbol{\nabla} V = -\sum_{i=1}^{n} V_i \boldsymbol{\nabla} N_i. \tag{3.64}$$

3.5 Software implementation

This thesis work aims at discussing the numerical results obtained with the presented FE model in the context of the deep brain stimulation problem. Therefore, no emphasis has been put in the inhouse development of an original FE software.
Rather, our formulas as developed and discussed in the previous Section 3.4 have been implemented thanks to a commercial tool COMSOL [36], which provides all the needed facilities for pre-processing (mesher) and post-processing (specialized graphics) for the studied problem.

3.6 Conclusion

The combination of a well established powerful numerical technique with a new and more accurate strategy for living tissues, including conductive anisotropy is one of the main achievements in this chapter. To this, it must be added the discussion of the main electromagnetic quantities involved and the thorough discussion of the mathematical relationship between them. In particular the careful application of the selected boundary conditions (Dirichlet and/or Neumann) is of paramount relevance for the results obtained in the subsequent chapters.

Bibliography

[1] J. Malmivuo and R. Plonsey, *Bioelectromagnetism*. Oxford University Press, 1995.

[2] R. Plonsey and D. B. Heppner, "Considerations of quasi-stationarity in electrophysiological systems." *Bull Math Biophys*, vol. 29, no. 4, pp. 657–664, Dec 1967.

[3] P. L. Nunez and R. Srinivasan, *Electric Fields of the Brain*.

[4] Y. Yan, P. L. Nunez, and R. T. Hart, "Finite-element model of the human head: scalp potentials due to dipole sources," *Med. Biol. Eng. Comput.*, vol. 29, pp. 475–481, Sep. 1991.

[5] H. Hallez, B. Vanrumste, P. V. Hese, Y. D'Asseler, I. Lemahieu, and R. V. de Walle, "A finite difference method with reciprocity used to incorporate anisotropy in electroencephalogram dipole source localization." *Phys Med Biol*, vol. 50, no. 16, pp. 3787–3806, Aug 2005. [Online]. Available: http://dx.doi.org/10.1088/0031-9155/50/16/009

[6] N. G. Sepulveda, C. F. Walker, and R. G. Heath, "Finite element analysis of current pathways with implanted electrodes." *J Biomed Eng*, vol. 5, no. 1, pp. 41–48, Jan 1983.

[7] A. C. Eycleshymer and D. M. Shoemaker, *A Cross-Section Anatomy*. Appelton New York, 1911.

[8] P. M. Bonovas, G. A. Kyriacou, and J. N. Sahalos, "A realistic three-dimensional FEM of the human head," *Physiol. Meas.*, vol. 22, no. 1, pp. 65–76, Feb. 2001.

[9] H. C. Burger and van Dongen, "Specific electric resistance of body tissues." *Phys Med Biol*, vol. 5, pp. 431–447, Apr 1961.

[10] C. F. Kay and H. P. Schwan, "Specific resistance of body tissues." *Circ Res*, vol. 4, no. 6, pp. 664–670, Nov 1956.

[11] S. Rush, J. A. Abildskov, and McFee, "Resistivity of body tissues at low frequencies." *Circ Res*, vol. 12, pp. 40–50, Jan 1963.

[12] L. Geddes and L. Baker, "The specific resitstance of biological materials - a compendium of data for the biomedical engineer and physiologist," *Med. Bio. Eng*, 1967.

[13] D. L. Collins, A. P. Zijdenbos, V. Kollokian, J. G. Sled, N. J. Kabani, C. J. Holmes, and A. C. Evans, "Design and construction of a realistic digital brain phantom." *IEEE Trans Med Imaging*, vol. 17, no. 3, pp. 463–468, Jun 1998. [Online]. Available: http://dx.doi.org/10.1109/42.712135

[14] C. H. Wolters, "Influence of tissue conductivity inhomogeneity and anisotropy on eeg/meg based source localization in the human brain," Ph.D. dissertation, Univesitat Leipzig, 2003.

[15] P. J. Basser, J. Mattiello, and D. LeBihan, "Mr diffusion tensor spectroscopy and imaging." *Biophys J*, vol. 66, no. 1, pp. 259–267, Jan 1994.

[16] C. Ramon, P. Schimpf, and J. Haueisen, "Influence of head models on eeg simulations and inverse source localizations," *BioMedical Engineering OnLine*, 2006.

[17] R. V. Uitert, C. Johnson, and L. Zhukov, "Influence of head tissue conductivity in forward and inverse magnetoencephalographic simulations using realistic head models." *IEEE Trans Biomed Eng*, vol. 51, no. 12, pp. 2129–2137, Dec 2004. [Online]. Available: http://dx.doi.org/10.1109/TBME.2004.836490

[18] G. Marin, C. Guerin, S. Baillet, L. Garnero, and G. Meunier, "Influence of skull anisotropy for the forward and inverse problem in eeg: simulation studies using fem on realistic head models." *Hum Brain Mapp*, vol. 6, no. 4, pp. 250–269, 1998.

[19] D. Güllmar, J. Haueisen, M. Eiselt, F. Giessler, L. Flemming, A. Anwander, T. R. Knösche, C. H. Wolters, M. Dümpelmann, D. S. Tuch, and J. R. Reichenbach, "Influence of anisotropic conductivity on eeg source reconstruction: investigations in a rabbit model." *IEEE Trans Biomed Eng*, vol. 53, no. 9, pp. 1841–1850, Sep 2006. [Online]. Available: http://dx.doi.org/10.1109/TBME.2006.876641

[20] J. Haueisen, D. S. Tuch, C. Ramon, P. H. Schimpf, V. J. Wedeen, J. S. George, and J. W. Belliveau, "The influence of brain tissue anisotropy on human eeg and meg." *Neuroimage*, vol. 15, no. 1, pp. 159–166, Jan 2002. [Online]. Available: http://dx.doi.org/10.1006/nimg.2001.0962

[21] C. H. Wolters, A. Anwander, X. Tricoche, D. Weinstein, M. A. Koch, and R. S. MacLeod, "Influence of tissue conductivity anisotropy on eeg/meg field and return current computation in a realistic head model: a simulation and visualization study using high-resolution finite element modeling." *Neuroimage*, vol. 30, no. 3, pp. 813–826, Apr 2006. [Online]. Available: http://dx.doi.org/10.1016/j.neuroimage.2005.10.014

[22] D. Le Bihan, J. F. Mangin, C. Poupon, C. A. Clark, S. Pappata, N. Molko, and H. Chabriat, "Diffusion tensor imaging: concepts and applications," *J. Magn. Reson. Imaging.*, vol. 13, no. 4, pp. 534–546, Apr. 2001.

[23] D. S. Tuch, V. J. Wedeen, A. M. Dale, J. S. George, and J. W. Belliveau, "Conductivity tensor mapping of the human brain using diffusion tensor MRI," *Proc. Natl. Acad. Sci. USA*, vol. 98, no. 20, pp. 11 697–11 701, Sep. 2001.

[24] P. W. Nicholson, "Specific impedance of cerebral white matter." *Exp Neurol*, vol. 13, no. 4, pp. 386–401, Dec 1965.

[25] Y. Wang, D. R. Haynor, and Y. Kim, "An investigation of the importance of myocardial anisotropy in finite-element modeling of the heart: methodology and application to the estimation of defibrillation efficacy." *IEEE Trans Biomed Eng*, vol. 48, no. 12, pp. 1377–1389, Dec 2001.

[26] H. Hallez, B. Vanrumste, P. V. Hese, S. Delputte, and I. Lemahieu, "Dipole estimation errors due to differences in modeling anisotropic conductivities in realistic head models for eeg source analysis." *Phys Med Biol*, vol. 53, no. 7, pp. 1877–1894, Apr 2008. [Online]. Available: http://dx.doi.org/10.1088/0031-9155/53/7/005

[27] M. S. Hamalainen and J. Sarvas, "Realistic conductivity geometry model of the human head for interpretation of neuromagnetic data." *IEEE Trans Biomed Eng*, vol. 36, no. 2, pp. 165–171, Feb 1989. [Online]. Available: http://dx.doi.org/10.1109/10.16463

[28] B. Yvert, O. Bertrand, M. Thvenet, J. F. Echallier, and J. Pernier, "A systematic evaluation of the spherical model accuracy in eeg dipole localization." *Electroencephalogr Clin Neurophysiol*, vol. 102, no. 5, pp. 452–459, May 1997.

[29] B. N. Cuffin, D. L. Schomer, J. R. Ives, and H. Blume, "Experimental tests of eeg source localization accuracy in realistically shaped head models." *Clin Neurophysiol*, vol. 112, no. 12, pp. 2288–2292, Dec 2001.

[30] G. Scheler, M. J. M. Fischer, A. Genow, C. Hummel, S. Rampp, A. Paulini, R. Hopfengrtner, M. Kaltenhuser, and H. Stefan, "Spatial relationship of source localizations in patients with focal epilepsy: Comparison of meg and eeg with a three spherical shells and a boundary element volume conductor model." *Hum Brain Mapp*, vol. 28, no. 4, pp. 315–322, Apr 2007. [Online]. Available: http://dx.doi.org/10.1002/hbm.20277

[31] L. A. Neilson, M. Kovalyov, and Z. J. Koles, "A computationally efficient method for accurately solving the eeg forward problem in a finely discretized head model." *Clin Neurophysiol*, vol. 116, no. 10, pp. 2302–2314, Oct 2005. [Online]. Available: http://dx.doi.org/10.1016/j.clinph.2005.07.010

[32] H. I. Saleheen and K. T. Ng, "A new three-dimensional finite-difference bidomain formulation for inhomogeneous anisotropic cardiac tissues." *IEEE Trans Biomed Eng*, vol. 45, no. 1, pp. 15–25, Jan 1998.

[33] ——, "New finite difference formulations for general inhomogeneous anisotropic bioelectric problems." *IEEE Trans Biomed Eng*, vol. 44, no. 9, pp. 800–809, Sep 1997. [Online]. Available: http://dx.doi.org/10.1109/10.623049

[34] S. V. D. Broek, H. Zhou, and M. Peters, "Computation of neuromagnetic fields using finite-element method and biot-savart law," *Medical and Biological Engineering and Computing*, 1996.

[35] C. E. Miller and C. S. Henriquez, "Finite element analysis of bioelectric phenomena." *Crit Rev Biomed Eng*, vol. 18, no. 3, pp. 207–233, 1990.

[36] *COMSOL Multiphysics*, COMSOL AB., Sweden.

4 Application to deep brain stimulation

To evaluate the electric potentials generated by the deep brain stimulation (DBS), the general bioelectric problem should be solved with the help of a numerical tool, as explained in the previous chapter. In this chapter, the previously selected finite element (FE) model is adapted to the specific environment of DBS and provides the first results for the electric potential generated by this type of stimulation.
First, the DBS system itself is described as well as the models used in previous studies (Section 4.1). Second, the original anatomical model used throughout this thesis, is described in Section 4.2. In contracts with previously published models, this simplified model extends to the chest in order to includes all the elements of the electric loop involved in DBS. In order to increase the realism and accuracy of the model, the highly inhomogeneous and anisotropic brain tissues surrounding the stimulation electrode are characterized through data extracted from a patient diffusion MRI (DT-MRI). Finally, the sensitivity of the potential distribution in the brain with respect to variations of parameters such as the conductivity and the applied boundary conditions (BC) are evaluated in Section 4.3.

4.1 Electrical model of deep brain stimulation

As explained in Section 3.2, numerous electrical head models have been built for EEG prediction (direct problem) or for source localization (inverse problem). With the development of medical imaging and the associated enhancing of biological tissues knowledge, the complexity of these models has dramatically increased. The main effort in these studies has been put on the modelling of tissues excited by currents which are created in a localized bundle of neurons transmitting a neural message. Therefore, these approaches have chosen to model these microscopic sources as infinitesimal electric dipoles [1–10].
However, in DBS, the source generating the potential distribution is usually an electrode of a length in the order of millimeters. Modelling it as an infinitesimal source is not accurate and a special care must be taken to model the stimulation electrode [11].

4.1.1 Deep brain stimulation system

In DBS, the electric pulses are usually delivered to the tissues through a system like the one represented in Fig. 4.1(a). This system is composed of [12]:

- an implanted pulse generator (IPG) that generates the electric pulses
- an implanted cable made of several wires that makes a galvanic connection between the IPG and the various contacts of the stimulation electrode
- a stimulation electrode, composed of several contacts insulated from each other, which delivers the electric pulses to the surrounding tissues (see Fig. 4.1(b)).

The system can be used in several configurations (see Fig. 4.2):

- monopolar stimulation: one contact is active (Fig. 4.3(a)),

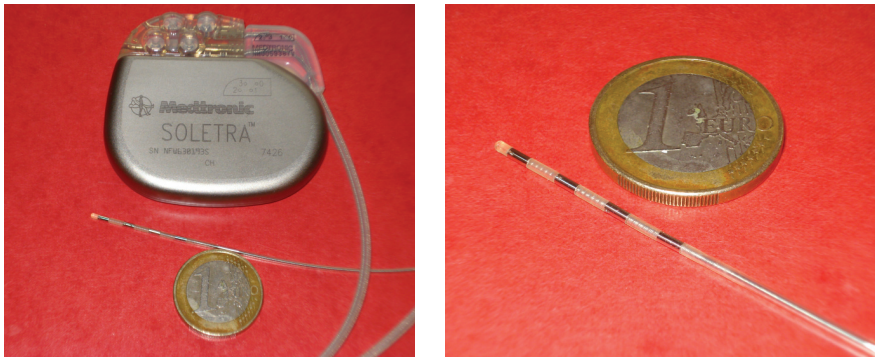

(a) Deep brain stimulation implantable system

(b) Stimulation electrode

Figure 4.1: Medtronic SOLETRA system for deep brain stimulation [12]. The system (a) is composed of a case containing the electronic system which generates the pulses, a bundle of wire and an electrode made of four contacts at its end (b). The case has one of its faces conductive and the other one insulated.

- multipolar balanced stimulation: several contacts are active and the sum of the currents going out of the contact is null (Fig. 4.3(b)),
- multipolar unbalanced stimulation: several contacts are active, the sum of the currents going out of the contact is not null and the difference have to go back to the IPG (Fig. 4.3(c)).

Either when the stimulation is monopolar or unbalanced, a return current electrode (RCE) must be set up in order to close the electric loop. The metallic case of the implanted pulse generator is usually used for that purpose. The SOLETRA stimulator [12] has all its faces electrically insulated except one, which acts as the RCE when needed.
Therefore the real BC of the DBS (see Fig. 4.4) are the following:

- on the stimulation contact surface, the stimulation parameters set the BC. For voltage stimulation, a fixed voltage must be set (Dirichlet type BC). For current stimulation, a fixed current must be set (Neumann type BC). When a contact is not activated, the continuity equations are applied.
- on the external boundary of the model, a fixed null Neumann BC is applied. That BC is set as the head is surrounded by air, which is an electric insulator, no current flux is crossing this boundary.
- on the conductive face of the implanted pulse generator, a Dirichlet BC sets a reference zero potential. This face is used as RCE in monopolar or unbalanced stimulation. On the other faces of the IPG, which are insulated, a null Neumann BC is applied, as no currents are crossing these interfaces.

As the IPG is remotely controlled, the parameters of the electric pulse (pulse width and frequency) as well as the type of stimulation chosen can be adjusted through the IPG even after the surgery.

The preferable configuration of the stimulation device is still discussed to treat movement disorders with DBS. Nevertheless, most of the clinicians are using monopolar configuration as it allows a more local stimulation (only the tissues surrounding one contact are activated) and therefore reduces side

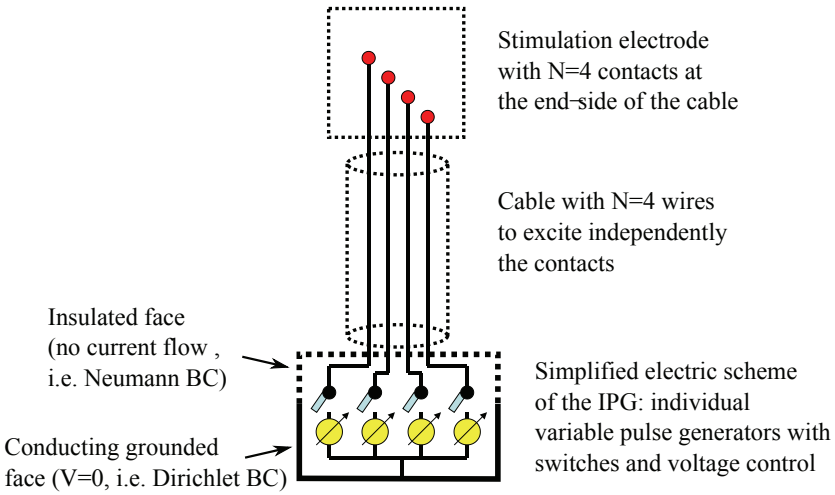

Figure 4.2: Simplified electric description of the implanted pulse generator.

effects [13]. When the bipolar balanced configuration is used, the tension set to one contact is usually opposite to the one applied on the other contact.
The DBS system can be either current or voltage controlled. Nevertheless, most of the implanted systems [12] are voltage controlled.
Considering the fact that monopolar configuration can be applied for the stimulation, the inadequacy of the infinitesimal dipole approach, used in most of the EEG studies to model the source, is clearly and plainly evident.

The Medtronic 3389 quadripolar device is the most commonly used system for DBS. Its electrode consists of a 1.27 mm-diameter cylinder made of four 1.5 mm height-contacts separated by 0.5 mm, as shown in Fig. 4.5. The contacts are made of conductive material (σ=5.99 10^7 S/m) and the space between each contact is made of insulator material (σ=5.99 10^{-7} S/m). These values are the limit values of the FE software used. The curved tip of this device is neglected in the model and is approximated by a straight cylinder of an equivalent height. As this cylinder and this curved tip are both made of insulating material, this replacement should only have a very minor impact on the global potential distribution. Nevertheless, this approximation may lead to an error for the potential evaluation at that precise place (the tip). Our approach is flexible enough to include a detailed treatment of the tip geometry and it would be worth in future studies to ascertain the real error incurred with this approximation.

The location of the electrode contact in the model is based on its anatomical position. The preferred site of stimulation for DBS applied for Parkinson's disease is the subthalamus nucleus (STN). The electrode contact position is therefore located with a small offset from the middle plan separating the two brain hemispheres.
The IPG is modelled by a box of $6 \times 5 \times 1$ cm ^{3}. These dimensions correspond to the Soletra system of Medtronic [12]. Unless specified, one of the main face of the box is set at the potential reference (0 Volt) to model the RCE needed to close the electrode loop in unbalanced stimulation. On the other faces, a null Neumann boundary condition is applied (no current going through the surfaces).

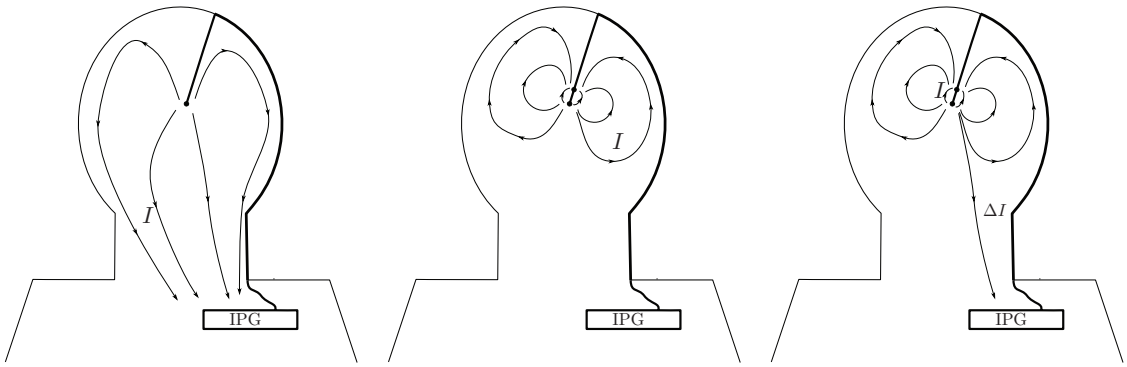

(a) Monopolar (b) Balanced (c) Unbalanced

Figure 4.3: Schematic views of the electric loops involved in DBS. (a) Monopolar stimulation: all the current going out of the stimulation electrode reaches the IPG in the chest. (b) Multipolar balanced stimulation: the sum of current going out of the electrodes is zero. (c) Unbalanced multipolar stimulation: the sum of currents going out of the electrode contact ΔI is not zero and must reach the return current electrode, here the IPG.

4.1.2 Description of the previous deep brain stimulation models

Several studies have been conducted lately with the purpose of evaluating the potential distribution generated by DBS and to predict their effect on the surrounding tissues. These studies have used different electrical brain models that can be classified as follows:

- An axisymmetric two-dimensional model, where the tissues have been considered as homogeneous and isotropic (Fig. 4.6 a) [14–18].
- A three dimensional cylindrical geometry to represent the homogeneous tissues surrounding the electrode (Fig. 4.6 b) [19–21]
- A cubic model including the inhomogeneous and anisotropic tissues surrounding the electrode (Fig. 4.6 c) [22–24]
- Butson *et al.* used a model extended to the head boundary to analyze the effect of deep brain stimulation (Fig. 4.6 d) [25].

All of them used a reduced model which does not include all the electric stimulation system. Therefore the approximation of setting a null Dirichlet BC to the external limits of their model to model the RCE has been made. So far, any complete and rigorous studies have been made (to our knowledge) to validate this approximation.

4.2 Description of the developed model

The model developed in this thesis aims at including all the tissues volumes involved in the whole DBS electric loop. For this reason it extends to the chest in order to include the IPG. The model is built with simple geometric elements such as cubes and cylinders to represent the main anatomical parts, namely the human head, neck and upper chest (see Fig. 4.7). Extensive numerical studies, including those performed in this thesis, have shown that the actual size of the body boundaries is of a very minor relevance here. The critical parameters affecting the quality and the accuracy of the results are:

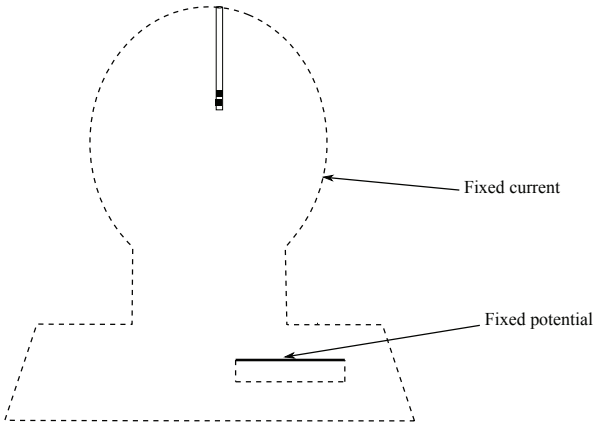

Figure 4.4: Two dimensional view of the real BC of DBS. On the surface of the stimulation electrode, the BC are set according to the stimulation parameters. On the external boundary of the model (dashed line) a null Neumann BC is applied. On the conductive face of the IPG (bold line), a fixed reference zero potential is applied, whereas on the other insulating faces (dashed line), a null Neumann BC is applied.

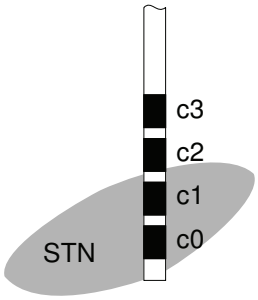

Figure 4.5: Schematic view of the quadripolar Medtronic electrode model, widely used in DBS. The black regions are the contacts (conducting material), while the rest of the structure is made of insulator. The labels denote the usual nomenclature used in clinical practice: C0 is the most distal contact and C3 is the most proximal one. Each contact is can be feed independently from the others by the IPG. The gray area depicts the STN.

- a good modelling of the conductive properties of tissues around the electrode
- an observance of the global boundary conditions to be fulfilled by the electric current flow.

Precisely, both conditions are accurately considered in the proposed model.
The deal was: once these conditions are fulfilled, what can be the improvements introduced in the model to maintain or improve accuracy without unduly increasing the computational complexity. This internal logic commands the inclusion on the model of neck and upper chest with the appropriate boundary conditions, to ensure an electric current flow as realistic as possible. On the other hand, for the geometrical treatment, the choice of highly simplified geometric structures to describe the biological tissues was considered a correct decision since it allows to maintain a reduced number of unknowns without modifying the electric loop followed by the currents. Indeed numerical experiments have shown that in these cases the modification of the geometrical elements (*e.g.* tetrahedrons, cylinders or spheres

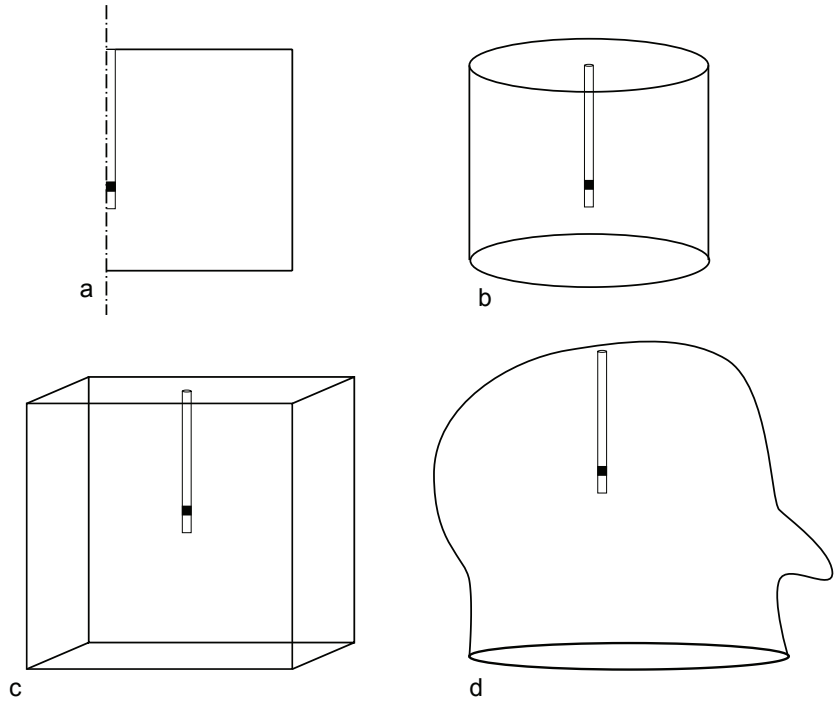

Figure 4.6: Schematic views of the previously used models. All these models have set a fixed 0 V potential to their boundaries. a) is an axisymmetric two dimensional model. b) is a three dimensional cylinder filler of homogeneous and isotropic medium. c) is a cubic three dimensional model using inhomogeneous and anisotropic tissues. d) is a three dimensional head model using anisotropic and inhomogeneous tissues.

instead of parallelepipeds) have a very low impact on the quantities of interest.

4.2.1 Tissue modelling

A reasonable number of different tissues, selected according to anatomical criteria, are used in the model. The choice of these tissues is mainly directed by previous models found in literature [4, 7] and by the availability of conductivity values for these tissues. This is depicted in Fig. 4.8, where each tissue is associated with a color.
The head is made of a parallelepiped containing the skull, which in turn includes the cerebrospinal fluid (CSF) and two hemispheres composed of white and gray matter. The rest is assimilated to muscle.
From the bottom of the skull two concentric cylinders go down to the bottom boundary to model the spinal cord: the outer represents bone while the innermost represents spinal cord. The neck is made of two concentric cylinders. The outermost models the skin while the innermost is assimilated as muscle and represents the tissues of the neck.
The upper chest is a parallelepiped crossed by the spinal cord. It is made of muscle and contains a small box which represents the IPG. The bones are not taken into account in this model since they present a very low conductivity and therefore are unlikely to be crossed by the electric loop.

Numerous studies have been conducted to quantify the electrical properties of the biological

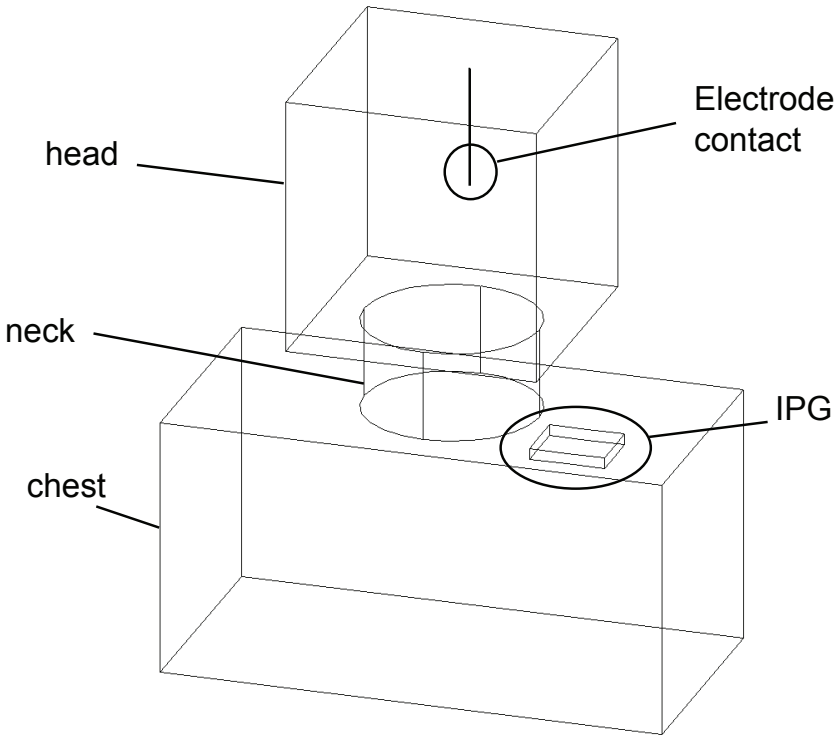

Figure 4.7: Simplified view of the three-dimensional model composed of: the head, the neck and the chest with the implanted DBS system.

tissues [26–31]. Nevertheless, the values provided by these studies show important variations. This is due to either the variability of these properties from a body to another or to the hard process of isolating one class of tissue to measure its electrical characteristics.

4.2.2 Global indicators for ascertaining the influence of the tissue conductivity

In order to extract information from the potential distribution, global indicators are developed.

To quantify the impact of the conductivity on the potentials, the global impedance R_{Tissue} of the tissues crossed by the current released during stimulation is computed. For a homogeneous medium, the resistance R [Ω] is given by

$$R = \frac{1}{\sigma}\frac{l}{S} \tag{4.1}$$

where l [m] is the length of the medium, S [m^2] its cross section and σ [S] its conductivity (see Fig. 4.9). Therefore the relation R-σ is trivial.

But in a inhomogeneous medium, moreover having a variable cross section such as the model developed here, resistance can only be computed as

$$R_{\text{Tissue}} = \frac{\Delta V}{I} \tag{4.2}$$

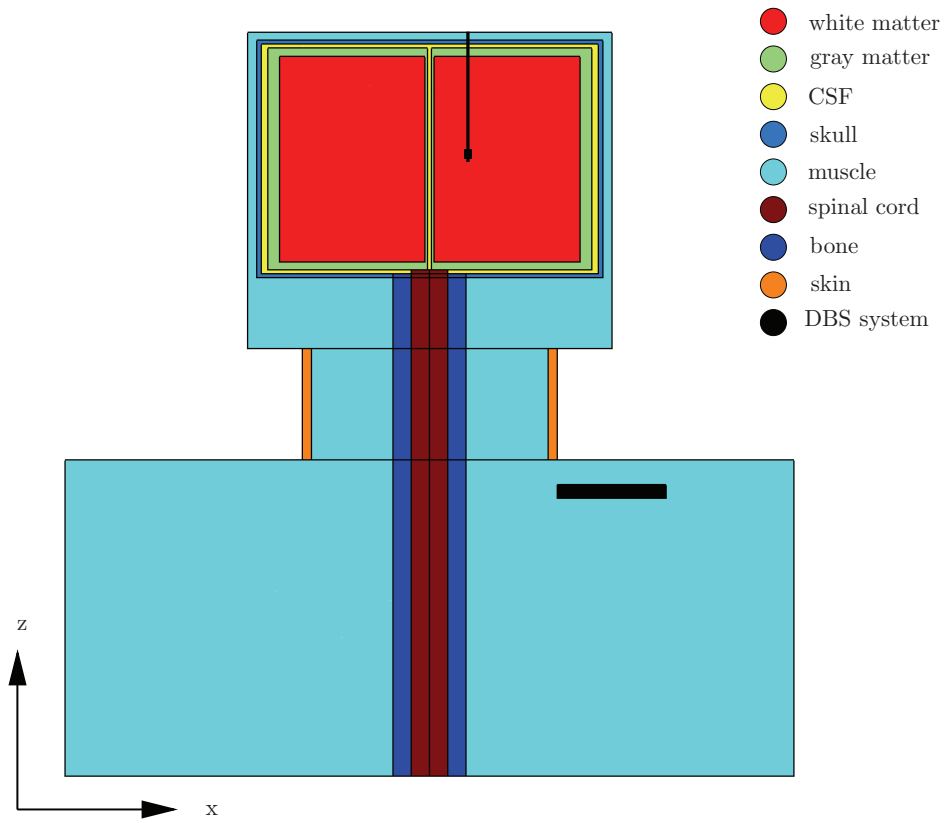

Figure 4.8: Coronal cutting view of the biological tissues used in the model.

where ΔV is the potential difference between the two electrodes involved in the stimulation (see Fig. 4.10(a) for monopolar case and Fig. 4.10(b) for bipolar case). Indeed, according to the anatomy and the current path, the conductivity of each tissue has its own impact. The total current I is computed by the surface integration of the current density on one of the electrode surfaces. When more than two electrodes are involved in the stimulation (unbalanced stimulation), the situation becomes much more complicated, since an electrical multiport equivalent circuit must be considered including more than one resistance.
R_{Tissue} is an excellent global indicator, as it takes into account any variation of conductivity for any tissue.

Another way to quantify the impact of the conductivity values used in the model is to compute the half pulse amplitude volume (HPAV). The HPAV is the volume of tissue where the potential ranges from the pulse voltage amplitude value U_{pulse} to its half value (see Fig. 4.11(a) for monopolar case and Fig. 4.11(b) for bipolar case). For example, for a voltage stimulation amplitude of $U_{\text{pulse}} = 1$ Volt, then the HPAV is the volume of tissue having a potential between 0.5 and 1 Volt. The HPAV provides an information on the potential repartition and more especially on the gradient of the potential amplitude. A small HPAV is obtained for a high amplitude gradient of potential, while a low amplitude gradient of potential induces a big HPAV. The knowledge of the potential variation is useful in electrical stimulation. As explained in Rattay's study [32], the activation of neurons is indeed linked to the second

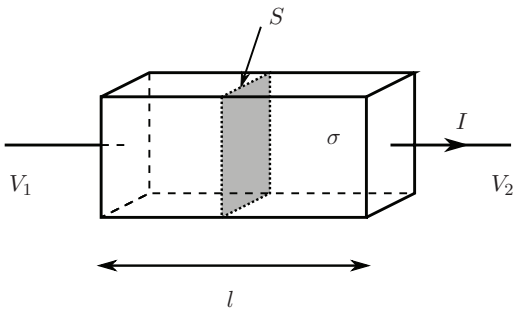

Figure 4.9: Resistance of a homogeneous volume with a constant cross section.

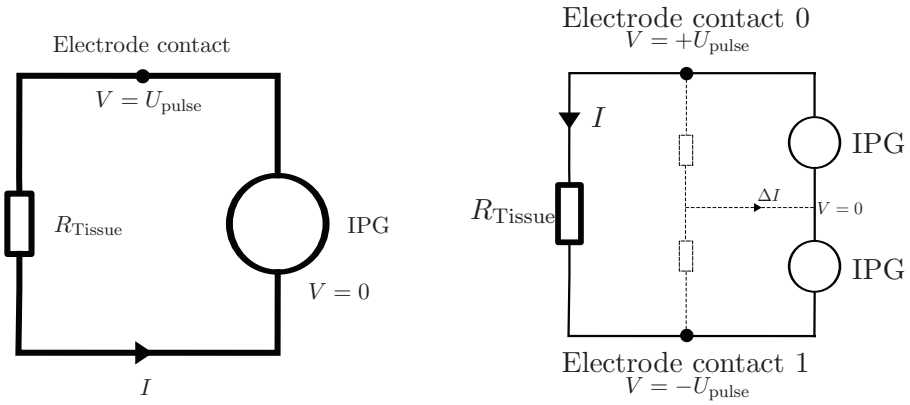

(a) monopolar stimulation (b) bipolar stimulation

Figure 4.10: Illustration of the electrical equivalent circuit in for monopolar (a) and bipolar balanced (b) stimulation. For bipolar balanced stimulation, the current differential $\Delta I = 0$ and therefore R_{Tissue} defines the impedance between the two active contacts.

spatial derivative of the potential. Therefore, a high HPAV is likely to activate less neurons than a small one, as the spatial variation is smoother. The equivalent radius of the HPAV can also be defined as

$$r_{\text{eq}} = \sqrt[3]{\frac{3 \cdot \text{HPAV}}{4\pi}}. \tag{4.3}$$

These two indicators are dependant of the conductivity of the tissues, but also of the BC applied to the model. Indeed, R_{Tissue} is computed for the tissues between the two electrodes involved in the stimulation. In monopolar stimulation, one of these electrodes is directly modelled by the BC. Therefore, a special care should be taken to model these BC.

4.2.3 Critical region

Numerous studies, mainly for EEG applications, have shown the importance of the tissue modelling in the vicinity of the source [4, 7, 8]. Therefore, special care is taken to model critical region formed by the tissues surrounding the electrode contact.
Ideally, the dimensions of the critical region should be comparable with the volume of tissue activated

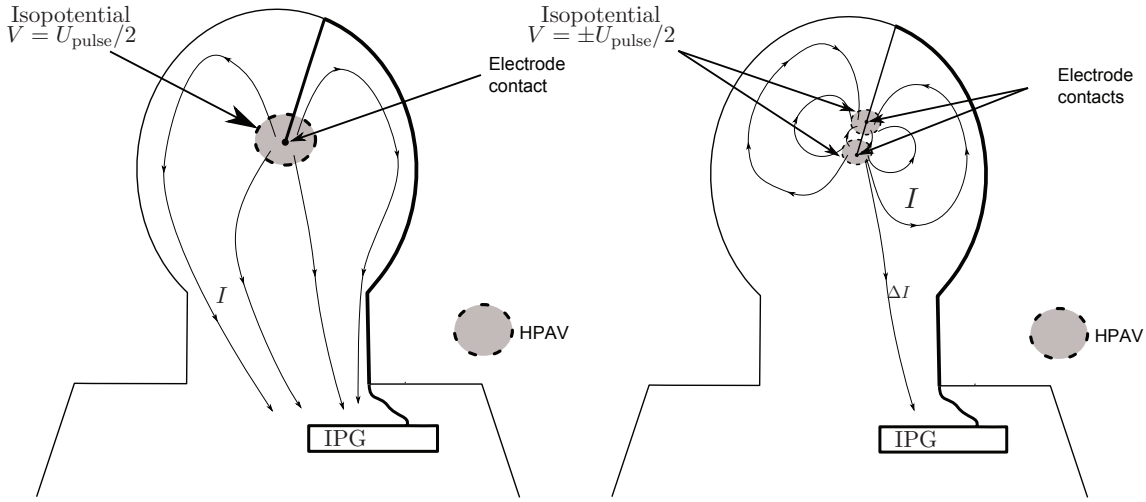

(a) monopolar stimulation (b) bipolar stimulation

Figure 4.11: Illustration of the half pulse amplitude volume (HPAV). The HPAV is the volume of tissue having a potential ranging between 100% and 50% of the pulse amplitude U_{pulse}.

but this information is only known a posteriori, so as a reasonable assumption must be made a priori on the size of the critical region. This assumption must be compatible with the available computer resource. Nevertheless the clinical observations showed that the extent of stimulation remains within a radius of several millimeters.

The use of the DT-MRI to provide information on the direction of fibers makes possible the introduction of anisotropic conductivity in the head models. Several studies have shown that the introduction of anisotropic conductivity in EEG models leads to a more realistic modelling of the human head and therefore to improvements in the EEG prediction and on the dipole localization [3, 5, 9, 23, 33–35].

Modelling each nerve and all microscopic cells constituting the brain structure is impossible (or at least impracticable) today. A macroscopic approximation is then used to assign a global electrical property to each discretized part of the brain.
This macroscopic approximation for the conductivity of tissue is based on the diffusion tensor imaging (DT-MRI) of a selected patient. First, the stimulation target is localized anatomically on the DT-MRI data by a clinician. Then an array of voxels (three dimensional elements of composing the DT-MRI data) surrounding the target is extracted and converted into an array of electrical conductivity tensors (see Section 3.3). An array of parallelepipeds having the same size and dimensions than the DT-MRI voxels (in this study an array of $8 \times 8 \times 5$ elements of $1.5 \times 1.5 \times 3$ mm^3) is created around the stimulation electrode model so the information included in the medical imaging is maximized. The conductivity tensors are then assigned to each elements, taking care that the targeted voxel is assigned to the element around the stimulation electrode contact. This array of tissue, referred as refined tissue, is shown in Fig. 4.12(a). The Fig. 4.12(b) shows the stimulation electrode model and the conductivity ellipsoids obtained from the DT-MRI for an $8 \times 8 \times 5$ array located around the stimulation electrode. The conductivity tensor ellipsoids show a high inhomogeneity, not only in their volumes but also in their shapes, which is a typical characteristic of the brain tissues. Indeed, white matter shows high

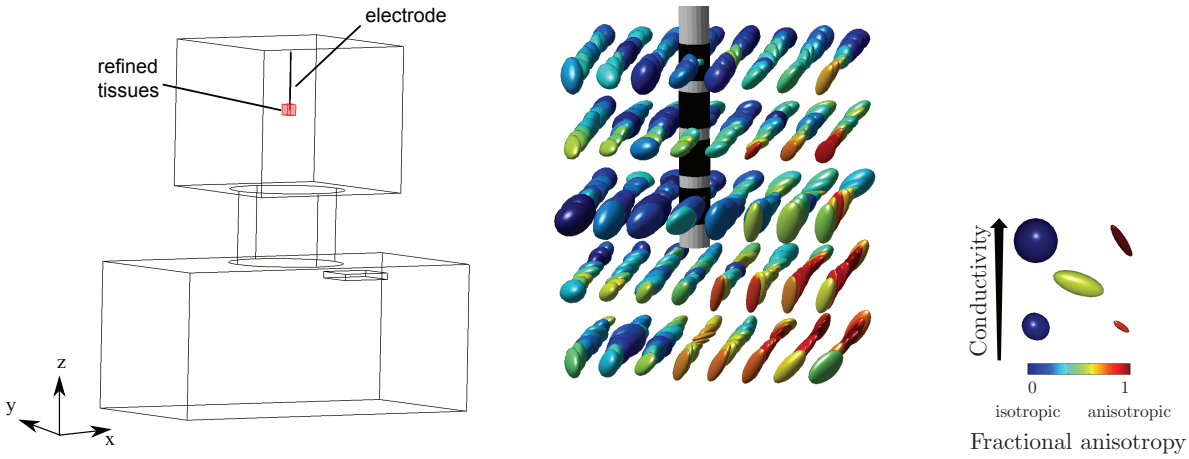

(a) General view of the refined tissues (b) Tensor ellipsoids of the refined tissues

Figure 4.12: Illustration of the refined tissues position and of their anisotropic conductivity. a) To improve the quality of the model, refined tissues (in pink) are located in the vicinity of the stimulation electrode. These tissues have their conductivity based on a high definition DT-MRI of each patient. b) The stimulation electrode is surrounded with the ellipsoids representing the anisotropic electrical conductivity. The color of each ellipsoid shows the fractional anisotropy (equation (3.19)). A blue color indictates an isotropic conductivity while a red color depicts a high anisotropy. The volume of the ellipsoid is linked to the value of the conductivity. A highly conductive tissue (*i.e* CSF) will have a bigger volume than a tissues showing low conductivity (*i.e* white matter).

anisotropy and CSF is a highly conductive media.

4.2.4 Finite element meshing of the model

The mesh generation for the model is managed directly by the finite element software COMSOL [36]. The electric potentials need to be accurately computed in the vicinity of the source. The neural effects are analyzed in this region. Since the electric field changes rapidly in this area, a high mesh density is forced in the critical region.

The maximum mesh element size is set to 0.2 mm on each electrode contact. An illustration of the high mesh density around the stimulation electrode can be seen in Fig. 4.13.
The final model is made of approximately 400 000 unknowns. The mesh density provides good results for the quantities under study. Indeed, as a proof of numerical convergence and stability, it has been checked that doubling the node number changes the potential values by amounts always smaller that 1.75%.

4.3 Sensitivity of the model to different parameters

In this section the sensitivity of potential distribution of the model to several parameters is investigated. First, the sensitivity of the model to the use of anisotropy is evaluated. Second, the values of the tissues conductivity are varied and the impact on the quantificators defined in previous section are analyzed. Finally, the effect of the applied BC is studied.

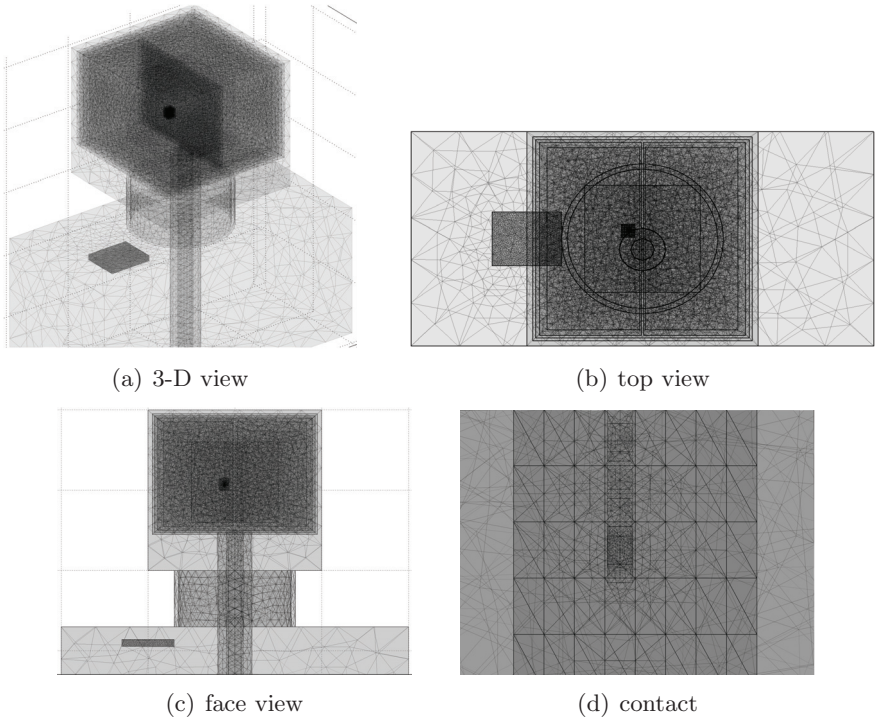

(a) 3-D view (b) top view

(c) face view (d) contact

Figure 4.13: Different cutting views of the mesh used in the model. The darker, the finer the mesh density. In (d) is shown a zoomed view of the stimulation electrode. The mesh in that area is forced to have a high density, as an accurate field value is required.

4.3.1 Influence of the anisotropic tissue modelling

At first glance, to evaluate the effect of anisotropy one could just compare a simple model where the refined tissues are modelled by an isotropic conductivity (that of white matter) with a more evolved model where tensorial conductivities based on DT-MRI is used within the refined region. Unfortunately, these changes imply not only the use of anisotropic rather than isotropic conductivity but also a global modification of the conductivity values. Therefore, quantifying the improvements obtained with the anisotropic conductivity is not an easy task.
Fig. 4.14 shows two isopotential surfaces corresponding approximately to the same volume. The first one, obtained using isotropic conductivity, shows an regular elliptical shape, while the one obtained using anisotropic conductivities shows a more irregular shape. This demonstrates that using anisotropic values impacts the potential distribution generated by the stimulation. The potential gradient will follow the direction of the largest conductivity. This leads to a more pronounced dependence of the potentials with the angular direction.

4.3.2 Influence of the tissue conductivity

The influence of the electrical tissue properties on the the potential distribution in EEG models has been investigated in [4, 7, 8]. These studies have shown that the values of conductivity used for the tissues surrounding the source have an important impact on the potential amplitude and distribution. In [4], the resistivity values found in literature has been reviewed. The sensitivity of forward model

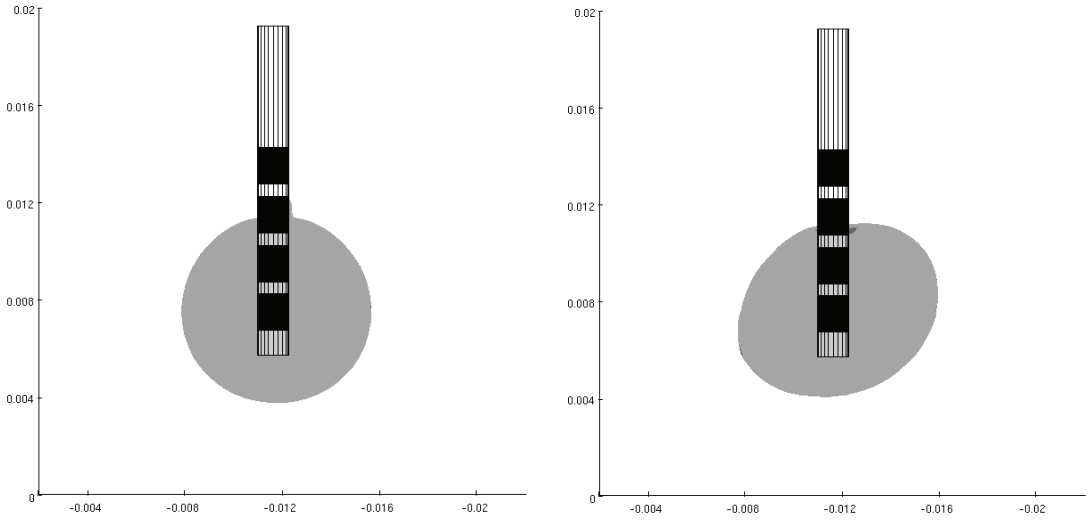

(a) Isotropic conductivity (b) Anisotropic conductivity

Figure 4.14: Illustration of the changes when using anisotropy. The left figure shows a volume obtained using isotropic conductivity. The obtained volume is regular and almost spherical. Right figure shows a volume having approximately the same size, but obtained using anisotropic conductivity. The obtained volume is non regular and is deformed according to the anisotropic conductivity of the tissue.

of EEG with respect to the resistivity of each class of tissue has been computed. Each class of tissue has been set to a mean conductivity value and an upper and lower bound (usually set to ± 50% of the mean value). Only in the case of widely varying values other bounds have been chosen. The range of the chosen lower and upper bounds represents a good approximation for all the resistivity values which can be found in the literature. This study has provided rounded up resistivity values in ω cm.
The previously described methodology has been applied to evaluate the sensitivity of the model to tissue conductivity. The conductivity values are taken from [4]. They are given in Table 4.1. Contrary to the EEG applications, conductivity values are considered rather than resistivity. This choice is motivated by the fact that the values of conductivity will be used to create the anisotropic conductivity based on water diffusion tensors.
To evaluate the sensitivity of the model to a specific class of tissue, each value is set to its upper and lower value, as defined in Table 4.1, while keeping the others to the mean value.
It is worth mentioning that the conductivity values shows a very similar degree of incertitude in most tissues, save for muscle and skull, where the open literature provides a rather important disparity of the announced results.

Case of monopolar stimulation

The sensitivity of monopolar DBS model to the electrical conductivity of tissues is investigated. The computed impedance and the HPAV results are given in Table 4.2.

The variation of the value of conductivity for the refined tissues leads to major variation of R_{Tissue} (+27% and -29% compared to the impedance using mean values). Since the refined tissues surround the stimulation electrode, the current must flow through these tissues (see Fig. 4.15). Therefore, they play a major role in the total impedance seen by the stimulation system.

Table 4.1: Conductivity of the human tissues used in the proposed model (values extracted from [4])

σ_{Tissue} $[S.\text{m}^{-1}]$	mean	lower	upper
Refined tissues	1.538	1.026 (66%)	3.076 (200%)
CSF	1.538	1.026 (66%)	3.076 (200%)
Muscle	0.1	0.056 (56%)	0.5 (500%)
Skull	0.0063	0.002 (31%)	0.0125 (200%)
Gray Matter	0.33	0.222 (66%)	0.667 (200%)
White Matter	0.143	0.095 (66%)	0.286 (200%)
Skin	0.434	0.29 (66%)	0.869(200%)
Bone	0.04	0.0267 (66%)	0.08 (200%)
Spinal cord	0.154	0.103 (66%)	0.308(200%)

Table 4.2: Sensitivity of the model of monopolar DBS to the tissue conductivity

	$R_{\text{Tissue}}[\Omega]$		relative error [%]		HPAV $[\text{mm}^3]$	
Type of tissue	σ_{upper}	σ_{lower}	σ_{upper}	σ_{lower}	σ_{upper}	σ_{lower}
base model	1001		0		272	
refined tissue	709	1271	-29	+27	20563	61
muscle	779	1183	-22	+18	33	3803
skull	992	1029	-0.9	+3	400	241
CSF	993	1006	-0.8	+0.5	243	287
gray matter	996	1004	-0.5	+0.3	254	282
white matter	939	1055	-6	+5	134	582
skin	977	1049	-2	+5	202	332
bone	997	1002	-0.4	+0.1	260	277
spinal cord	998	1002	-0.3	+0.1	260	277

The impact of the muscle conductivity on R_{Tissue} is important (+18% and -22%). This result can be explained by several ways. First, most of the model is composed of muscle and its location makes that the current has to go through. Moreover, as pointed out in Table 4.1, the variation of the estimated conductivity of muscular tissue is important. On the other hand, it is worth noticing that the cross section of muscle is big, which according to equation (4.1) should reduce the value of R_{Muscle}.

White matter surrounds the refined tissues. The current is therefore forced to go across this tissue. But here also the cross section reduces the impact of that class of tissue, since changing its conductivity value between its extreme accepted values only modifies R_{Tissue} of less than 6%.
The current is also forced to go across the neck to reach the RCE. Its preferred path is to go through the tissue having the highest conductivity on the skin. Notice that despite of its location, in the outermost surface of the model, the skin conductivity has a big influence on the total impedance (+5% and -2%).
For the remaining classes of tissues, the changes obtained when changing the value of conductivity are not significant (below 1%).

The HPAV is also influenced by changing the conductivity of tissues. The same type of tissue have an important influence on the total impedance also have a great effect on the HPAV. Nevertheless, the impact on the HPAV is opposite if the considered tissue is in the vicinity or far from the stimulation electrode.
This can be explained as follows. The voltage drop between two points and hence the slope of the voltage variation with distance is directly proportional to the medium resistance and therefore inversely proportional to conductance. So higher values of conductance yield lower slopes of the potential curve. Now there are two fixed values of this curve, namely the U_{pulse} value at the contact electrode level and the reference zero value at the IPG position (see Fig. 4.16).
If a change of slope is forced in the proximal region (the critical region near the electrode) or in the

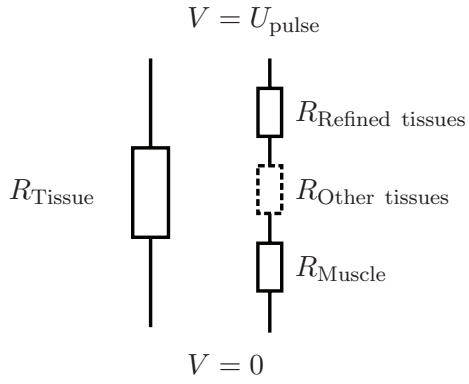

Figure 4.15: The total resistance of the tissue R_{Tissue} can be decomposed is a sum of resistance. As refined tissues and muscle are surrounding the electodes, the current have to go through these classes of tissue. The rest of the resistance is made by the other tissues.

distal region (far from the electrode), the potential curves must forcefully evolve as in, respectively, Fig. 4.16(a) and Fig. 4.16(b), since the potential is a continuous function. Now if the mid point in the vertical axis (50% of U_{pulse}) which is used to define the HPAV we see by plain geometry that HPAV increases when conductivity increases in the proximal region (Fig. 4.16(a)). But the same increase of conductivity in the distal region will produce a decrease of the HPAV Fig. 4.16(b).
These phenomena are particularly evident when changes of conductivity are applied to muscle with white matter playing the second role in the list of relevant tissues.

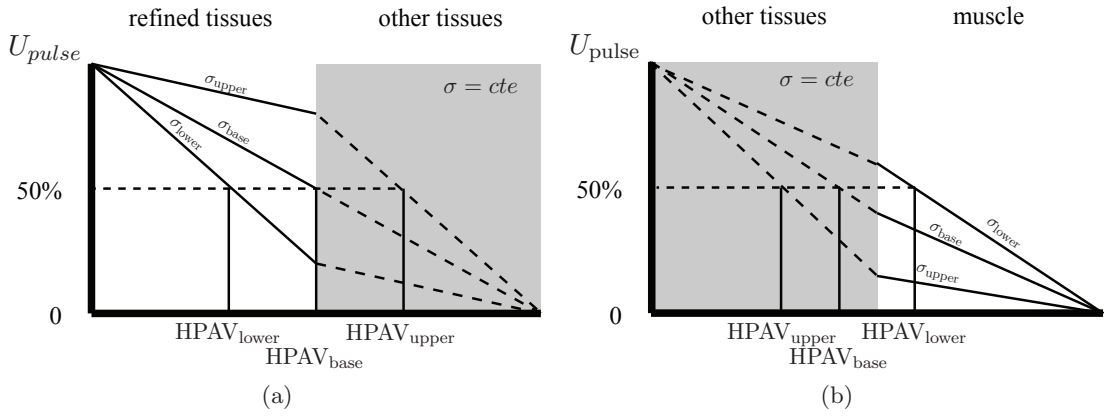

Figure 4.16: Illustration of the effect of the change of the conductivity on the HPAV.

Case of bipolar balanced stimulation

In a bipolar stimulation, the current loop involved is much smaller than in a monopolar stimulation. The current emitted by the positive electrode returns to the negative electrode and the differential current ΔI (see Fig. 4.10(b)) is not significant compared to the current between the two contacts.
Only the conductivity of the tissues in the vicinity of the stimulation electrodes (refined tissues and white matter in the critical region) might influence the potential distribution in bipolar stimulation.

The obtained results are showed in Table 4.3.
As expected, doubling the resistivity of the refined tissues leads to a double tissue impedance. When changing the conductivity value of the white matter, the variation of impedance are negligible. The tissues located further to the stimulation electrode than the refined tissues have a negligible impact and to the electric loop involved in bipolar stimulation.
Changing the value of conductivity in bipolar model does not impact the HPAV, which remains constant with the changes. As the electric loop is going across only one class of tissue (the refined tissues), changing the conductivity value of this class does not affect the potential distribution.

Table 4.3: Sensitivity of the model of bipolar balanced DBS to the tissue conductivity

	$R_{\text{Tissue}}[\Omega]$		relative error [%]		HPAV [mm^3]	
Type of tissue	lower	upper	lower	upper	lower	upper
base model	864		0		13	
refined tissue	1274	424	+47	-51	12.9	13.1
white matter	864	868	0	-0.4	13.0	12.9

Case of multipolar unbalanced stimulation

These techniques are rarely used in DBS. Since the current is going both between the active electrode contacts and to the IPG, the influence of the tissue conductivity could be obtained as a linear combination of the results associated to the two previous cases.

4.3.3 Influence of the boundary conditions

In this section, the influence of the BC applied on the model is investigated.
Most of the previous studies on DBS have used the same reduced model to investigate bipolar and monopolar stimulation [14–17,20,21,23–25,37,38]. The choice of the BCs applied on the limits of these model was usually the same for bipolar and monopolar configuration, namely a fixed zero potential on the external boundary (see Fig. 4.6). This boundary condition is fully justified for balanced bipolar stimulation. In effect, it has been shown in Section 4.3.2 that tissues located away from the source do not impact the potential distribution. The currents reaching the tissues located away from the electrode are negligible, and therefore fixing a null Neumann or Dirichlet condition on the external boundary is equivalent.
In monopolar stimulation, applying a zero potential on the external boundary sets up a RCE and then only one part of the electric loop is considered. However, the entire electrical loop involved in monopolar STN DBS includes all the biological tissues between the stimulation electrode active contact and the RCE, i.e. the IPG.
To evaluate the influence of the RCE model, three full loop models are used and compared with a commonly used model of reduced size that is considered as the reference.

Description of the return current electrode models

Four RCE models are investigated. They present various types of BC, as depicted in Fig. 4.17:

- BC I: the IPG is located in the chest. One of the main faces (30 cm^2) of the box is set to the reference potential (0 Volt) while the other faces are considered as isolating surfaces (no current flow through the surfaces).
- BC II: the IPG is located in the chest and has its two main faces set to 0 Volt. The area of the RCE is then doubled (60 cm^2).

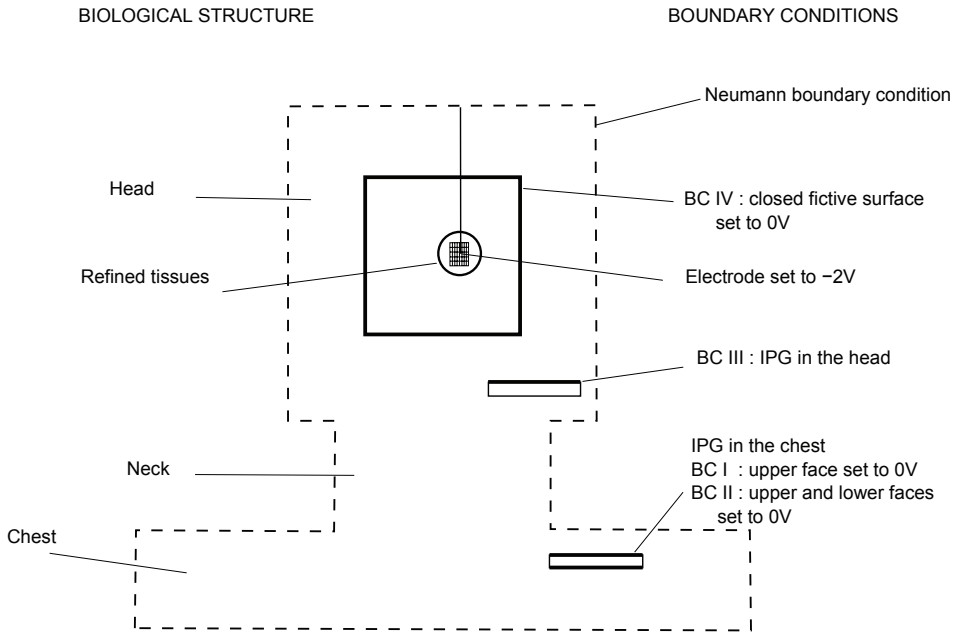

Figure 4.17: Illustration of the four return current electrode (RCE) models compared in this study. BC I – the IPG is located in the chest and its main side is set to 0 Volt. BC II – the IPG is located in the chest and its two main sides are set to 0 Volt. BC III – the IPG is located at the bottom of the head and its main side is set to 0 Volt. BC IV – an artificial cubic boundary is created (10 cm side). The surface of this cube is set to 0 Volt to recreate the boundary condition used in previous studies. Refined tissues having their properties based on the DT-MRI can be seen in the center of the head.

- BC III: the IPG is located in the bottom of the head, closer to the electrode (see Fig. 4.17), with one face set to 0 Volt.
- BC IV: the surface of a 10 cm side cube (600 cm^2) surrounding the stimulation electrode is set to 0 Volt.

BC IV is the most currently used model [14, 16, 17, 21, 23, 24]. Therefore, this BC will be used as benchmark to ascertain the improvements obtained by the more sophisticated model, BC I, that is used in this thesis. BC II and BC III are used to show the influence of, respectively, the size and the position of the RCE.

Influence of the return current electrode model in monopolar stimulation

The evaluated impedance of the tissues located between the electrode contact and the RCE in monopolar stimulation are reported in Table 4.4 for the four RCE models. The HPAV are also given, as well as the equivalent radius r_{eq}.
The highest value of impedance is obtained with the the RCE model BC I (1001 Ω). For this case, we observe an increase of the tissue impedance of 48% compared to the reference boundary condition model (BC IV). Doubling the surface of the RCE (BC II) induces a small decrease of the impedance (953 Ω). When moving the RCE to the base of the head, the impedance reaches 853 Ω. Finally, using the boundary condition BC IV yields to an impedance value of 674 Ω.

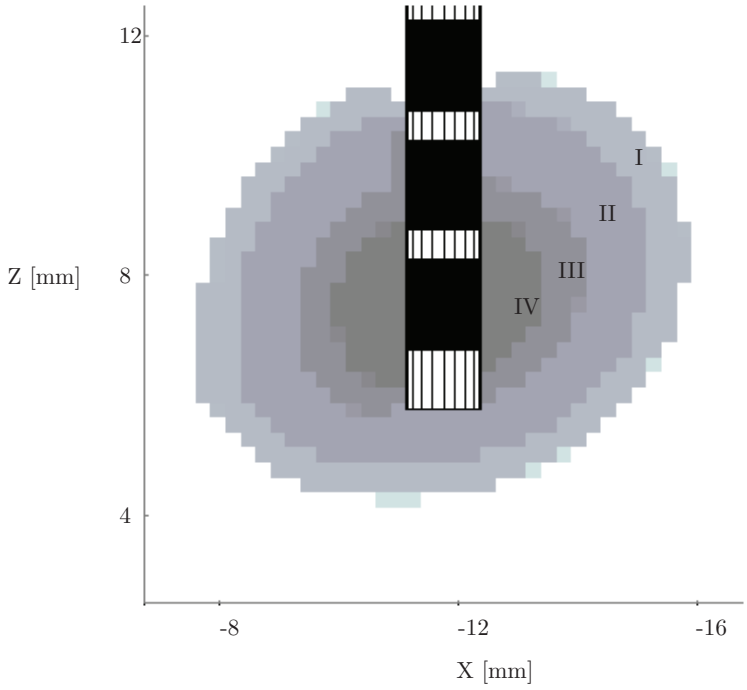

Figure 4.18: Isopotential surfaces of half the pulse amplitude obtained using four return current electrode (RCE) models (I stands for BC I). The potentials generated by the stimulation decrease more rapidly when the surface set to 0 Volt is closer (IV, III) or larger (II) than when using the most realistic model for the RCE (I).

The potential distribution is also affected by the RCE model, as exposed in Fig. 4.18. Isopotential surfaces of the half pulse amplitude are shown. The potentials generated by the stimulation decrease more rapidly when the 0 Volt surface is closer to the electrode contact and/or larger. Inversely, the total resistance of the tissues decrease when the RCE model surface increases and/or when its position is closer. So, as anticipated, the more accurate is the model, the smaller are the results for R_{Tissue} and HPAV. In other words, the values of R_{Tissue} and HPAV are largely underestimated with the standard models available in the literature.

4.4 Conclusion

In this chapter, the model used to to compute the potential generated by the stimulation electrode in deep brain stimulation has been presented. Opposite to the models used in previous studies, this model encompasses the head, the neck and the upper chest to include the full electric loop involved in DBS. This electric loop is composed of the stimulating electrode, the implanted generator and all the tissues located in between. The use of a full electric loop model, while not necessary when studying balanced bipolar stimulation, is mandatory in studies of monopolar stimulation. It has been shown that whereas all the tissues crossed by the stimulation current impacts the impedance seen by the stimulation system and modifies the potential distribution, only the ones surrounding the active electrodes have a relevant impact. It has also been shown that the boundary condition usually applied in previous studies leads to important differences in the prediction of the potential distribution compared to the one applied here, which is more realistic.

Table 4.4: RCE model influence on the impedance and the potential distribution

RCE model	R_{tissue} [Ω]	R_{tissue} relative error [%]	HPAV [mm^3]	r_{eq}
BC I	1001	+48	272	4.02
BC II	953	+40	160	3.36
BC III	853	+27	49	2.27
BC IV	674	0	19	1.66

The effects of these modelling aspects on the potential distribution have been shown, but their neurological effects on the stimulated tissues are still hard to quantify. According to Rattay [32], the activation of a neuron is linked to the second spatial derivative of the potential. As the spatial potential decrease from the electrode is influenced either by the tissues conductivity and the boundary conditions applied, it is likely that the volume of tissue stimulated is also affected by these parameters. In any case, as far as only electric quantities are discussed, this work shows clearly that key quantities like the total tissular resistance R_{Tissue} and the radius of the HPAV could be strongly underestimated (roughly a factor two) by current approaches.
In the next chapter, neuron models will be introduced in the potential field obtained by the FE simulation in order to quantify the amount of tissue activated by the stimulation.

Bibliography

[1] S. V. D. Broek, H. Zhou, and M. Peters, "Computation of neuromagnetic fields using finite-element method and biot-savart law," *Medical and Biological Engineering and Computing*, 1996.

[2] H. Buchner, G. Knoll, M. Fuchs, A. Riencker, R. Beckmann, M. Wagner, J. Silny, and J. Pesch, "Inverse localization of electric dipole current sources in finite element models of the human head." *Electroencephalogr Clin Neurophysiol*, vol. 102, no. 4, pp. 267–278, Apr 1997.

[3] H. Hallez, B. Vanrumste, P. V. Hese, S. Delputte, and I. Lemahieu, "Dipole estimation errors due to differences in modeling anisotropic conductivities in realistic head models for eeg source analysis." *Phys Med Biol*, vol. 53, no. 7, pp. 1877–1894, Apr 2008. [Online]. Available: http://dx.doi.org/10.1088/0031-9155/53/7/005

[4] J. Haueisen, C. Ramon, M. Eiselt, H. Brauer, and H. Nowak, "Influence of tissue resistivities on neuromagnetic fields and electric potentials studied with a finite element model of the head." *IEEE Trans Biomed Eng*, vol. 44, no. 8, pp. 727–735, Aug 1997.

[5] J. Haueisen, D. S. Tuch, C. Ramon, P. H. Schimpf, V. J. Wedeen, J. S. George, and J. W. Belliveau, "The influence of brain tissue anisotropy on human eeg and meg." *Neuroimage*, vol. 15, no. 1, pp. 159–166, Jan 2002. [Online]. Available: http://dx.doi.org/10.1006/nimg.2001.0962

[6] G. Marin, C. Guerin, S. Baillet, L. Garnero, and G. Meunier, "Influence of skull anisotropy for the forward and inverse problem in eeg: simulation studies using fem on realistic head models." *Hum Brain Mapp*, vol. 6, no. 4, pp. 250–269, 1998.

[7] C. Ramon, P. Schimpf, and J. Haueisen, "Influence of head models on eeg simulations and inverse source localizations," *BioMedical Engineering OnLine*, 2006.

[8] R. V. Uitert, C. Johnson, and L. Zhukov, "Influence of head tissue conductivity in forward and inverse magnetoencephalographic simulations using realistic head models." *IEEE Trans Biomed Eng*, vol. 51, no. 12, pp. 2129–2137, Dec 2004. [Online]. Available: http://dx.doi.org/10.1109/TBME.2004.836490

[9] C. H. Wolters, A. Anwander, X. Tricoche, D. Weinstein, M. A. Koch, and R. S. MacLeod, "Influence of tissue conductivity anisotropy on eeg/meg field and return current computation in a realistic head model: a simulation and visualization study using high-resolution finite element modeling." *Neuroimage*, vol. 30, no. 3, pp. 813–826, Apr 2006. [Online]. Available: http://dx.doi.org/10.1016/j.neuroimage.2005.10.014

[10] Y. Yan, P. L. Nunez, and R. T. Hart, "Finite-element model of the human head: scalp potentials due to dipole sources," *Med. Biol. Eng. Comput.*, vol. 29, pp. 475–481, Sep. 1991.

[11] C. C. McIntyre and W. M. Grill, "Finite element analysis of the current-density and electric field generated by metal microelectrodes," *Ann. Biomed. Eng.*, vol. 29, no. 3, pp. 227–235, Mar. 2001.

[12] *SOLETRA system*, Medtronic, Minneapolis, MN, USA, http://www.medtronic.com/our-therapies/neurostimulators-movement-disorders/index.htm.

[13] S. Breit, J. B. Schulz, and A.-L. Benabid, "Deep brain stimulation." *Cell Tissue Res*, vol. 318, no. 1, pp. 275–288, Oct 2004. [Online]. Available: http://dx.doi.org/10.1007/s00441-004-0936-0

[14] C. R. Butson, C. B. Maks, and C. C. McIntyre, "Sources and effects of electrode impedance during deep brain stimulation." *Clin Neurophysiol*, vol. 117, no. 2, pp. 447–454, Feb 2006. [Online]. Available: http://dx.doi.org/10.1016/j.clinph.2005.10.007

[15] C. R. Butson and C. C. McIntyre, "Differences among implanted pulse generator waveforms cause variations in the neural response to deep brain stimulation." *Clin Neurophysiol*, vol. 118, no. 8, pp. 1889–1894, Aug 2007. [Online]. Available: http://dx.doi.org/10.1016/j.clinph.2007.05.061

[16] ——, "Role of electrode design on the volume of tissue activated during deep brain stimulation." *J Neural Eng*, vol. 3, no. 1, pp. 1–8, Mar 2006. [Online]. Available: http://dx.doi.org/10.1088/1741-2560/3/1/001

[17] ——, "Tissue and electrode capacitance reduce neural activation volumes during deep brain stimulation." *Clin Neurophysiol*, vol. 116, no. 10, pp. 2490–2500, Oct 2005. [Online]. Available: http://dx.doi.org/10.1016/j.clinph.2005.06.023

[18] S. Miocinovic, M. Parent, C. R. Butson, P. J. Hahn, G. S. Russo, J. L. Vitek, and C. C. McIntyre, "Computational analysis of subthalamic nucleus and lenticular fasciculus activation during therapeutic deep brain stimulation." *J Neurophysiol*, vol. 96, no. 3, pp. 1569–1580, Sep 2006. [Online]. Available: http://dx.doi.org/10.1152/jn.00305.2006

[19] M. Aström, J. D. Johansson, M. I. Hariz, O. Eriksson, and K. Wårdell, "The effect of cystic cavities on deep brain stimulation in the basal ganglia: a simulation-based study." *J Neural Eng*, vol. 3, no. 2, pp. 132–138, Jun 2006. [Online]. Available: http://dx.doi.org/10.1088/1741-2560/3/2/007

[20] X. F. Wei and W. M. Grill, "Current density distributions, field distributions and impedance analysis of segmented deep brain stimulation electrodes." *J Neural Eng*, vol. 2, no. 4, pp. 139–147, Dec 2005. [Online]. Available: http://dx.doi.org/10.1088/1741-2560/2/4/010

[21] N. Yousif, R. Bayford, P. G. Bain, and X. Liu, "The peri-electrode space is a significant element of the electrode-brain interface in deep brain stimulation: A computational study." *Brain Res Bull*, vol. 74, no. 5, pp. 361–368, Oct 2007. [Online]. Available: http://dx.doi.org/10.1016/j.brainresbull.2007.07.007

[22] C. R. Butson, S. E. Cooper, J. M. Henderson, and C. C. McIntyre, "Predicting the effects of deep brain stimulation with diffusion tensor based electric field models." *Med Image Comput Comput Assist Interv Int Conf Med Image Comput Comput Assist Interv*, vol. 9, no. Pt 2, pp. 429–437, 2006.

[23] C. C. McIntyre, S. Mori, D. L. Sherman, N. V. Thakor, and J. L. Vitek, "Electric field and stimulating influence generated by deep brain stimulation of the subthalamic nucleus." *Clin Neurophysiol*, vol. 115, no. 3, pp. 589–595, Mar 2004. [Online]. Available: http://dx.doi.org/10.1016/j.clinph.2003.10.033

[24] S. Sotiropoulos and P. Steinmetz, "Assessing the direct effects of deep brain stimulation using embedded axon models," *Journal of Neural Engineering*, vol. 4, no. 2, pp. 107–119, 2007. [Online]. Available: http://stacks.iop.org/1741-2552/4/107

[25] C. R. Butson, S. E. Cooper, J. M. Henderson, and C. C. McIntyre, "Patient-specific analysis of the volume of tissue activated during deep brain stimulation." *Neuroimage*, vol. 34, no. 2, pp. 661–670, Jan 2007. [Online]. Available: http://dx.doi.org/10.1016/j.neuroimage.2006.09.034

[26] H. C. Burger and van Dongen, "Specific electric resistance of body tissues." *Phys Med Biol*, vol. 5, pp. 431–447, Apr 1961.

[27] S. Rush, J. A. Abildskov, and McFee, "Resistivity of body tissues at low frequencies." *Circ Res*, vol. 12, pp. 40–50, Jan 1963.

[28] P. W. Nicholson, "Specific impedance of cerebral white matter." *Exp Neurol*, vol. 13, no. 4, pp. 386–401, Dec 1965.

[29] L. Geddes and L. Baker, "The specific resitstance of biological materials - a compendium of data for the biomedical engineer and physiologist," *Med. Bio. Eng*, 1967.

[30] K. R. Foster and H. P. Schwan, "Dielectric properties of tissues and biological materials: a critical review." *Crit Rev Biomed Eng*, vol. 17, no. 1, pp. 25–104, 1989.

[31] S. Gabriel, R. W. Lau, and C. Gabriel, "The dielectric properties of biological tissues: Ii. measurements in the frequency range 10 hz to 20 ghz." *Phys Med Biol*, vol. 41, no. 11, pp. 2251–2269, Nov 1996.

[32] F. Rattay, "Analysis of models for external stimulation of axons," *IEEE Trans Biomed Eng*, 1986.

[33] D. Güllmar, J. Haueisen, M. Eiselt, F. Giessler, L. Flemming, A. Anwander, T. R. Knösche, C. H. Wolters, M. Dümpelmann, D. S. Tuch, and J. R. Reichenbach, "Influence of anisotropic conductivity on eeg source reconstruction: investigations in a rabbit model." *IEEE Trans Biomed Eng*, vol. 53, no. 9, pp. 1841–1850, Sep 2006. [Online]. Available: http://dx.doi.org/10.1109/TBME.2006.876641

[34] S. Kim, T.-S. Kim, Y. Zhou, and M. Singh, "Influence of conductivity tensors in the finite element model of the head on the forward solution of eeg," in *Nuclear Science Symposium Conference Record, 2001 IEEE*, vol. 4, 4-10 Nov. 2001, pp. 1892–1896.

[35] Y. Wang, D. R. Haynor, and Y. Kim, "An investigation of the importance of myocardial anisotropy in finite-element modeling of the heart: methodology and application to the estimation of defibrillation efficacy." *IEEE Trans Biomed Eng*, vol. 48, no. 12, pp. 1377–1389, Dec 2001.

[36] *COMSOL Multiphysics*, COMSOL AB., Sweden.

[37] C. R. Butson and C. C. McIntyre, "Current steering to control the volume of tissue activated during deep brain stimulation," *Brain Stimulation*, vol. 1, no. 1, pp. 7–15, 2008. [Online]. Available: www.scopus.com

[38] C. C. McIntyre, S. Miocinovic, and C. R. Butson, "Computational analysis of deep brain stimulation." *Expert Rev Med Devices*, vol. 4, no. 5, pp. 615–622, Sep 2007. [Online]. Available: http://dx.doi.org/10.1586/17434440.4.5.615

5 Interaction between neurons and electric field

The finite element (FE) model presented in the previous chapter is able to solve the Poisson equation for a biological environment extending to the chest. Therefore, the prediction of the potentials generated by the deep brain stimulation (DBS) can be immediately done. But while this knowledge is valuable from a physical point of view, it does not reveal the neurological action leading to the improvements of the symptoms observed clinically.
In this chapter, the action of the stimulation on the tissues surrounding the electrode is investigated. In the first section, the general electrical model of a neuron is introduced, and the action of electrical stimulation is explained. The second section introduces the specific model of axons used in this thesis to evaluate the volume of activated tissues. Finally the last section presents the central results obtained in this thesis, predicting the volume of tissue activated by the electrical stimulation in different configurations.

5.1 Neural signal propagation and general electrical model of a neuron

This section provides a general description of neurons and introduces the biological mechanisms of neural signal propagation. The electrical models of neurons are then developed, and the definition of the activation function is provided.

5.1.1 Neuron description and signal propagation in axons

Neurons are the responsible cells for the generation and transmission of information in living bodies. The typical structure of a neuron is shown in Fig. 5.1. According to the task it is dedicated a neuron can show several morphologies.
A succinct description of the neuron morphology as follow [1]:

- the soma, which is the central part of the neuron. It contains the nucleus of the cell. The nucleus ranges from 3 to 18 μm in diameter.
- the dendrites are cellular extensions with many branches. The majority of input signals arriving to the neuron enter through this part of the neuron.
- the axon is a cable-like projection which transmits the neural signal away from the soma. Its length varies from ten to ten thousand times the diameter of the soma. An axon can be covered with an insulating sheath of myelin, which allows a more rapid transmission of signal. These sheaths frequently happen a s discontinuous sections. The space between two sections of myelin sheath is called a node of Ranvier (see Fig. 5.1).
- the axon terminal contains synapses, specialized structures where neurotransmitter chemicals are released in order to communicate with the dendrites of other neurons.

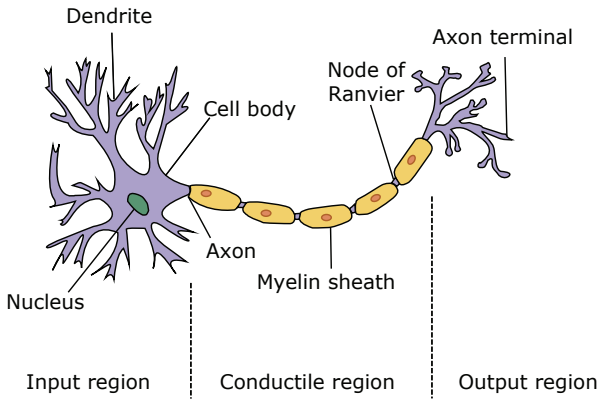

Figure 5.1: Typical structure of a neuron. The cell body is called soma. It is surrounded by dendrites which are the receptors of signals from other neurons. The signal propagates through the axon to the axon terminals, which are connected to the dentrites of other neurons. After [1]

The transmission of signal takes place through electrochemical processes along the fiber. The cell membrane of the axon and soma contains voltage-gated ion channels which allows the neuron to generate and propagate an electrical signal. These signals are generated and propagated by charge-carrying ions including sodium (Na^+), potassium (K^+), chloride (Cl^-), and calcium (Ca^{2+}). The unidirectional signal transmission from one neuron to the other is made through synapses, specialized structures allowing communication between two neurons where neurotransmitter chemicals are released. The conduction of nerve impulses is an example of an all-or-none response. In other words, either a neuron stays unactivated or responds completely to stimulation. In that case, an action potential propagates along the axon to the axon terminals.
There are several stimuli that can activate a neuron amd lead to electrical activity, including pressure, stretch, chemical transmitters, and changes of the electric potential across the cell membrane. Stimuli cause specific ion-channels within the cell membrane to open. This leads to a flow of ions through the cell membrane. The result is a change in the "**transmembrane potential**" defined as the potential difference or voltage existing between the intracellular and extracellular regions at both sides of the cell's membrane. The time-evolution of this transmembrane potential during a neuronal signal transmission is called the "**action potential**".

The time evolution of the action potential can be divided into five parts (see Fig. 5.2):

- resting state: Prior to the signal activation, as the intracellular and extracellular ions concentrations are not equal, there is a non-zero value for the transmembrane potential, called the resting potential.
- depolarization: As the membrane potential is increased, both the sodium and potassium ion channels begin to open up. This increases both the inward sodium current and the balancing outward potassium current. For small voltage increases, the potassium current triumphs over the sodium current and the voltage returns to its normal resting value. However, if the voltage increases past a critical threshold, the sodium current dominates. This results in a runaway condition whereby the positive feedback from the sodium current activates even more sodium channels. Thus, the cell "fires", producing an action potential.
- repolarization: At the peak of the action potential, the sodium channels become inactivated. At

the same time, the raised voltage opens voltage-sensitive potassium channels. Combined, these changes in sodium and potassium permeability cause the membrane potential to drop quickly.

- hyperpolarization: The raised voltage opened many more potassium channels than usual, and these do not close right away when the membrane returns to its normal resting voltage. Hence, there is an undershoot, called hyperpolarization, that persists until the membrane potassium permeability returns to its usual value.
- refractory period: The opening and closing of the sodium and potassium channels during an action potential may leave some of them in a "refractory" state, in which they are unable to open again until they have recovered. In the absolute refractory period, so many ion channels are refractory that no new action potential can be fired. In the relative refractory period, enough channels have recovered that an action potential can be provoked, but only with a stimulus much stronger than usual. These refractory periods ensure that the action potential travels in only one direction along the axon.

More details on the description of the neurons and of the bioelectrochemical mechanisms of signal propagation can be found in [1].

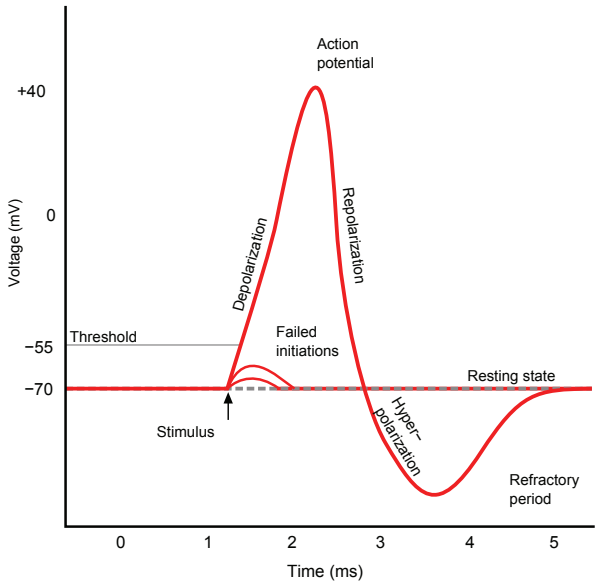

Figure 5.2: Idealized time course of an action potential. The difference between the outer and the inner potential is called the membrane potential. This membrane potentials is varying while the signal is transmitted along the axon.

5.1.2 Electrical equivalent models of a neuron

The first electrical stimulation of nerves and muscles dates from Galvani's experiment (see Chapter 2). Nevertheless, the understanding of what really happens when a nerve is electrically excited was not possible prior to the knowledge of the behavior of the membrane surrounding the nerve fiber.
The breakthrough in understanding the propagation process has come with the description of membrane behavior by a system of four differential equations which are known as the Hodgkin-Huxley equations [2]. This mechanism has been understood thanks to experiments on giant squids axons.

Their extremely large axon diameters, up to 1 mm, allow the insertion of microelectrodes.
The electrical properties of a biological membrane depend essentially on the types and amount of ionic channels. In 1964, as technical progress allowed the measurements of myelinated frog axons (which have diameters of some μm only), Frankenhaeuser and Huxley published their equations which seemed more appropriate for mammalian and human applications [3].
The Hodgkin-Huxley equations, as well as the Frankenhaeuser-Huxley (FH) equations quantifies the voltage current relations of a piece of membrane in the time dimension. They essentially deal with the transmembrane potential V_m (difference of potential between the inner (V_i) and the outer (V_o) potential)
The behavior of such a patch of membrane, can be simulated by an electrical equivalent circuit consisting of a voltage source, capacity and nonlinear resistance (see Fig. 5.3). More information on the description of the equation driving the resistance of the membrane can be found in [4].

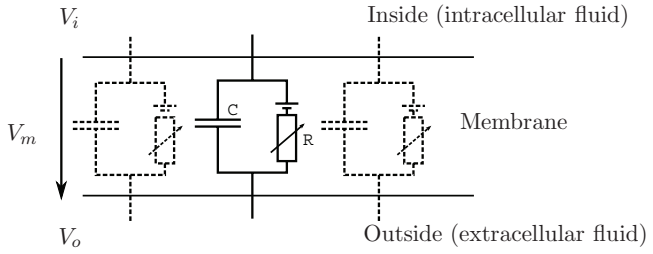

Figure 5.3: Electrical equivalent circuit for a patch of membrane. The voltage source represents the potential difference of the membrane due to the different ionic concentrations. The membrane resistance is highly nonlinear because of the activity of the ionic channels embedded in the membrane.

An action potential propagates like a wave phenomena, because during repolarization it generates local currents that tend to depolarize the membrane immediately adjacent to the action potential. When that depolarization caused by the local currents reaches a threshold, a new action potential is produced adjacent to the original one. Action potential propagation is unidirectional (no backward propagation) because the recently depolarized area of the membrane is in absolute refractory period and cannot generate an action potential.
A similar effect can be reached artificially by changing the membrane voltage via the extracellular potential. This is the aim of extracellular electrical stimulation.

5.1.3 Electrical equivalent models of the excitation of a myelinated fiber

The simplest example of nerve stimulation consists of a punctual current source of amplitude I_a placed near an uniform myelinated axon (see Fig. 5.4). Both the source and the fiber are considered to lie in an uniform conducting medium of unlimited extent. This model has been investigated in [5].
The electric model corresponding to Fig. 5.4 is described in Fig. 5.5. In this electric model, it is assumed that the transmembrane current is confined solely in to the nodal region. Since the node is relatively narrow, the network representing the membrane is essentially described by lumped elements. These are shown as a parallel RC-structure at all the nodes except the central one (node 0). Only the central node is described by the FH equations, as it is here that the stimulation arises [5].

The axial intracellular current path introduces the axial intracellular resistance per internodal length R_i, in [Ω], that can be obtain according to equation (4.1). In this case, the involved surface is a circular

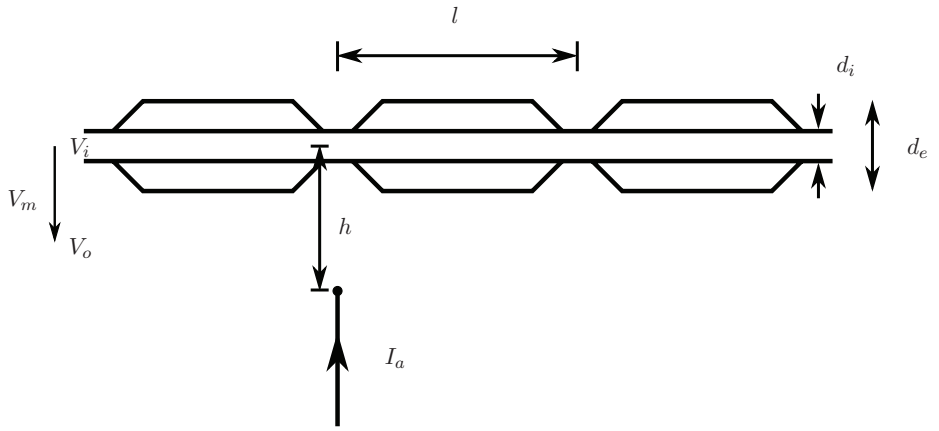

Figure 5.4: Example of myelinated fiber stimulation. A punctual current stimulus, I_a, lies at a distance h form a single myelinated fiber. A node of Ranvier is assumed to be aligned with the stimulating monopole. The internodal distance l is related to the outer diameter of the myelin, d_e where $l = 100d_e$. The axon diameter is d_i.

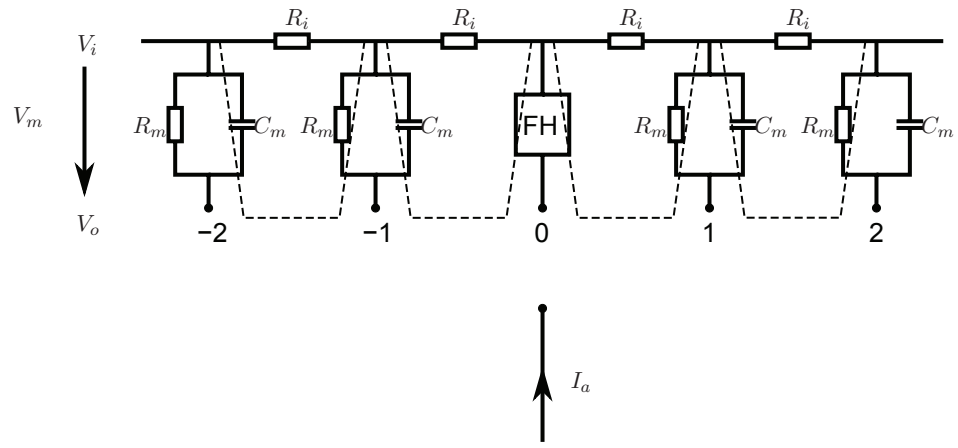

Figure 5.5: Electrical equivalent model of a myelinated fiber stimulation. The fiber is stimulated by a point current source of strength I_a. The node directly beneath the source is labeled 0 and its membrane is modeled by Frankenhaeuser-Huxley (FH) equations. Lateral nodes are assumed to be at resting state and represented by parallel resistance and capacitance (where R_m, C_m are the total nodal lumped resistance and capacitance, respectively, per nodal area). The total intracellular internodal resistance is R_i. The hatched lines represent the internodal myelin sheaths.

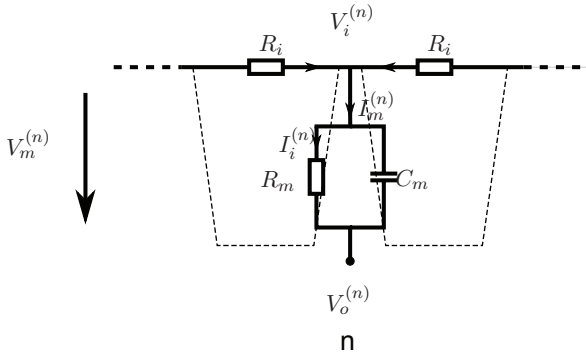

Figure 5.6: Generic n^{th} node.

section of diameter d_i. Therefore :

$$R_i = \frac{1}{\sigma_i} \frac{l}{\pi (d_i/2)^2} = \frac{4l}{\sigma_i \pi d_i^2} \tag{5.1}$$

with σ_i the intracellular conductivity, in $[\Omega \cdot m]^{-1}$; l the internodal length, in $[m]$ and d_i the axon diameter (internal myelin diameter), in $[m]$.
McNeal assumed that the potential on the extracellular side of the nodal membrane was fixed by the stimulating field. Since the latter is a point source (*i.e.* a monopole), the associate resistance is a radial one, computed again as in equation (4.1) but using as surface a sphere of radius r :

$$R = \frac{1}{\sigma_o} \frac{r}{4\pi r^2} \tag{5.2}$$

and therefore, the applied stimulating potential V_o, in $[V]$, is

$$V_o = I_a R = \frac{I_a}{4\pi \sigma_0 r} \tag{5.3}$$

with I_a the applied current, in $[A]$; σ_0 the extracellular conductivity of the medium, in $[\Omega \cdot m]^{-1}$ and r the distance from any node to the point source, in $[m]$.
This formulation considers that the field is obtained for an infinite homogeneous medium. The influence of the axon structure and of the action potential on the field are thus neglected.

On the basis of the equivalent electric circuit for a n^{th} node described in Fig. 5.5 and the applied field of Equation (5.3), one can determine the response to step currents of varying strengths (up to that required for excitation at node 0).
The Fig. 5.6 shows a generic $n^{th} \neq 0$ element in the axon. According to Kirchhoff laws, the transmembrane current $I_m^{(n)}$ can be obtained as

$$I_m^{(n)} = \frac{V_i^{(n-1)} - V_i^{(n)}}{R_i} + \frac{V_i^{(n+1)} - V_i^{(n)}}{R_i} \tag{5.4}$$

where $V_m^{(n)}$ is the transmembrane voltage at the n^{th} node and R_i the axial intracellular resistance per internodal length. This current can be separated into two terms, going through the nodal capacitance

C_m and resistance R_m, as

$$I_m^{(n)} = C_m \frac{dV_m^{(n)}}{dt} + I_i^{(n)} \tag{5.5}$$

where

$$I_i^{(n)} = \frac{V_m^{(n)}}{R_m} \tag{5.6}$$

is the so called "**ionic current**".
Combining equations (5.4) and (5.5) and using the definition in equation (5.6) an the definition of the transmembrane voltage $V_m^{(n)} = V_i^{(n)} - V_o^{(n)}$ gives

$$\frac{dV_m^{(n)}}{dt} = \frac{1}{C_m}\left[\frac{1}{R_i}(V_m^{(n-1)} - 2V_m^{(n)} + V_m^{(n+1)} + V_o^{(n-1)} - 2V_o^{(n)} + V_o^{(n+1)}) - I_i^{(n)}\right]. \tag{5.7}$$

However this development is only valid for $n \neq 0$ (subthreshold conditions). For the activated node, the ionic current $I_i^{(n)}$ is in fact given by the Frankenhaeuser-Huxley equations and has a much more complicated expression being done by

$$I_i^{(0)} = \pi d_i \nu (i_{Na} + i_K + i_P + i_L) \tag{5.8}$$

where ν is the nodal width.
Then for $n = 0$ equation (5.7) must be replaced by

$$\frac{dV_m^{(0)}}{dt} = \frac{1}{C_m}\left[\frac{1}{R_i}(V_m^{(-1)} - 2V_m^{(0)} + V_m^{(1)} + V_o^{(-1)} - 2V_o^{(0)} + V_o^{(1)}) - I_i^{(0)}\right]. \tag{5.9}$$

Additional mathematical aspects of these equations can be found in [1].

5.1.4 Electrical models of the excitation of an unmyelinated fiber

The response of a single unmyelinated fiber of diameter d to a stimulating field can be found through the same type of simulation described for the myelinated fiber. In fact, to obtain numerical solutions it is necessary to discretize the axial coordinate (x) into elements Δx and a network somewhat similar to that considered in Fig. 5.5 results. One obtains an expression similar to the equation (5.7) for the transmembrane current at the n^{th} element:

$$\frac{dV_m^{(n)}}{dt} = \frac{1}{C_m}\left[\frac{1}{r_i \Delta x}(V_m^{(n-1)} - 2V_m^{(n)} + V_m^{(n+1)} + V_o^{(n-1)} - 2V_o^{(n)} + V_o^{(n+1)}) - \pi\, d\, \Delta x\, i_{\text{ionic}}\right] \tag{5.10}$$

where

$$r_i = \frac{4}{\sigma_i \pi d^2}, \tag{5.11}$$

with σ_i being the conductivity of the axon. Introducing the capacitance per cm^2 c_m and the geometrical relationship:

$$C_m = \pi\, d\, \Delta\, x\, c_m \tag{5.12}$$

leads to

$$\frac{dV_m^{(n)}}{dt} = \frac{1}{c_m}\left[\frac{1}{r_i d\pi}\left(\frac{V_m^{(n-1)} - 2V_m^{(n)} + V_m^{(n+1)}}{\Delta x^2} + \frac{V_o^{(n-1)} - 2V_o^{(n)} + V_o^{(n+1)}}{\Delta x^2}\right) - i_{\text{ionic}}\right]. \tag{5.13}$$

For $\Delta x \to 0$ we obtain

$$\frac{dV_m^{(n)}}{dt} = \frac{1}{c_m}\left[\frac{1}{r_i d\pi}\left(\frac{\partial^2 V_m}{\partial x^2} + \frac{\partial^2 V_o}{\partial x^2}\right) - i_{ionic}\right]. \tag{5.14}$$

In the above formula, the only term including the extracellular influence is the second derivative of V_o. **Therefore, the stimulating influence of the extracellular potential in a fiber is given by**

$$f = \frac{\partial^2 V_o}{\partial x^2}. \tag{5.15}$$

This function f has been named "activating function" by Rattay [6].
The activation takes place when $\partial V_m^{(n)}/\partial t > 0$, namely when there is a depolarization of the membrane (see Fig. 5.2). But according to equation (5.14), the sign of $\partial V_m^{(n)}/\partial t$ will depend on the amplitude of a positive term (which includes f as main part) which must counterbalance the existing negative ionic current i_{ionic}. Therefore, when f exceeds a given threshold which depends on several parameters such as the properties of the fiber and the initial conditions, the stimulation takes place. Fig. 5.7 shows the potential distribution V_o generated by a positive punctual current source as obtained form Equation (5.3). The red curve shows the activation function for a negative current (cathodic stimulation) and the blue for a positive current (anodic stimulation). It is easy to show that the activation function reach higher value when using cathodic stimulation rather than anodic stimulation. Therefore cathodic stimulation is preferred as the threshold is reached using a lower current than with anodic stimulation.
When the value of cathodic current is increased, the negative lobes located on each side of the maximum peaks create a lateral hyperpolarization to the active region that blocks the emerging propagating pulse. More investigations on this behavior can be found in [4].

5.2 Coupling of an axon model with extracellular potentials

The activation of neuron by extracellular stimulation is linked to the second spatial difference of the extracellular potential applied along the fiber. Several studies have used the activating function f (see Equation (5.15)) in computer models to predict the volume of tissues activated by a stimulation [7–9]. But the generation of an action potential arise when f exceeds a certain threshold, depending on several parameters such as the structure of the neuron. Therefore the use of multi-compartment models coupled with the electric potential field generated by the stimulation provides a more accurate prediction of activated neurons [10, 11].

5.2.1 Description of the axon model

During extracellular stimulation, the action potential initiation occurs in the axon [12–14] rather than in the soma of the neuron. Therefore the model used to predict the action potential generation by DBS is a thalamocortical axon. The axon model is based on the McIntyre model, proposed in [15]. This model has been reused in most of the studies on DBS [16–27].
This model consists of a multi-compartment double cable of a mammalian axon. The 21 nodes of Ranvier are explicitly represented, as well as the 20 paranodal and internodal section of the axons and a finite impedance myelin sheath. The double cable represents the axon membrane and the myelinated sheath. Each segment between two nodes of Ranvier has a length of 0.5 mm and is composed of two myelin attachment segments (MYSA), two paranode segments (FLUT) and six internodes segments

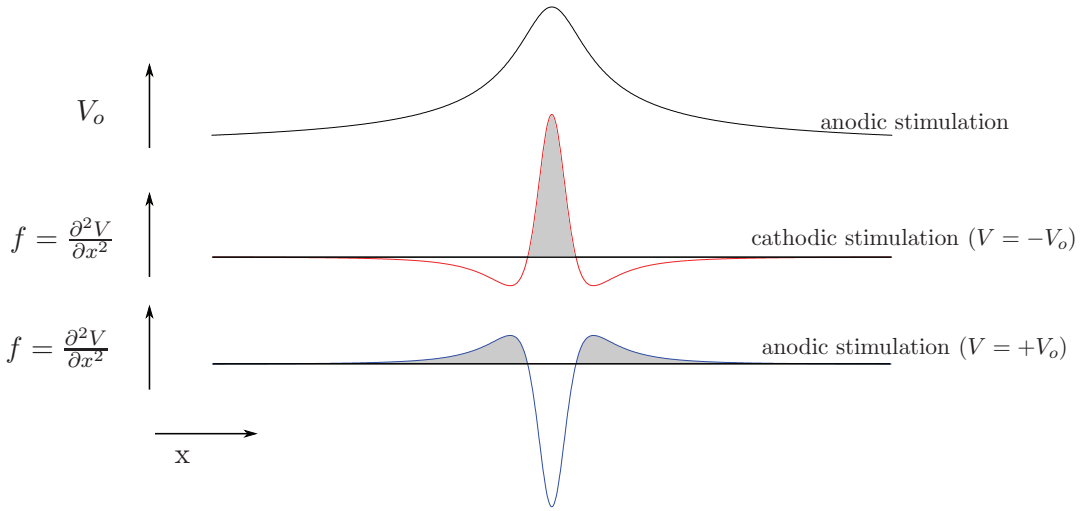

Figure 5.7: Extracellular stimulation of a fiber. The upper curve shows the extracellular potentials generated by a positive current point source (anodic stimulation). The middle curve shows the activation function f for an cathodic stimulation (negative current) and the lower curve shows f an anodic stimulation. The activation happens when f is over a certain threshold, depending of the fiber properties. The cathodic stimulation is much more effective than the anodic stimulation.

(STIN). Fig. 5.8 shows the geometry of the axon model.

Each segment of the axon model has its own membrane dynamics (see Fig. 5.9):

- the node of Ranvier is a combination of nonlinear fast Na^+, persistent Na^+ and slow K^+ conductance, a linear leakage conductance and the membrane capacitance.
- the internodal segments are made of a double cable structure. The myelin sheath and the axon membrane are represented by a linear conductance in parallel with the membrane capacitance. The MYSA, FLUT and STIN segments have their own conductance and capacitance.

Fig. 5.8 shows the geometry of the axon model. The values of the electrical properties of the membrane and ionic sources can be found in Table 2 of [15].

The electrical model of the axon is implemented with the help of the NEURON simulation environment [28]. In [15], several model geometric parameters are proposed, based on the diameter of the fiber. The excitability of axons is reduced as their diameters decrease [29]. Therefore the choice of the smallest diameter (5,7 μm) is assumed. The other dimensions of the axon model can be found in Table 1 of [15].

5.2.2 Determination of the extracellular potentials generated by the stimulation

The potential V_o applied as extracellular potential to the electrical model of axon are extracted from the FE model.

A time varying field of potential is created convoluting the normalized potentials by an time varying electric pulse of amplitude U_{pulse} and width P_w. The pulse amplitude and width can be adjusted to

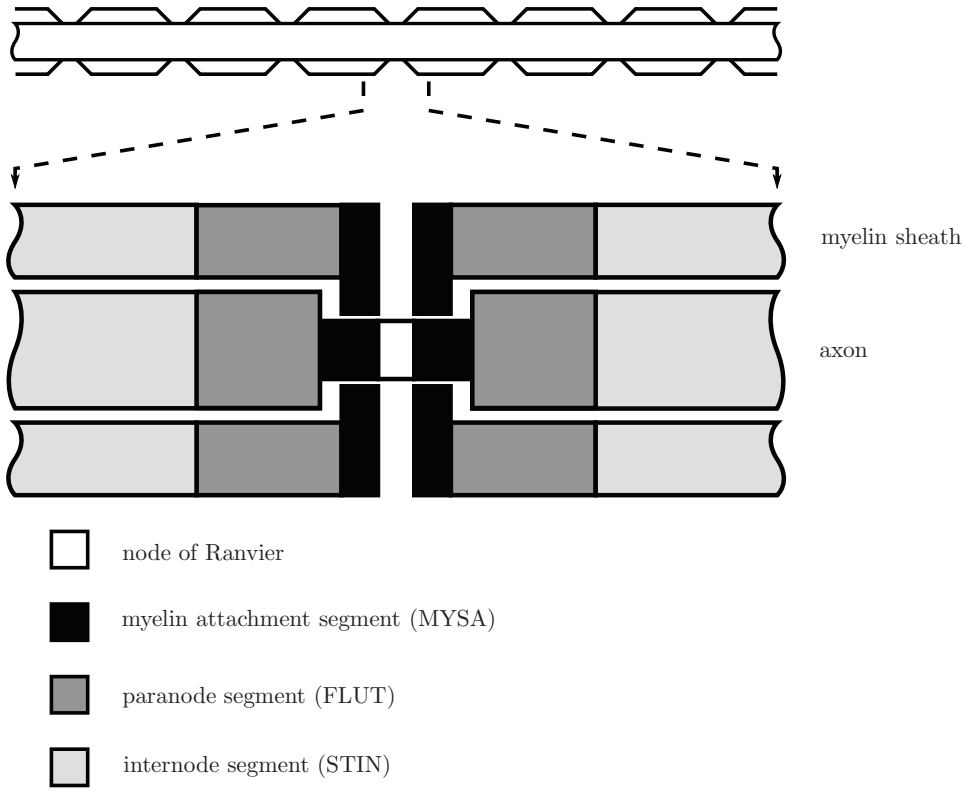

Figure 5.8: The model of axon used to evaluate the generation of action potential by the stimulation is a multi-compartment double cable model of myelinated axon, taken from [15]. This axon is composed of 21 nodes and 20 internodes. Each internode has a length of 0.5 mm and is decomposed into 2 myelin attachment segments (MYSA), 2 paranode segments (FLUT) and 6 internode segments (STIN), having different electrical properties.

correspond to clinically used electric pulses.

The time varying extracellular potentials $V_o(t)$ are then set to each NEURON discretized node of the axon model. When the location of the discretized nodes did not match a FE node, a linear interpolation of the electric potential value of the adjacent nodes is made.

5.2.3 Choice of the axons' direction

The generation of an action potential in an axon is linked to the activation function f, defined as the second spatial difference of the extracellular potential along the axon process. Therefore the chosen direction of the axon plays an important role on the determination of the generation of an action potential.

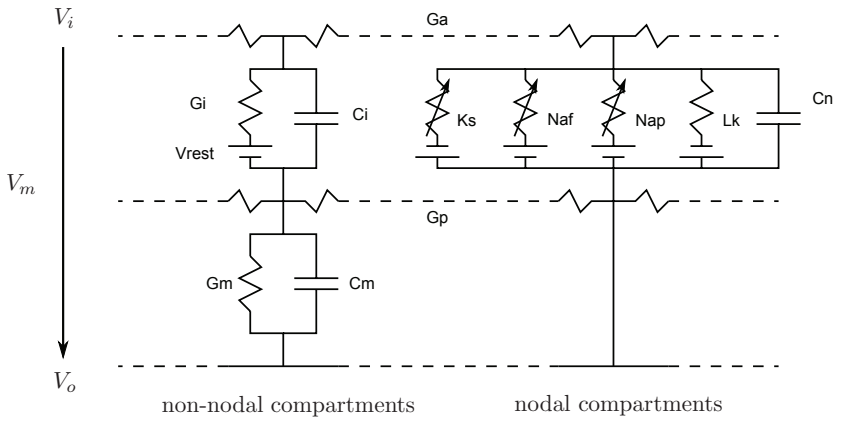

Figure 5.9: Electrical equivalent of the model of axon. The nodal segment is composed of a fast Na^+ (Naf), persistent Na^+ (Nap) and slow K^+ (Ks) conductance, a linear leakage conductance (Lk) and the membrane capacitance (Cn). The internodal segments are made of a double cable structure of linear conductance with an explicit representation of the myelin sheath (Gm in parallel with Cm) and the internodal axon membrane (Gi in parallel with Ci). Gp and Ga represent the axial resistance of the periaxonal space and the axon. Taken from [15].

Pre-determined direction of axons

Many studies have evaluated the extend of the stimulation using axon models perpendicular to the electrode shaft coupled to a two dimensional FE model, as shown in Fig. 5.10(a) [18–20, 30]. These studies have shown that the activation threshold is dependent not only on the fibers topology but also to is distance from the stimulation electrode. They also provided the first predictions of the volume of tissue activated (VTA). This approach to evaluate the spatial activation of axons is satisfying when using axisymmetric or homogeneous FE models. Indeed, the results provide a two dimensional image of the area where action potential arise. Subsequently, a rotation of the obtained results provide a volume of tissue activated (VTA).

When the FE model is fully 3D and uses inhomogeneous or anisotropic conductivities, the potential distribution is not axisymmetric anymore (see Section 4.3.1). In these cases, techniques assuming axons always perpendicular to the rotation plane will miss the real situation and will produce only partially valid results. A three dimensional evaluation of the VTA cannot be accurately made by using axons models perpendicular to only one plane. Indeed, according to this plane direction, the potential distribution along the axons varies. To overcome this issue, the McIntyre's group has proposed another method to evaluate the VTA, based on the evaluation of the activation threshold for f. The VTA has then been obtained through the computation of f in an anisotropic and inhomogeneous three dimensional model. But choices for the direction chosen to compute f has not been clearly explained in the publications [16, 17, 27].

A new technique is proposed here to evaluate the VTA generated by the DBS. Axons model are placed regularly in the three dimensional space around the stimulation electrode. Therefore the inhomogeneities of the potential field introduced by the anisotropic conductivity are directly taken into account. The direction of the axons is forced to be perpendicular to several planes containing the electrode shaft, as proposed in the two dimension case(see Fig. 5.10(b)). Therefore,

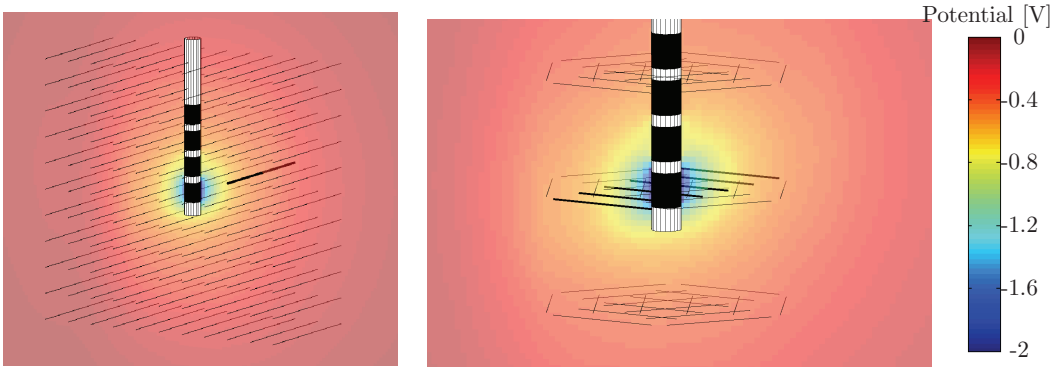

(a) Axon disposition for homogeneous models

(b) Axon disposition for inhomogeneous models

Figure 5.10: Models of axons having pre-determined direction. a) In previous studies, several models of axon having their direction perpendicular to the same plane are used. The volume of tissue activated is then obtained using a rotation of the responses obtained for one plane. b) When using inhomogeneous and anisotropic conductivity, the use of axons having their direction tangential to the electrode shaft is necessary, as the potential distribution does not have a regular shape. To improve the clearness of the figure, less axons are represented. In both cases, the extracellular potentials of the axon models are coupled to the potential field obtained from the FE model. In that case, the pulse amplitude U_{pulse} is set to -2 V.

the space is described by axons tangential to the electrode shaft. As the central nodes are the most proximal to the stimulation electrode, the action potential is likely to arise at this position. Therefore, the determination of activation at one point is given by the activation of the axon model centered at this point and tangential to the electrode shaft. The evaluation of the VTA is then obtained with a spatial integration of the responses of the axons to stimulation for all the central points.

Anatomically based direction of axons

Another method to evaluate the tissue activation is to set the direction of the axon models according to a realistic fiber direction.
The direction of the rectilinear axon models as well as the tissue anisotropy have been set according to the anatomical knowledge in the model used by Sotiropoulos and Steinmetz in [26].
Yet, an alternative technique is used in [25]. This study has focused on the effect of stimulation on a particular class of neurons, the STN projection neurons. Models using the non-rectilinear real geometry of neurons have been generated and combined with the results of a FE model of the DBS electrode and electric field transmitted to the tissue medium.

In this thesis a new method is developed to use the information of the DT-MRI to orient the models of axons. When a DT-MRI voxel shows a fractional anisotropy (see equation (3.19)) over 0.25, the axons having their central nodes in that vortex are aligned according to the main eigenvector of the anisotropic tensor. When the fractional anisotropy of a voxel is below that threshold, no axon models are used for that voxel. Fig. 5.11 shows the obtained models for a coronal cutting view.
With axon models having their direction based on DT-MRI, the most proximal nodes to the stimulation

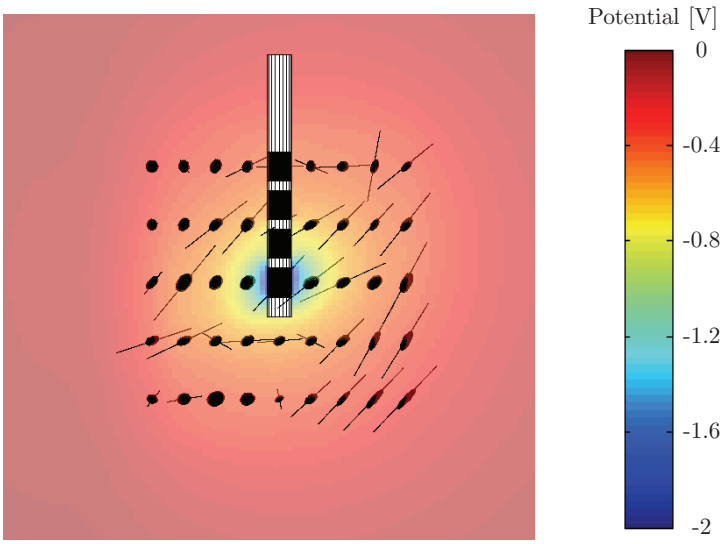

Figure 5.11: Cutting view showing the models of axons having their orientation based on DT-MRI. The conductivity tensor ellipsoids are shown in black. When the fractional anisotropy of a voxel is over 0.25, the axons models having their central nodes in that voxel share the same direction that the conductivity tensor's main eigenvector. When the fractional anisotropy is below 0.25, no axon models are used for that voxel. All the axons model have the same length, the projection introduces some differences. The extracellular potentials of axon models is coupled to the potential field obtained from the FE model. In that case, the pulse amplitude U_{pulse} is set to -2 V.

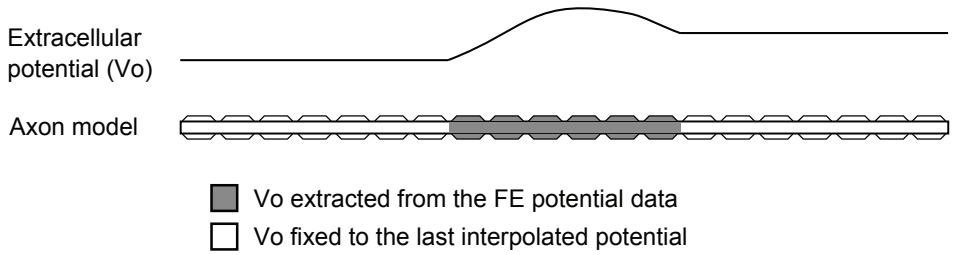

Figure 5.12: Extracellular potential V_o of the axons models having their direction based on the DT-MRI. To avoid a firing of the axon ends, only the 7 central nodes and 6 central internodal segments have their extracellular potentials extracted from the FE potential data. The other extracellular potentials are set to the last interpolated value to have a continuity of potential.

electrode are not necessary at the center of the axon models. Therefore, determination of the action activation at one point can be ambiguous. Moreover, it has been shown that the axon's ends have a larger sensitivity to extracellular stimulation. To avoid that problem, only the extracellular potential of the seven central nodes and of the six internodes are set to the values obtained from the FE method. The other extracellular potentials are set to the value of the last interpolated node, to maintain the potential continuity as proposed in [26]. Fig. 5.12 shows the extrapotential applied to these axon models. A spatial integration of the responses of the axons to stimulation for all the central points provides the evaluation of the VTA.

The spatial extents of stimulation is evaluated for a three dimensional space around the stimulation electrode. The evaluation for a point of the space is made through the response of an axon model to the extracellular potentials generated by the stimulation. The axon models are set according to the two originals methods proposed in this section.
In the following section, the influence of several parameters on the VTA will be investigated with the help of the two techniques described just before:

- Using axon models perpendicular to the electrode shaft
- Setting the axons according to the fiber direction provided by DT-MRI.

5.3 Evaluation of the volume of tissue activated by the deep brain stimulation

This section evaluates the influence of several parameters on the activation of tissue by the DBS. First, the used procedure is described. Then, the evaluation of the influence of several parameters such as the pulse amplitude, the tissue conductivity and the applied boundary conditions is performed.

5.3.1 Procedure used to evaluate the activation of neuron models

The main steps for the evaluation of the volume of tissue activated are shown in Fig. 5.13. The potentials obtained from the FE model are used as input for the extracellular potentials of axon models. The response of these axon models to the extracellular stimulation is evaluated with the help of the NEURON environment tool [28]. Each point is said to be activated when the corresponding axon model is the place where an action potential arises. To detect if an action potential arises, a

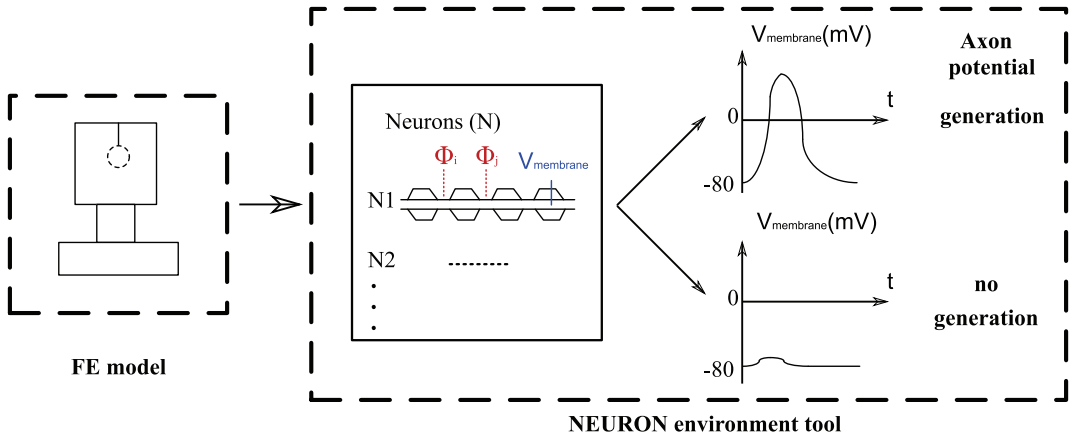

Figure 5.13: Steps to predict the axon activation. The potential obtained with the FE model are interpolated at the nodes of axon model. The NEURON environment tool [28] is then used to evaluate the response of axon models to stimulation. If an action potential is generated, the axon is considered as activated by the stimulation.

simple threshold filter is applied on the time variation of the membrane potential V_m.

The volumes of tissues activated are then computed by estimating the volume spanned by the active axons with a simplified three dimensional integration procedure. Both techniques used to determine the orientation of the axons are considered, thus leading to two series of results that can be compared. The equivalent radius of the VTA obtained with tangential models of axons can also be defined as

$$r_{\text{eq}} = \sqrt[3]{\frac{3 \cdot \text{VTA}}{4\pi}} \tag{5.16}$$

for monopolar stimulation,

$$r_{\text{eq}} = \sqrt[3]{\frac{3 \cdot \frac{\text{VTA}}{2}}{4\pi}} \tag{5.17}$$

for bipolar stimulation. Due to their irregular shape, defining an equivalent radius of the VTA obtained with axons direction based on DT-MRI is inappropriate.

5.3.2 Influence of the pulse amplitude

Fig. 5.14 shows four coronal cutting views of the response of tangential axon models to different stimulation amplitudes. The boundary condition used for these models is the most realistic one (BC I, see Section 4.3.3).

The two VTA obtained using either tangential or DT-MRI based directions for axons are shown in Fig. 5.15, for a pulse amplitude of -2V and the same BC applied.

Both the cutting views and the computed VTA with tangential directions show good agreements with the results obtained in previous modeling studies [8, 16, 18–20, 26, 27, 30]. The VTA obtained with axon direction based on the DT-MRI is very irregular. This is due to mainly two reasons: the discontinuities in the axons direction when changing from a voxel to another one and the fact that when a voxel shows a low anisotropy, no axon models are used. As this technique has not been used so far, no comparison with previous studies can be done.

Table 5.1: Influence of the pulse amplitude on the VTA [mm^3] for monopolar stimulation

U_{pulse} [V]	VTA with tangential direction of axons [mm^3]	r_{eq} [mm]	VTA with direction of axons based on DT-MRI [mm^3]
-0.5	24	1.79	19
-1	67	2.52	47
-2	165	3.40	208
-3	409	4.60	505

Nevertheless, both approaches show the same trends. As the pulse amplitude increases, the number of axons activated by the stimulation increases. This result is in accordance with clinical observations, as increasing the pulse amplitude leads to an extension of the stimulation effect. Table 5.1 shows the computed VTA using tangential and DT-MRI based directions for axon models in function of the pulse amplitude. With both approach the volumes increase with the pulse amplitude.

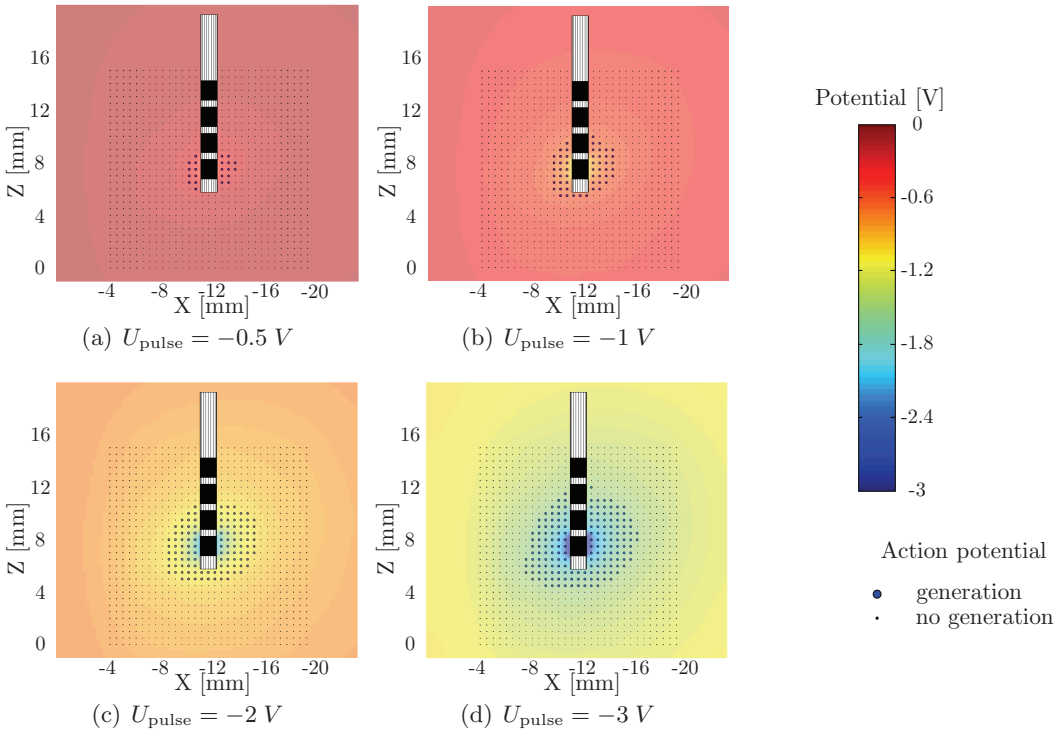

(a) $U_{\text{pulse}} = -0.5\ V$ (b) $U_{\text{pulse}} = -1\ V$

(c) $U_{\text{pulse}} = -2\ V$ (d) $U_{\text{pulse}} = -3\ V$

Figure 5.14: Prediction of the axon models activation for several pulse amplitudes. Increasing the pulse amplitude leads to more action potential generation.

The obtained values for the VTA computed for bipolar stimulation are in Table 5.2. The same effects are observed than for monopolar stimulation. An increase of the pulse amplitude generates more activation and therefore a bigger VTA.

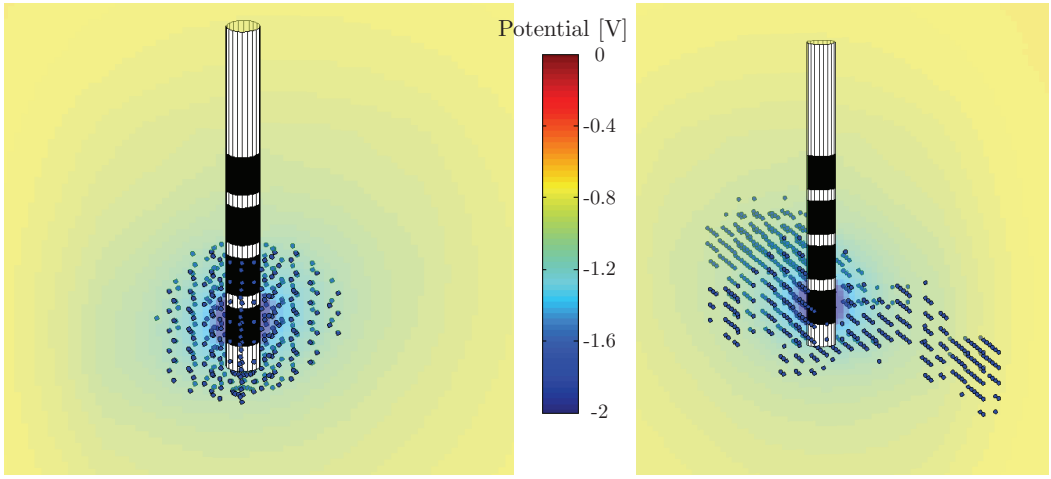

(a) (b)

Figure 5.15: Volumes of tissue activated obtained for $U_{\text{pulse}} = -2\ V$. a) axon directions tangential to the electrode shaft. b) axon directions based on DT-MRI.

Table 5.2: Influence of the pulse amplitude on the VTA [mm^3] for bipolar stimulation

$\pm U_{\text{pulse}}$ [V]	VTA with tangential direction of axons [mm^3]	r_{eq} [mm]	VTA with direction of axons based on DT-MRI [mm^3]
0.5	56	1.88	50
1	154	2.64	93
2	443	3.75	190

5.3.3 Influence of the return current electrode model

To evaluate the influence of the RCE model, the potential fields obtained with the four different models introduced in Section 4.3.3 are used. The influence of the boundary conditions applied to the model on the volume of tissue activated for a -2 V monopolar stimulation is shown in Table 5.3. The volumes of tissues activated increases when increasing the surface set to the reference potential (BC II). It also increases when modelling the RCE closer to the stimulation electrode (BC III). The VTA also increases when setting the RCE on the boundary of a reduced model as proposed in previous studies (BC IV). The equivalent radius r_{eq} increases of more than 30% when using BC IV rather than BC I. These results are coherent with the observations of Section 4.3.3, since a smaller half pulse amplitude volume (HPAV) leads to a more important decrease of potential and therefore to an increase of the VTA.
The influence in bipolar stimulation has not been computed since for that configuration, the potential distribution is not influenced by the choice of the RCE model (see the results of Section 4.3.3).

Table 5.3: Influence of the RCE model on the VTA [mm^3]

RCE type	VTA with tangential direction of axons [mm^3]	r_{eq} [mm]	VTA with direction of axons based on DT-MRI [mm^3]
BC I	165	3.40	208
BC II	178	3.49	232
BC III	235	3.83	320
BC IV	358	4.45	483

Table 5.4: Influence of the tissue conductivity on the VTA [mm^3]

Refined tissue conductivity type	VTA with tangential direction of axons [mm^3]	r_{eq} [mm]	VTA with direction of axons based on DT-MRI [mm^3]
base	165	3.40	208
lower	204	3.65	234
upper	138	3.20	184

5.3.4 Influence of the tissue conductivity

The influence of the tissue conductivity on the volume of tissue activated is investigated for the class of tissue showing the most important changes in the potential, namely the refined tissues. As shown in Section 4.3.2, the potential distribution is affected by the conductivity of tissues in monopolar configuration whereas in bipolar configuration it remains practically unaffected. Therefore, the evaluation will be conducted for the monopolar configuration only. Table 5.4 shows the computed volumes of tissues obtained using the three different conductivity values for the refined tissues, as explained in Section 4.3.2. The pulse amplitude is set to -2 V and the BC applied are of type BC I. The volumes are computed using either a tangential direction for axons or a direction based on the DT-MRI.
The results show that the obtained VTA are affected by the used conductivity of tissue values. The biggest VTA is obtained when the lower conductivity is used. This is in accordance with the observations of Section 4.3.2, as a smaller HPAV and therefore a more important potential drop has been observed with this parameter. Nevertheless, the variations observed are less important than when modifying the other parameters under consideration (pulse amplitude or RCE model).

5.3.5 Discussion

The observed VTA are very different when evaluated with tangential or with DT-MRI based axon directions. The volume obtained with tangential axon directions seems more realistic than the one obtain with the alternative method. But independently of the approach chosen for the VTA computations, the same trends are observed on the influence of the parameters. The irregularities observed when using DT-MRI based axon direction arise because of the the variations of axon directions from voxel to voxel and because when a voxel does not show any anisotropy, no axon models are used. Nevertheless the information they provide should help the neurologist to identify if some specific area are activated or not by the stimulation.

All of the parameters previously tested impacted the VTA. Nevertheless, the impact of the choice of RCE model is more important than the choice of tissue conductivity. The differences observed when using the realistic BC proposed in this thesis rather than a simplified BC as in previous studies (BC IV) [8,9,16,18–20,22,26,27,30,31] on the VTA is very important (-54% for tangential axon models and -57% for DT-MRI based axon models). For the equivalent radius, the observed reduction is of -24%.

5.4 Conclusion

This chapter has introduced the neural aspects into the model. Based on the potentials obtained for the FE model, the response to stimulation of specific axon models has been evaluated. In particular the electrical equivalent model for an axon has been reviewed and the role of currents and potentials in axon activation has been discussed. The equations show the relevance of the second spatial derivative of the potential (the so called activation function f) in the firing of the axonal signal.
The link between the computed potential obtained from the finite element model and their derivatives and the volume of tissue activated is explored through the computed based NEURON environment tool. For the VTA computation, two original techniques have been used. The first uses axon models having their direction set tangentially to the electrode shaft. The second uses the information provided by DT-MRI to set the direction of axon models anatomically.
The VTA obtained with the first technique showed good agreement with previous studies. As for the second technique, which includes anatomical anisotropy, it produces very interesting results as it should be possible to make correlations with real anatomical structures in the brain. Most probably, the most reliable results can be obtained with a combination of both techniques.
It has been shown that the volume of tissue activated by the stimulation increases with the pulse amplitude, which agrees with clinical observations. Special care should be taken to set the conductivity of tissues, as this parameter also impacts the volumes of tissue activated. Finally, it has been shown that using the original more realistic BC introduced in this thesis rather than the simplified ones generally used in literature leads to an important decrease of the VTA. This would tend to prove that there is an important overestimation of VTA values in the current literature.

Bibliography

[1] J. Malmivuo and R. Plonsey, *Bioelectromagnetism*. Oxford University Press, 1995.

[2] A. L. Hodgkin and A. F. Huxley, "A quantitative description of membrane current and its application to conduction and excitation in nerve." *J Physiol*, vol. 117, no. 4, pp. 500–544, Aug 1952.

[3] B. Frankenhaeuser and A. F. Huxley, "The action potential in the myelinated nerve fiber of xenopus laevis as computed on the basis of voltage clamp data," *J Physiol*, vol. 171, pp. 302–315, Jun 1964.

[4] F. Rattay, *Electrical Nerve Stimulation*. Springer-Verlag, 1990.

[5] D. R. McNeal, "Analysis of a model for excitation of myelinated nerve." *IEEE Trans Biomed Eng*, vol. 23, no. 4, pp. 329–337, Jul 1976.

[6] F. Rattay, "Analysis of models for external stimulation of axons," *IEEE Trans Biomed Eng*, 1986.

[7] A. M. Kuncel and W. M. Grill, "Selection of stimulus parameters for deep brain stimulation." *Clin Neurophysiol*, vol. 115, no. 11, pp. 2431–2441, Nov 2004. [Online]. Available: http://dx.doi.org/10.1016/j.clinph.2004.05.031

[8] C. C. McIntyre, S. Mori, D. L. Sherman, N. V. Thakor, and J. L. Vitek, "Electric field and stimulating influence generated by deep brain stimulation of the subthalamic nucleus." *Clin Neurophysiol*, vol. 115, no. 3, pp. 589–595, Mar 2004. [Online]. Available: http://dx.doi.org/10.1016/j.clinph.2003.10.033

[9] X. F. Wei and W. M. Grill, "Current density distributions, field distributions and impedance analysis of segmented deep brain stimulation electrodes." *J Neural Eng*, vol. 2, no. 4, pp. 139–147, Dec 2005. [Online]. Available: http://dx.doi.org/10.1088/1741-2560/2/4/010

[10] R. Plonsey and R. C. Barr, "Electric field stimulation of excitable tissue." *IEEE Trans Biomed Eng*, vol. 42, no. 4, pp. 329–336, Apr 1995.

[11] E. N. Warman, W. M. Grill, and D. Durand, "Modeling the effects of electric fields on nerve fibers: determination of excitation thresholds." *IEEE Trans Biomed Eng*, vol. 39, no. 12, pp. 1244–1254, Dec 1992.

[12] L. G. Nowak and J. Bullier, "Axons, but not cell bodies, are activated by electrical stimulation in cortical gray matter. i. evidence from chronaxie measurements." *Exp Brain Res*, vol. 118, no. 4, pp. 477–488, Feb 1998.

[13] ——, "Axons, but not cell bodies, are activated by electrical stimulation in cortical gray matter. ii. evidence from selective inactivation of cell bodies and axon initial segments." *Exp Brain Res*, vol. 118, no. 4, pp. 489–500, Feb 1998.

[14] F. Rattay, "The basic mechanism for the electrical stimulation of the nervous system." *Neuroscience*, vol. 89, no. 2, pp. 335–346, Mar 1999.

[15] C. C. McIntyre, A. G. Richardson, and W. M. Grill, "Modeling the excitability of mammalian nerve fibers: influence of afterpotentials on the recovery cycle." *J Neurophysiol*, vol. 87, no. 2, pp. 995–1006, Feb 2002. [Online]. Available: http://jn.physiology.org/cgi/reprint/87/2/995

[16] C. R. Butson, S. E. Cooper, J. M. Henderson, and C. C. McIntyre, "Patient-specific analysis of the volume of tissue activated during deep brain stimulation." *Neuroimage*, vol. 34, no. 2, pp. 661–670, Jan 2007. [Online]. Available: http://dx.doi.org/10.1016/j.neuroimage.2006.09.034

[17] ——, "Predicting the effects of deep brain stimulation with diffusion tensor based electric field models." *Med Image Comput Comput Assist Interv Int Conf Med Image Comput Comput Assist Interv*, vol. 9, no. Pt 2, pp. 429–437, 2006.

[18] C. R. Butson, C. B. Maks, and C. C. McIntyre, "Sources and effects of electrode impedance during deep brain stimulation." *Clin Neurophysiol*, vol. 117, no. 2, pp. 447–454, Feb 2006. [Online]. Available: http://dx.doi.org/10.1016/j.clinph.2005.10.007

[19] C. R. Butson and C. C. McIntyre, "Role of electrode design on the volume of tissue activated during deep brain stimulation." *J Neural Eng*, vol. 3, no. 1, pp. 1–8, Mar 2006, electrode design. [Online]. Available: http://dx.doi.org/10.1088/1741-2560/3/1/001

[20] ——, "Tissue and electrode capacitance reduce neural activation volumes during deep brain stimulation." *Clin Neurophysiol*, vol. 116, no. 10, pp. 2490–2500, Oct 2005. [Online]. Available: http://dx.doi.org/10.1016/j.clinph.2005.06.023

[21] C. C. McIntyre, W. M. Grill, D. L. Sherman, and N. V. Thakor, "Cellular effects of deep brain stimulation: model-based analysis of activation and inhibition." *J Neurophysiol*, vol. 91, no. 4, pp. 1457–1469, Apr 2004. [Online]. Available: http://dx.doi.org/10.1152/jn.00989.2003

[22] C. C. McIntyre, S. Miocinovic, and C. R. Butson, "Computational analysis of deep brain stimulation." *Expert Rev Med Devices*, vol. 4, no. 5, pp. 615–622, Sep 2007. [Online]. Available: http://dx.doi.org/10.1586/17434440.4.5.615

[23] C. C. McIntyre, M. Savasta, L. K.-L. Goff, and J. L. Vitek, "Uncovering the mechanism(s) of action of deep brain stimulation: activation, inhibition, or both." *Clin Neurophysiol*, vol. 115, no. 6, pp. 1239–1248, Jun 2004. [Online]. Available: http://dx.doi.org/10.1016/j.clinph.2003.12.024

[24] C. C. McIntyre, M. Savasta, B. L. Walter, and J. L. Vitek, "How does deep brain stimulation work? present understanding and future questions." *J Clin Neurophysiol*, vol. 21, no. 1, pp. 40–50, 2004.

[25] S. Miocinovic, M. Parent, C. R. Butson, P. J. Hahn, G. S. Russo, J. L. Vitek, and C. C. McIntyre, "Computational analysis of subthalamic nucleus and lenticular fasciculus activation during therapeutic deep brain stimulation." *J Neurophysiol*, vol. 96, no. 3, pp. 1569–1580, Sep 2006. [Online]. Available: http://dx.doi.org/10.1152/jn.00305.2006

[26] S. Sotiropoulos and P. Steinmetz, "Assessing the direct effects of deep brain stimulation using embedded axon models," *Journal of Neural Engineering*, vol. 4, no. 2, pp. 107–119, 2007. [Online]. Available: http://stacks.iop.org/1741-2552/4/107

[27] C. R. Butson and C. C. McIntyre, "Current steering to control the volume of tissue activated during deep brain stimulation," *Brain Stimulation*, vol. 1, no. 1, pp. 7–15, 2008. [Online]. Available: www.scopus.com

[28] M. L. Hines and N. T. Carnevale, "The neuron simulation environment." *Neural Comput*, vol. 9, no. 6, pp. 1179–1209, Aug 1997.

[29] J. B. Ranck, "Which elements are excited in electrical stimulation of mammalian central nervous system: a review." *Brain Res*, vol. 98, no. 3, pp. 417–440, Nov 1975.

[30] C. R. Butson and C. C. McIntyre, "Differences among implanted pulse generator waveforms cause variations in the neural response to deep brain stimulation." *Clin Neurophysiol*, vol. 118, no. 8, pp. 1889–1894, Aug 2007, electrode Parameters. [Online]. Available: http://dx.doi.org/10.1016/j.clinph.2007.05.061

[31] N. Yousif, R. Bayford, P. G. Bain, and X. Liu, "The peri-electrode space is a significant element of the electrode-brain interface in deep brain stimulation: A computational study." *Brain Res Bull*, vol. 74, no. 5, pp. 361–368, Oct 2007. [Online]. Available: http://dx.doi.org/10.1016/j.brainresbull.2007.07.007

6 Conclusions and Future Work

6.1 Thesis assessment

Deep brain stimulation is a invasive surgical technique widely used in the last twenty years to treat Parkinson's disease and similar movement disorders. But despite his relatively long existence, the understanding of its action mechanisms remains unclear and controversial.
This thesis aims to provide a clear understanding of the electromagnetic aspects of the stimulation, and a precise evaluation of the involved electric potentials. Through this, a better prediction of clinically important parameters like the volume of tissue likely to be activated by the stimulation is hoped to be achieved.
Since this thesis is intended not only for electrical engineers but also for medical doctors and practicians, an effort has been made to provide the needed background in both areas. Thus, a definition of the bioelectromagnetism and of some of its applications is provided to the reader in Chapter 2. Special care is taken to explain the applications of electromagnetic stimulations, and more specifically of the electrical deep brain stimulation. Therefore, a review of the history of that technique and of the State of the Art was undertakn as a preliminary task.

Preliminary facts

One of the catalysts for the strategy adopted in this thesis was the consideration of two antagonist facts. On one side, it was evident that the new imaging techniques were providing a description of the human body's inner anatomy and physiology with an accuracy and detail never previously achieved. Also for the first time, results concerning the natural anisotropy of biological tissues were available, for instance thanks to the diffusion tensors generated by magnetic resonance imaging (MRI).
On the other hand the translation of these informations into electric properties of living biological tissues remains uncertain. For instance, it is not unusual to find in the literature estimations for the isotropic conductivity of tissues varying by a factor of five or even ten. And the anisotropy of the electrical conductivity was scarcely taken into account, although it is obviously a very important property. Any sound electrical model accurately depicting a very inhomogeneous medium (the brain) where directive structures (the neurons) are embedded should show a strong anisotropy!

Better description of conductivity and anisotropy

The above considerations prompted us to try to develop a new model for DBS, where these properties and uncertainties would be better taken into account. Although the natural biological variability will prevent us forever to assign to the tissue conductivities numerical bounds as narrow as those used for inorganic media, there was clearly a lot of room for improvement.
This led to some of the first relevant achievements in the thesis: the thorough study of the effect of conductivity variation and the systematic introduction of a conductivity tensor, obtained through an original treatment of the MRI diffusion tensors. With this approach, conductivity values could even

be individually adapted to each patient!

New theoritical model, better boundary conditions

The obvious consequence was the need to start with a re-appraisal of the equations customarily solved in biolelectromagnetism. Here, they are derived from the fundamental differential equations of electromagnetism (Maxwell), including anisotropy from the very beginning. The developed formulation leaves the door open for further rigorous developments, like the quantification of associated magnetic fields and the use of electric permittivity and magnetic permeability properties.
A key ingredient for the accurate solution of differential equations is the use of a correct geometrical discretization and of the proper boundary conditions (BC). Most existing models use conservative or oversimplified boundary conditions (Dirichlet). In this work we us, for the first time, more appropriate BCs (Neumann) that correctly reproduce the behavior of potentials and currents in the limiting surfaces of the problem (skin in contact with the air and IPG).

Computer implementation, better geometry, refined finite elements

No claims of originality are made respect to the choice of the numerical discretization technique. Finite elements (FE) are here the obvious choice, as recognized by most researchers in the area.
However, this thesis provides a original computer implementation, using equations that naturally accepts anisotropy. Also, an intermediate complexity model has been introduced for the geometry under study. It includes head, neck and upper chest and, in this sense, it goes a step beyond the currently used reduced head models. On the other hand, the proposed model remains reasonably simple in terms of tissue characterization (eight different types) and anatomy reconstruction (parallelepipeds and cylinders) and it is readily tractable with a single advanced desktop computer. Accuracy is improved by using an adaptive mesh that refines the tissue description in a critical small region around the electrode.

A wealth of numerical results

All the above improvements concur to produce a numerical model that is supposed to predict realistic and accurate values for the electric potentials and other mathematically derived quantities.
One of the immediate benefits is the possibility of running systematic sensitivity or parametric studies. This document summarizes a few of the most significant results. Many other were obtained, by running exhaustively a computer model with almost half a million of unknowns and changing the conductivity values, the mesh density, the boundary conditions, the type of electric stimulation (monopolar, multipolar...) and many other relevant parameters. For instance it can be clearly shown with the proposed model that tissue conductivity is strongly influencing the potential distribution generated by DBS, especially in monopolar configurations.

Our model provides also many other interesting results. The IPG (implanted pulse generator, usually under the collarbone) plays a major role from an electrical point of view, especially in monopolar stimulation. Indeed, in this configuration the involved electric loop is closed through the conductive face of the IPG. Our model can easily characterize this situation, since it extends to the upper chest and it uses the right boundary conditions allowing the correct characterization of a return current.

The obtained results show that the approaches usually chosen in the literature to model DBS are systematically underestimating several key indicators used to quantify the electrical potential distribution, like the tissue impedance and the half pulse amplitude volume.

Combining finite elements and neuron/axon models

Whereas the information provided by our model is considered to be reliable from an electric point of view, it is hard to evaluate the impact it can have on the actual neural processes. A first step in this direction is provided in this thesis by applying the obtained potential distribution to a well established electric neuron/axon model. For the sake of completeness the basics of neural signal propagation are first reviewed and the electrical equivalent models for axons are introduced. Then the specific axon models used to predict the volumes of tissue activates are discussed.

More flexibility in axons' orientation

Thanks to the inclusion of anisotropy and to the enhanced anatomical information available, we have been able to include two improved axon models, defined not only by their topologies but also by their orientation respect to the electrode.
The first type exhibits a radial orientation, normal to the electrode shaft. For the second type, the axon orientation is set according to the information provided by the diffusion tensor and therefore it bears information about the actual anatomical position of fibres surrounding the electrode.
The results obtained for the first type of axons show good agreement with previous studies. As for the second technique, it produces very promising new results, as they should make possible to perform correlations with real anatomical structures.

The volume of tissue activated by DBS

The combination of the global finite element model with local axon models allows a first prediction of the volume of tissue activated (VTA) . First, it has been checked that, as expected and in agreement with clinical observations, VTA increases with the pulse amplitude. More interesting is to obtain the impact of the tissues conductivity and of the BCs. Thanks to the correct approach used to model the return current in monopolar configurations, we can show that the simplified assumptions and the BCs currently used in the literature may lead to a serious (typically more than 30%) overestimation of the equivalent radius of volume of tissues activated. As expected, results are practically unaffected by the choice of BC or the modification of parameters in distal tissues in the case of bipolar configurations.

6.2 General discussion on the model

The model used in this thesis has been developed based on a survey of the existing models found in literature. It includes most of the important aspects proposed in these studies. Nevertheless several assumptions have been made are discussed globally in this section.

On a geometrical point of view, the main objective was to include the whole electric loop involved in the monopolar deep brain stimulation. Therefore, the models is not based on a reduced size model of the head but encompass the head, neck and upper chest of a human. The simplified geometry used for these structures is motivated by a reduction of the number of unknowns and the easier generation of the model, while keeping its essential features. The number of tissues classes used in the model is based on anatomical consideration and on the values of electric conductivity available in literature. These geometrical considerations can be debated as they only partially represent reality. Improvements of the model could be obtained by using more realistic geometries for the tissues. The

most realistic model should be obtained using the information on the tissues provided by the medical imaging (MRI or DT-MRI) to build a model extending to the chest. Nevertheless, this technique would need and important pre-processing task. Indeed, the use of MRI would need a segmentation process, while the use of the DTMRI would not provide a good characterization of some tissues such as the bones. Moreover, the use of elements having the same definition than voxels provided by the medical imaging would dramatically increase the number of unknowns in a model encompassing the whole electric loop.
An interesting way to avoid the problem of the return current electrode model would be to use of a model using fixed currents rather than fixed voltage as boundary conditions. In that case, a reduced size model could be used, providing that the total current going out of the stimulation electrode equals the current going out of the external boundary of the problem. Nevertheless, the obtained potentials will be highly dependent of the value of the conductivity.
An important aspect that is not treated in this work is the cicatricial tissues that will systematically form around the stimulation electrode after the surgery. These tissues are obviously of course not present on medical imaging obtained before surgery, but are surely influencing the potential distribution. The model proposed here could be really improved by inserting an encapsulation of cicatricial tissues around the electrode contact.

The use of the quasistatic approximation in this work can also be discussed as the biological tissues are showing capacitive effects. Therefore, the time variation of the potential will be affected by these capacitive properties of the tissues, deforming the electric pulse shape. These deformations might generate variation on the firing of the axons models.
Another timely aspect that has not been treated in this work is the influence of the pulse width. Increasing this parameter should lead to an increase of the firing of axons. Indeed, the threshold for an action potential generation should be easier to reach with longer stimulation times.
Another key parameter of the DBS is the frequency of stimulation. This parameter has an influence on the global neural response to stimulus rather than on the firing of axons, since the usual refractory period is about one millisecond and the frequency of stimulation does not exceeds 200 Hz.

Finally the technique used to evaluate the volume of tissue activated (VTA) is highly dependent on the axon models. The response of a neuron to extracellular stimulation is linked to several parameters such as its geometrical properties and its direction.
The choice of using axon models rather than soma is motivated by the fact that this part of neuron is the most excitable one by extracellular stimulation. This choice is logical when modeling white matter fibers, as they are mainly composed of axons, but it can be questioned for gray matter, as it is essentially made of soma. The use of neuron models adapted to each voxel could be implemented in further research.
The choice of the direction is also determinant for the evaluation of the response of a neuron to external stimulation, as shown by the obtained VTA. When tangential direction for the axons are used, the VTA have an spheroidal shape that reflects the global extent of the stimulation. When the axon direction is determined with the help of the DT-MRI, the VTA shape is highly irregular. It shows important information on the ability of anatomical structures to influence on the firing threshold when they are not in the direct vicinity of the stimulation electrode. The irregular shape has to major origins: the fact that when a voxel doesn't show anisotropy, no evaluation of the activation is performed, and the high discontinuity in the axon direction when moving from a voxel to another one. To improve the VTA obtained, the use of both approaches should be mixed. Axons located in voxels showing high anisotropy should have their directions fixed by this anisotropy, while in voxels showing low anisotropy, models of soma having no preferential direction or a statistical distribution

should be used.

6.3 Perspectives and future work

The immediate objective of the thesis, namely to provide a tool able to accurately predict the electric potentials generated in DBA has been clearly achieved. The subsequent and more exciting goal is to predict the volume of tissue activated by the deep brain stimulation. This goal can be also considered as fulfilled. Our model has demonstrated both to give results in accordance with the literature and to correct the literature predictions in more complex situations.

To go further, the model should also foresee the influence of different positions of the electrode in the brain. This would help to predict the optimized localization of the electrode from an initial position targeted before surgery. Moreover, for post-operative studies, very accurate results could be obtained with the definitve electrode localization, providing information on the activated area involved in long term effects of DBS.

The model developed here does not include the so-called "brain-electrode" interface, which has been shown to impact the potential distribution. Recent observations have demonstrated the creation in a thin region around the electrode contacts of a layer of tissue whose properties are affected and modified by the electrode. Moreover, very accurate results could then be obtained for the final electrode localization.

One of the main results obtained from this study is the accurate modelling of the return current electrode in monopolar voltage stimulation, ignored in most existing studies. This return current plays an important role not only on the potential distribution but also on the predicted volume of tissue activated. A promising technique to make the stimulation less dependent on return currents is the recently announced introduction of current controlled electrodes. Our model is general and should be easily adapted to this new electric excitation (fixed current rather than voltage). Also the boundary conditions should be re-examined in the case of fixed current excitation as by continuity the total current issued from the electrode contact should be equal to the current going out of any closed surface surrounded the electrode, thus opening new possibilities for reduced geometrical models. The tissue conductivity would remain a key factor in this type of situations and this is also a positive asset for our model.

From a medical point of view, the obtained volumes of tissue activated should be correlated with anatomical atlases, to identify the anatomical zone activated by the stimulation especially in long term effects studies. Another interesting challenge with obvious clinical implications is to evaluate the influence of the position of the return electrode (IPG) on a patient.

List of Figures

List of Tables

CV

Grégoire Walckiers was born on August 18, 1980 in Meyrin, Swiss. He received the Ing. Él. Dipl. EPF (Ingénieur électricien diplômé EPF) degree from the Ecole Polytechnique Fédérale de Lausanne (EPFL), in April 2004. In September 2004 he enrolled the PhD studies at the Laboratoire d'Electromagnétisme et d'Acoustique (LEMA) of the Ecole Polytechique Fédérale de Lausanne (EPFL), where he is currently a Research and Teaching Assistant. As a Research Assistant he has been responsible for several projects.

- Development of computer model for the Deep Brain Stimulation in collaboration with the Centre Hospitalier Universitaire Vaudois. (2004-present)
- Design and simulation of RF Rotary Joint for Mobile In-Vehicle Entertainment in the framework of the European Space Agency project "Hi-SAT" (ESA/ESTEC Contract No. 20185/06/NL/NH). European Space Agency Project (2006-present).

As a Teaching Assistant he has led the exercises in classes on Electromagnetics I and II, graded exams, and proposed and supervised student semester projects.

List of Publications

REFEREED JOURNAL PAPERS

1. G. Walckiers, B. Fuchs, J.-P. Thiran, J. R. Mosig and C. Pollo, "Influence of the Return Current Electrode Model in Finite Element Model of Monopolar Deep Brain Stimulation," *IEEE Transactions on Biomedical Engineering*, under review.

REFEREED CONFERENCE PAPERS

1. G. Walckiers, J.-P. Thiran, J. R. Mosig and C. Pollo, "Influence of Boundary Condition in Monopolar Deep Brain Stimulation Models," *6th Forum of European Neuroscience (FENS '08)*, Genève, Suisse, Jul. 12–16, 2008, Abstr., vol.4, 218.62.
2. G. Walckiers, J.-P. Thiran, J. R. Mosig and C. Pollo, "Iterative Full Head Finite Element Model for Deep Brain Stimulation," *3rd International IEEE/EMBS Conference on Neural Engineering (CNE '07)*, Hawaii, USA, May 2–5, 2007, pp. 561–563.
3. G. Walckiers, J. R. Mosig and C. Pollo, "A New Approach to Model Boundary Conditions in Finite Element Method Analysis of Deep Brain Stimulation," *First European Conference on Antennas and Propagation (EuCAP 2006)*, Nice, France, Nov. 6–10, 2006.
4. C. Pollo and G. Walckiers, "3D Computer Model of Brain Electrical Propagation from a Localizable Source," *Meeting of the European Society of Stereotactic and Functional Neurosurgery (ESSFN 2006)*, Montreux, Suisse, Oct. 4–7, 2006.
5. C. Pollo and G. Walckiers, "Influence of Boundary Conditions on Finite Element Models of Deep Brain Stimulation," *Meeting of the American Society of Stereotactic and Functional Neurosurgery (ASSFN 2006)*, Boston, USA, Jun. 1–4, 2006.